ADVANCED STEEL CONSTRUCTION

An International Journal

Volume 5 Number 1

March 2009

CONTENTS

Technical Papers

The Hong Kong Institute of Steel Construction
Website: *http://www.hkisc.org*
ISSN 1816-112X
Science Citation Index Expanded, Materials Science Citation Index and ISI Alerting

Cover: Skylight at MGM, Macau, China
designed by second-order P-Δ-δ analysis without assumption of effective length

---

ADVANCED STEEL CONSTRUCTION

VOL.5, NO.1 (2009)

ADVANCED STEEL CONSTRUCTION

an International Journal

ISSN 1816-112X

Volume 5 Number 1 *March 2009*

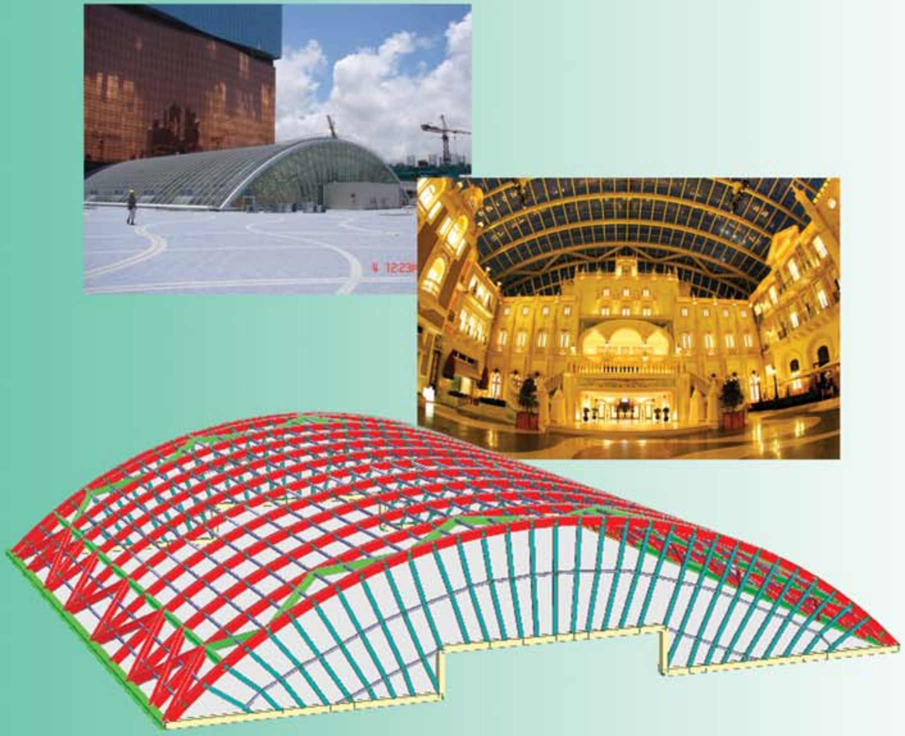

Advanced Steel Construction
an international journal

ISSN 1816-112X

Science Citation Index Expanded, Materials Science Citation Index and ISI Alerting

EDITORS-IN-CHIEF

Asian Pacific, African and organizing Editor
S.L. Chan
The Hong Kong Polyt. Univ., Hong Kong

American Editor
W.F. Chen
Univ. of Hawaii at Manoa, USA

European Editor
R. Zandonini
Trento Univ., Italy

INTERNATIONAL EDITORIAL BOARD

F.G. Albermani
The Univ. of Queensland, Australia

F.S.K. Bijlaard
Delft Univ. of Technology, The Netherlands

R. Bjorhovde
The Bjorhovde Group, USA

M.A. Bradford
The Univ. of New South Wales, Australia

D. Camotim
Technical Univ. of Lisbon, Portugal

C.M. Chan
Hong Kong Univ. of Science & Technology, Hong Kong

S.P. Chiew
Nanyang Technological Univ., Singapore

W.K. Chow
The Hong Kong Polyt. Univ., Hong Kong

K.F. Chung
The Hong Kong Polyt. Univ., Hong Kong

G.G. Deierlein
Stanford Univ., California, USA

L. Dezi
Univ. of Ancona, Italy

D. Dubina
The Politehnica Univ. of Timosoara, Romania

R. Greiner
Technical Univ. of Graz, Austria

G.W.M. Ho
Ove Arup & Partners Hong Kong Ltd., Hong Kong

B.A. Izzuddin
Imperial College of Science, Technology and Medicine, UK

J.P. Jaspart
Univ. of Liege, Belgium

S. A. Jayachandran
SERC, CSIR, Chennai, India

S. Kitipornchai
City Univ. of Hong Kong, Hong Kong

D. Lam
Univ. of Leeds, UK

G.Q. Li
Tongji Univ., China

J.Y.R. Liew
National Univ. of Singapore, Singapore

X. Liu
Tsinghua Univ., China

E.M. Lui
Syracuse Univ., USA

Y.L. Mo
Univ. of Houston, USA

J.P. Muzeau
CUST, Clermont Ferrand, France

D.A. Nethercot
Imperial College of Science, Technology and Medicine, UK

D.J. Oehlers
The Univ. of Adelaide, Australia

K. Rasmussen
The Univ. of Sydney, Australia

T.M. Roberts
Cardiff Univ., UK

J.M. Rotter
The Univ. of Edinburgh, UK

C. Scawthorn
Scawthorn Porter Associates, USA

P. Schaumann
Univ. of Hannover, Germany

G.P. Shu
Southeast Univ. China

J.G. Teng
The Hong Kong Polyt. Univ., Hong Kong

G.S. Tong
Zhejiang Univ., China

K.C. Tsai
National Taiwan Univ., Taiwan

C.M. Uang
Univ. of California, USA

B. Uy
University of Western Sydney

M. Veljkovic
Univ. of Lulea, Sweden

F. Wald
Czech Technical Univ. in Prague, Czech

Y.C. Wang
The Univ. of Manchester, UK

D. White
Georgia Institute of Technology, USA

E. Yamaguchi
Kyushu Institute of Technology, Japan

Y.B. Yang
National Taiwan Univ., Taiwan

B. Young
The Univ. of Hong Kong, Hong Kong

X.L. Zhao
Monash Univ., Australia

Cover: Skylight at MGM, Macau, China
designed by second-order P-Δ-δ analysis without assumption of effective length

General Information
Advanced Steel Construction, an international journal

Aims and scope

The International Journal of Advanced Steel Construction provides a platform for the publication and rapid dissemination of original and up-to-date research and technological developments in steel construction, design and analysis. Scope of research papers published in this journal includes but is not limited to theoretical and experimental research on elements, assemblages, systems, material, design philosophy and codification, standards, fabrication, projects of innovative nature and computer techniques. The journal is specifically tailored to channel the exchange of technological know-how between researchers and practitioners. Contributions from all aspects related to the recent developments of advanced steel construction are welcome.

Instructions to authors

Submission of the manuscript. Authors may submit double-spaced manuscripts preferably in MS Word by emailing to one of the chief editors as follows for arrangement of review. Alternatively papers can be submitted on a diskette to one of the chief editors.

Asian Pacific , African and organizing editor :	Professor S.L. Chan, Email: ceslchan@polyu.edu.hk
American editor :	Professor W.F. Chen, Email: waifah@hawaii.edu
European editor :	Professor R. Zandonini, Email: riccardo_zandonini@ing.unitn.it

All manuscripts submitted to the journal are recommended to accompany with a list of four potential reviewers suggested by the author(s). This list should include the complete name, address, telephone and fax numbers, email address, and at least five keywords that identify the expertise of each reviewer. This scheme will improve the process of review.

Style of manuscript

General. Author(s) should provide full postal and email addresses and fax number for correspondence. The manuscript including abstract, keywords, references, figures and tables should be in English with pages numbered and typed with double line spacing on single side of A4 or letter-sized paper. The front page of the article should contain:

a) a short title (reflecting the content of the paper);
b) all the name(s) and postal and email addresses of author(s) specifying the author to whom correspondence and proofs should be sent;
c) an abstract of 100-200 words; and
d) 5 to 8 keywords.

The paper must contain an introduction and a conclusion. The length of paper should not exceed 25 journal pages (approximately 15,000 words equivalents).

Tables and figures. Tables and figures including photographs should be typed, numbered consecutively in Arabic numerals and with short titles. They should be referred in the text as Figure 1, Table 2, etc. Originally drawn figures and photographs should be provided in a form suitable for photographic reproduction and reduction in the journal.

Mathematical expressions and units. The Systeme Internationale (SI) should be followed whenever possible. The numbers identifying the displayed mathematical expression should be referred to in the text as Eq. (1), Eq. (2).

References. References to published literature should be referred in the text, in the order of citation with Arabic numerals, by the last name(s) of the author(s) (e.g. Zandonini and Zanon [3]) or if more than three authors (e.g. Zandonini et al. [4]). References should be in English with occasional allowance of 1-2 exceptional references in local languages and reflect the current state-of-technology. Journal titles should be abbreviated in the style of the Word List of Scientific Periodicals. References should be cited in the following style [1, 2, 3].

Journal: [1] Chen, W.F. and Kishi, N., "Semi-rigid Steel Beam-to-column Connections, Data Base and Modelling", Journal of Structural Engineering, ASCE, 1989, Vol. 115, No. 1, pp. 105-119.
Book: [2] Chan, S.L. and Chui, P.P.T., "Non-linear Static and Cyclic Analysis of Semi-rigid Steel Frames", Elsevier Science, 2000.
Proceedings: [3] Zandonini, R. and Zanon, P., "Experimental Analysis of Steel Beams with Semi-rigid Joints", Proceedings of International Conference on Advances in Steel Structures, Hong Kong, 1996, Vol. 1, pp. 356-364.

Proofs. Proof will be sent to the corresponding author to correct any typesetting errors. Alternations to the original manuscript at this stage will not be accepted. Proofs should be returned within 48 hours of receipt by Express Mail, Fax or Email.

Copyright. Submission of an article to "Advanced Steel Construction" implies that it presents the original and unpublished work, and not under consideration for publication nor published elsewhere. On acceptance of a manuscript submitted, the copyright thereof is transferred to the publisher by the Transfer of Copyright Agreement and upon the acceptance of publication for the papers, the corresponding author must sign the form for Transfer of Copyright.

Permission. Quoting from this journal is granted provided that the customary acknowledgement is given to the source.

Page charge and Reprints. There will be no page charges if the length of paper is within the limit of 25 journal pages. A total of 30 free offprints will be supplied free of charge to the corresponding author. Purchasing orders for additional offprints can be made on order forms which will be sent to the authors. These instructions can be obtained at the Hong Kong Institute of Steel Construction, Journal website: http://www.hkisc.org

The International Journal of Advanced Steel Construction is published quarterly by non-profit making learnt society, The Hong Kong Institute of Steel Construction, c/o Department of Civil & Structural Engineering, The Hong Kong Polytechnic University, Hung Hom, Kowloon, Hong Kong.

Subscription inquiries and change of address. Address all subscription inquiries and correspondence to Member Records, IJASC. Notify an address change as soon as possible. All communications should include both old and new addresses with zip codes and be accompanied by a mailing label from a recent issue. Allow six weeks for all changes to become effective.

The Hong Kong Institute of Steel Construction
HKISC
c/o Department of Civil and Structural Engineering,
The Hong Kong Polytechnic University,
Hunghom, Kowloon, Hong Kong, China.
Tel: 852- 2766 6047 Fax: 852- 2334 6389
Email: *ceslchan@polyu.edu.hk* Website: *http://www.hkisc.org/*
ISSN 1816-112X
Science Citation Index Expanded, Materials Science Citation Index and ISI Alerting

ISSN 1816-112X

Science Citation Index Expanded, Materials Science Citation Index and ISI Alerting

Advanced Steel Construction
an international journal

VOLUME 5 NUMBER 1 MARCH 2009

Technical Papers

Conference Announcements

NEW MODELING TECHNIQUE FOR BIONIC SPACE GRID STRUCTURES

N. Li and Y.Z. Luo*

Space Structures Research Center, Zhejiang University, Hangzhou, China
**(Corresponding author: E-mail: luoyz@zju.edu.cn)*

Received: 31 October 2007; Revised: 15 December 2007; Accepted: 20 December 2007

ABSTRACT: This paper is intended to introduce a new modeling technique for bionic space grid structures. Utilizing the methods derived from bionics and reverse engineering, the modeling technique acquires geometric data points of the natural patterns. Generally, the theory of bionics is used to express the forms of spatial patterns in direct analytic function of curves or surfaces. In this paper, the key point is to express obvious geometric features in data points. For more complicated natural patterns, it is convenient to get data points by three-dimensional (3D) measurement in reverse engineering. So this paper introduces the 3D measurement and explains the manipulations of the data points detailedly. Then the free-form surface of the natural pattern is reconstructed and meshed by the re-interpolation reflection meshing method, which combines the bi-cubic B-spline interpolation of surface and reflection meshing method. In order to satisfy the practical requirement, several meshing ways and evaluation functions of grid quality are proposed. There are several illustrated design examples are presented.

Keywords: Modeling technique; space grid structure; bionics; reverse engineering; B-splines interpolation; meshing

1. INTRODUCTION

Generally speaking, the forms of space grid structures are usually expressed in regular shape. Take the space truss or latticed shell for example. Its form is easily designed in a plane, a semi-cylinder, a semi-sphere and so on. But nowadays, there are some special bionic space grid structures, which imitate the natural patterns vividly, appearing in public buildings. Since their elements can neatly express the free-form surface, their forms become diversified in the development. Such as the aim in the "Bubble" (Figure 1), the given name for the Exhibition-Pavillon of BMW at the International Motorshow IAA in Frankfurt in 1999, was to support the formal idea by expressing the dynamic balance of the two water drops becoming a unit and suggesting the idea that form is only a "frozen moment" (Harald [1]).

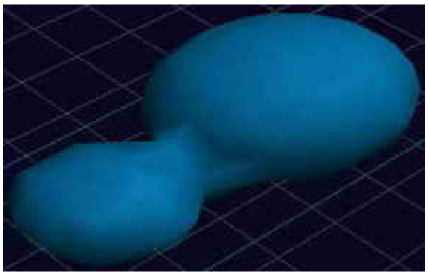

(a) Form Simulation

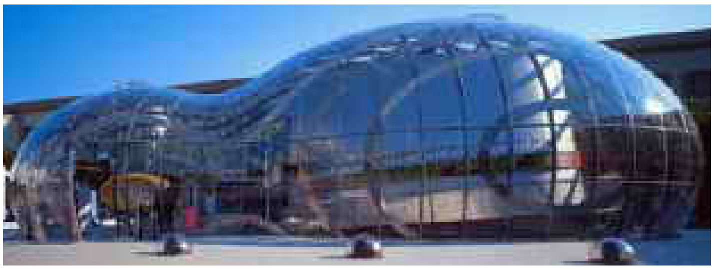

(b) Final Project

Figure 1. Bubble-Project

However, it is quite difficult to rebuild the modeling of the natural pattern, as this free-form surface can not be represented by the direct analytic function. For this reason it is easy to understand the interested designers have different techniques like bionics and mathematics theory (Stach [2]). The data points of the surface can be acquired by methods derived from bionics or reverse engineering, and then can be used to reconstruct the whole surface by techniques of mathematics. So the modeling technique applied in this paper begins with the acquisition of the data points, and its essential process is to rebuild the space grid structure from the data points.

At present, there are two methods to get the data points. The one is basic geometric feature extraction and the other is three-dimensional (3D) measurement. The basic geometric feature extraction comes from the theory of bionics. Raup [3] found that the surface of seashells could be expressed by four basic parameters. Stach [2] described three familiar seashells with those basic parameters and obtained the corresponding analytical curves. The 3D measurement is derived from the reverse engineering of geometric models. Reverse engineering typically starts with measuring an existing object so that a surface or solid model can be deduced in order to exploit the advantages of CAD/CAM technologies. The 3D measurement comprises a lot of methods, such as optical, acoustic, magnetic methods and so on (Várady et al. [4]). In all of them, the laser scanning is used most commonly, which is an optical non-contact method and uses 3D scanner to get points. Barber et al. [5] concluded that the data acquisition had greatly progressed in these last years due to the introduction of laser scanning technologies. Balz and Böhm [6] outlined the point clouds of the morphology scanned by 3D scanner. According to Harald [1], in the design process of M.art.A. Museum in Herford, a series of physical models were built manually by architects and then were three-dimensionally digitized by using 3D scanner. The resulted data were transformed in the computer-aided design environment to correct the shape and define the digital database.

After the acquisition of data points, some techniques of mathematics can be applied to rebuild the practical structures. Gong [7] first introduced the theory of computer-aided geometric design (CAGD) into the modeling technique of space grid structure. Then the reflection meshing method was applied to deal with the free-form surface, and evaluation functions of grid quality were proposed (Zhang [8]). Cen [9] advanced the re-interpolation reflection meshing method and completed the program to realize a variety of shells. There were several practical meshing ways extended to divide the surface (Li and Luo [10]). The modeling technique combines these methods, and furthermore, in order to deal with the problem of data points which are not of rectangular topology, the cubic B-spline interpolation of curve will be used.

According to the above introduction, the modeling technique in this paper comprises two important phases. The first one is data acquisition, and the second one is surface reconstruction and meshing. Especially in the first phase, the modeling technique utilizes both geometric feature extraction and 3D measurement to get data points. Generally, the theory of bionics is used to express the forms of spatial patterns in direct analytic function of curves or surfaces. In this paper, the geometric feature extraction derived from bionics expresses the obvious geometric features in data points. For more complicated natural patterns, the 3D measurement is used to get data points conveniently. So this paper introduces this method and explains the manipulations of the data points detailedly. The second phase of surface reconstruction and meshing which have been improved continuously is also described to complete the whole modeling. Several design examples will be presented to illustrate the technique.

2. DATA ACQUISITION

This section will expatiate on the two methods, basic geometric feature extraction and 3D measurement, which get the data points from the surface of natural pattern rationally.

2.1 Basic Geometric Feature Extraction

Through observing the *scallop*, *pilosa* and other spatial patterns, it is found that the geometric features can be expressed by base-lines and ridge-lines, as shown in Figure 2. The base-lines determine the basic shape of the pattern while the ridge-lines determine the curvature.

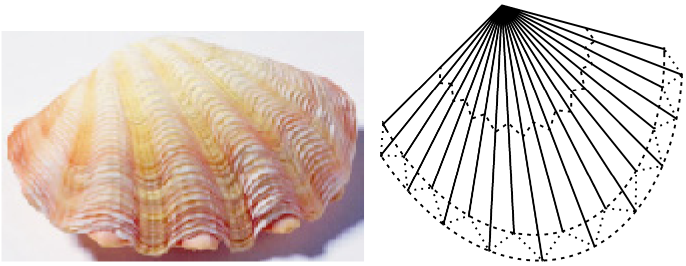

(a) *Scallop*

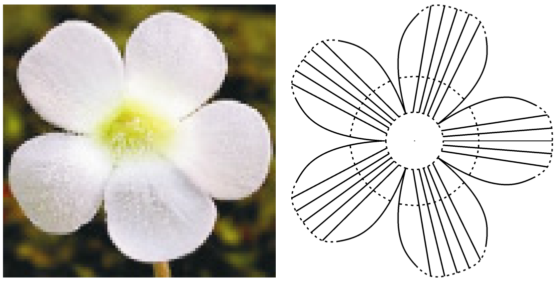

(b) *Pilosa*

Figure 2. Natural Patterns

The chain Dots Denote the Base-lines, and the Solid Lines Denote the Ridge-lines.

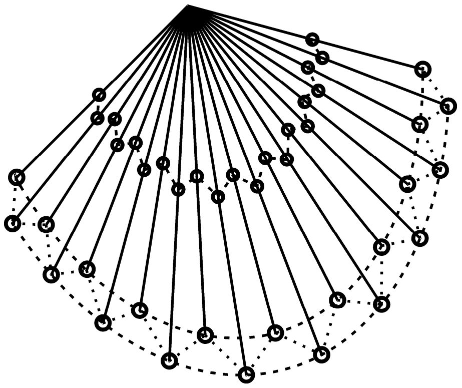

Figure 3. Data Points

The Open Circles Express the Position of Data Points.

Data points are extracted from the base-lines and ridge-lines. Figure 3 shows that the data points are of topological relationship and consist of intersection.

To get the ideal curvature, the data points, which are placed on middle of ridge-lines, can be adjusted in two ways, which are named z-coordinate offset and expansion coefficient set respectively, as shown in Figure 4. In Cartesian coordinates, z-coordinate offset modifies z coordinate of the data points to target position, and the expansion coefficient set changes the size of the adjustable ring, which consists of data points of the same z-coordinate.

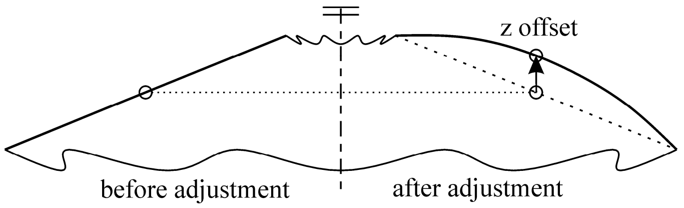

(a) Z-Coordinate Offset

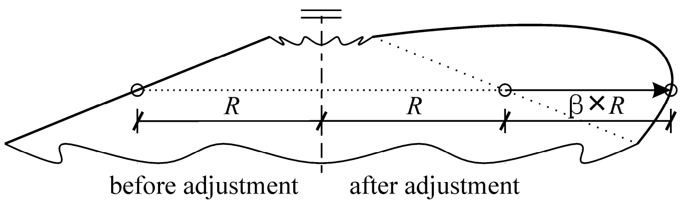

(b) Expansion Coefficient Set. β is the Expansion Coefficient.

Figure 4. The Ways of Adjustment

2.2 3D Measurement

With the rapid development of 3D measurement technology, it becomes easier to get precise data points from the natural patterns. In this paper, the important point is to explain the manipulations of the data points, so it will not refer to the instruction for the equipment of 3D measurement.

2.2.1 Point clouds

By 3D measurement, a large amount point data of physical surface can be recorded, which are 3D coordinates and stored in computer with certain files. These point data are so-called point clouds. For example, the advantages of the laser scanning are its capacity to store large 3D point clouds acquired with a high speed and a high level of precision (Luca et al. [11]). In Figure 5a and Figure 6a, the point clouds show cylindrical and conical surfaces. In Figure 7a, the point clouds come from a *dolphin* model, so its surface is free-form. All of these point clouds are scattered.

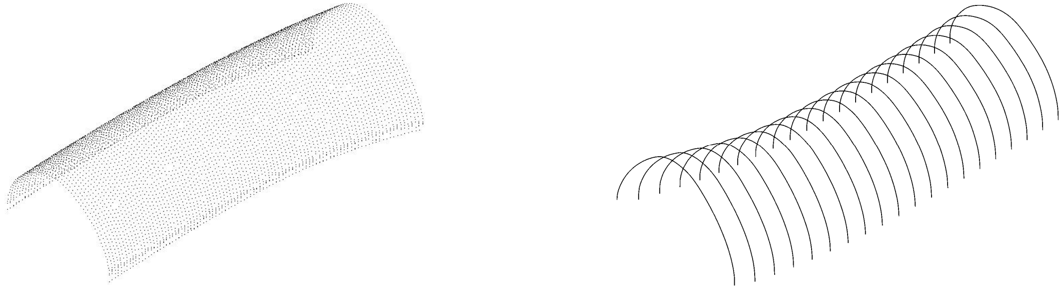

(a) Point Clouds (b) Data Points

Figure 5. Cylindrical Surface

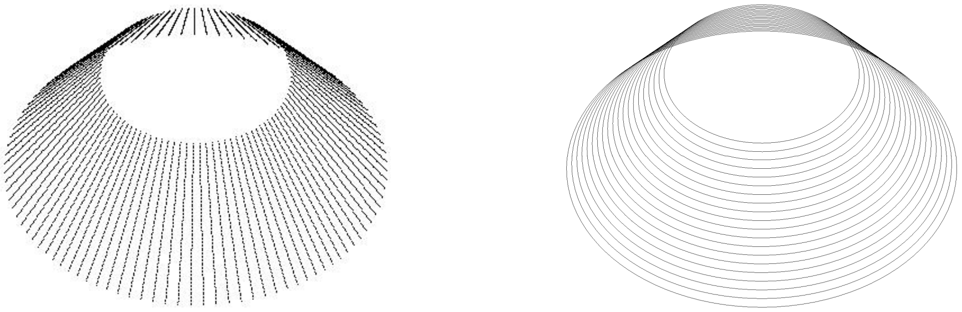
(a) Point Clouds (b) Data Points

Figure 6. Conical Surface

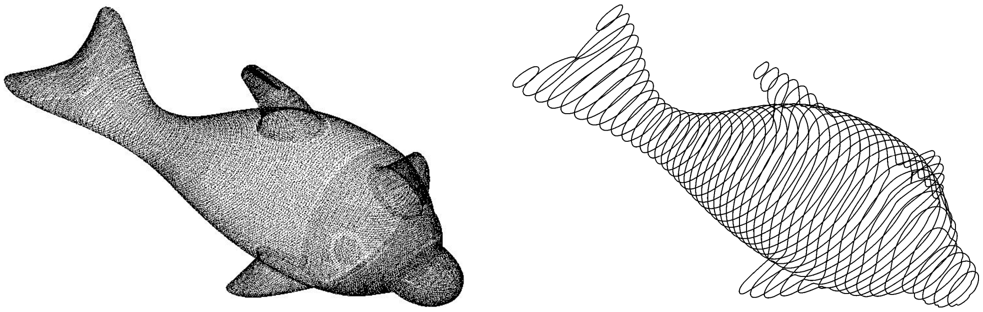
(a) Point Clouds (b) Data Points

Figure 7. *Dolphin*-Shaped Surface

2.2.2 Data points extraction

After the point clouds have already acquired, the results are transformed in the CAD environment of Imageware to delete the noise, subtract the redundancy and so on. Then the data points can be extracted from the sections of point clouds.

In reverse engineering, surface reconstruction is the most important process. But in this modeling technique, the main purpose is to rebuild the space grid structures. In order to get ready for the surface reconstruction and meshing process, the data points should distribute in rectangular topological relationship. But as shown in Figure 5b, each solid line may have different number of data points, and the data points may still distribute scattered. It is necessary to pretreat these data points before the surface reconstruction and meshing process.

3. SURFACE RECONSTRUCTION AND MESHING METHOD

In this section, the cubic B-spline curve will be used to deal with the problem of data points which are not of rectangular topology. Then the re-interpolation reflection meshing method will be used to rebuild the space grid structures. Before the explanation of the procedure, the theory of B-splines will be introduced briefly.

3.1 B-Spline Representation

The definition, important properties and manipulations of B-spline curve and surface are briefly outlined here. The detailed contents can be found in Farin [12] and DeBoor [13].

3.1.1 B-splines interpolation of curve and surface

A B-spline curve is defined by the Eq. 1.

$$\boldsymbol{p}(u) = \sum_{i=0}^{n} \boldsymbol{d}_i N_{i,k}(u) \qquad 0 \le u \le 1, \tag{1}$$

where $N_{i,k}(u)$ are B-spline basis functions, $\boldsymbol{d}_i$ are vectors composed of x, y, z coordinates of the control points, k is the order of a B-spline curve, and $\boldsymbol{U} = [u_0, u_1, \ldots, u_m]$ is the knot vector which specifies the distribution of the parameter u along the curve. The relationship among the order of the curve k, the number of control points n+1, and the number of knots m+1 is given by

$$m + 1 = n + 1 + k + 1 . \tag{2}$$

Figure 8 depicts the non-uniform cubic B-spline curve interpolated by the data points.

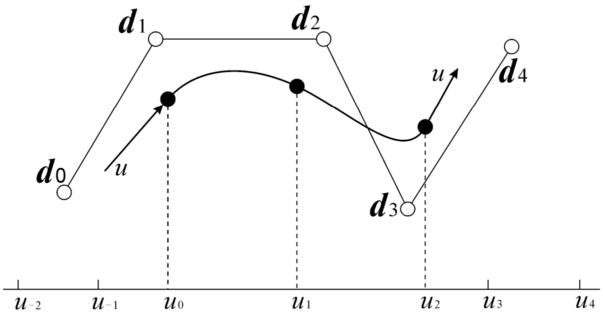

Figure 8. Non-Uniform Cubic B-Spline Curve Fitting

B-spline basis functions $N_{i,k}(u)$ are defined by

$$N_{i,0}(u) = \begin{cases} 1, & \mathit{if}\ u_i \le u < u_{i+1} \\ 0, & \text{otherwise} \end{cases} \tag{3}$$

$$N_{i,k}(u) = \frac{u - u_i}{u_{i+k} - u_i} N_{i,k-1}(u) + \frac{u_{i+k+1} - u}{u_{i+k+1} - u_{i+1}} N_{i+1,k-1}(u), \tag{4}$$

where i is sequence number, k is the order. These recursive formula show that it needs k+2 knots u_i, u_{i+1}, …, u_{i+k+1} to calculate $N_{i,k}(u)$, and the interval $[u_i, u_{i+k+1}]$ is called the support knot span of $N_{i,k}(u)$.

As an extension of a parametric B-spline curve, a biparametric B-spline surface can be defined as the tensor product of B-spline curves. A (k×l)th order B-spline surface is defined as follows:

$$\boldsymbol{p}(u,v) = \sum_{i=0}^{m} \sum_{j=0}^{n} \boldsymbol{d}_{i,j} N_{i,k}(u) N_{j,l}(v), \qquad 0 \le u,v \le 1 \tag{5}$$

where (m+1)×(n+1) control points $\boldsymbol{d}_{i,j}$ build up the control net in 3D, and $N_{i,k}(u)$, $N_{j,l}(v)$ are the B-spline basis functions of order k and l in the u- and v-directions, respectively. Figure 9 shows various geometric entities defining a bi-cubic non-uniform B-spline patch.

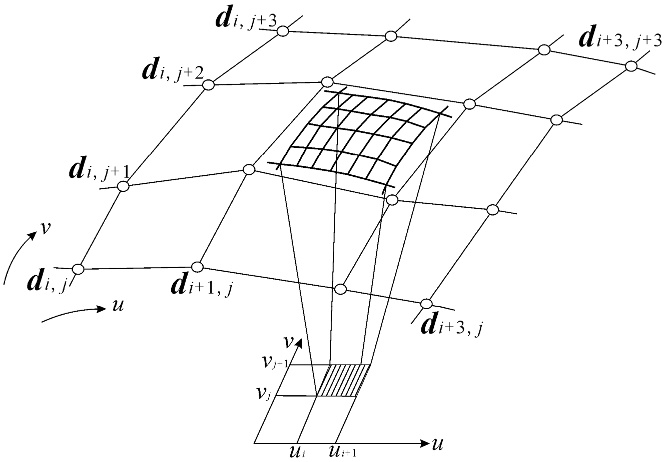

Figure 9. Geometric Configuration Defining a Bi-Cubic NUBS Patch

3.1.2 Evaluation of B-spline surface

The overall procedure of constructing a composite B-spline surface from the input data consists of the following four separate steps:

(1) Determination of knot spans $U = [u_0, u_1, \ldots, u_m]$ and $V = [v_0, v_1, \ldots, v_n]$.
The spline interpolation problem is usually stated as "given data points x_i and parameter values u_i . . .". In practice, parameter values are rarely given and therefore must be made up somehow. The convenient way to determine the u_i is to have the knot spacing proportional to the distances of the data points.

$$\frac{u_i - u_{i-1}}{u_{i+1} - u_i} = \frac{\|x_i - x_{i-1}\|}{\|x_{i+1} - x_i\|}. \tag{6}$$

A knot sequence satisfying Eq. 6 is called chord length parametrization. In the present study, this method is employed.

(2) Determination of intermediate control points.
At this step, a B-spline curve is fitted from each "column" j of the input data. That is, for each column j, sequence mesh points and end boundary tangents are given. The intermediate control points corresponding to the input data are found.

(3) Determination of boundary vectors.
The next step is to determine the boundary vectors from the boundary tangents and corner twist vectors. The boundary tangents can be determined by using data points.

(4) Determination of control vertices $\boldsymbol{d}_{i,j}$.
This step determines the B-spline control points $\boldsymbol{d}_{i,j}$ by fitting a composite B-spline curve from each "row" i of intermediate control points.

In the present study, the B-spline curve or surface is cubic, so the order k or l is three.

3.2 Data Points Manipulations

The B-spline interpolation of surface request data points distribute in rectangular topological relationship. But in the manner of 3D measurement, some data points may not fulfil this requirement. As shown in Figure 10a, the data points distribute in lines, so the problem can be solved with cubic B-spline curve. Through the interpolation, it ensures the number of data points in each line is equal and the data points distribute in rectangular topological relationship. The data points which have been manipulated can be seen in Figure 10b.

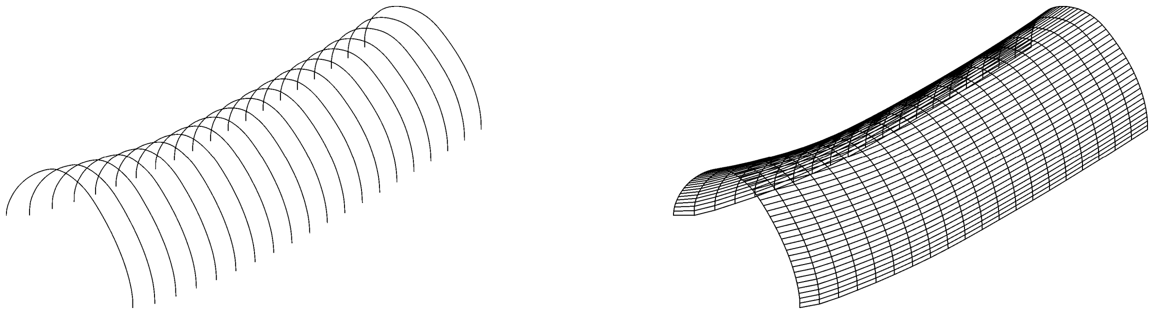

(a) Before Interpolation of B-Spline Curve (b) After Interpolation of B-Spline Curve

Figure 10. Data Points Manipulation

3.3 Re-Interpolation Reflection Meshing Method

A rectangular parameter field has been prepared for the B-spline interpolation of surface, and it is also appropriate for the reflection meshing method to divide the surface. The basic procedure of the reflection meshing method is as follows (Zheng, et al. [14]):

(1) Mesh the rectangular parameter field and get knots (u_i, v_j).

(2) Substituting each knot into Eq. 5, gives the corresponding $p(u_i, v_j)$.

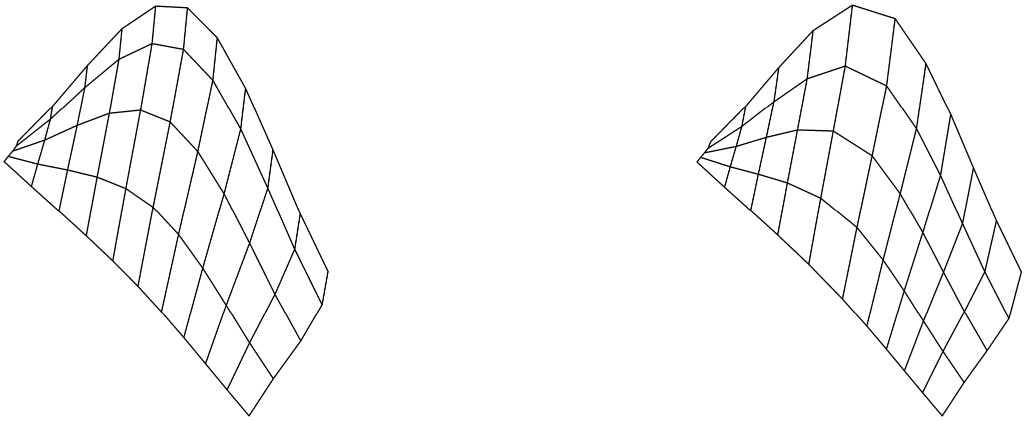

(a) Single Interpolation (b) Re-Interpolation

Figure 11. Comparison of Meshing Methods

Reflection meshing method is very simple, and if the parameter values are given well, it will produce a good division. However, in the process of B-Spline interpolation, the data points are parameterized with chord length parametrization, which is an approximate method compared with the arc length parametrization. If the curvature changes sharp, the parameter values will become anamorphic, and the inherent flaw is that some uneven grids (Figure 11a) will appear in the places where the curvature changes sharp.

Therefore, the re-interpolation reflection meshing method is proposed to advance the prior method. The procedure is as follows:

(1) From the data points, the bi-cubic B-spline interpolation of surface and reflection meshing method are applied to get the output of enough new data points, which are rectangular topology and express the features of the surface clearly.

(2) Put the new data points repeat the above procedure, and the required grids will be acquired.

This approach is similar to the arc length parametrization, and the final grids distribute regular and even. As shown in Figure 11b, grids tend to be more homogeneous.

3.4 Meshing Ways

To facilitate modeling, meshing ways can be designed as the following solutions (Li and Luo [10]):

(1) Rectangular grids:
- Set the number of the round and radial grids. This solution is suitable when the number of grids has been determined.
- Set the expectation of the element length, then the surface can be meshed automatically. It is suitable when the length of the element has been restricted.
- In addition, the grids can be decreased rationally to avoid too many grids centralizing on the top.

(2) Three-dimensional grids:
- Set the number of central round and radial grids.

Take the conical surface for example. The surfaces which are meshed by the above solutions are shown in Figure 12.

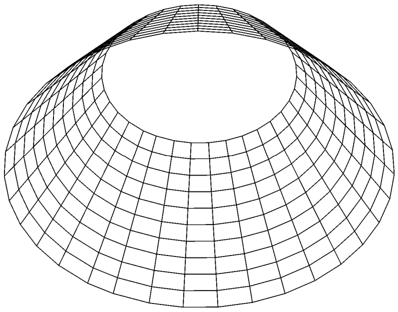

(a) Rectangular Grids: Set Number

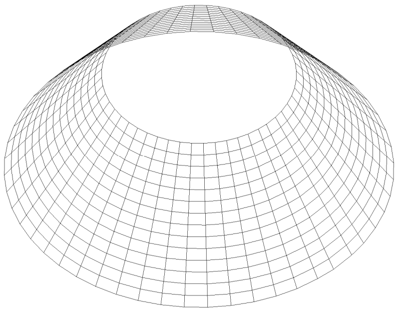

(b) Rectangular Grids: Set Expectation of The Element Length

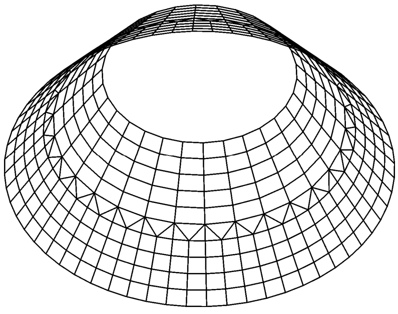

(c) Rectangular Grids: Decrease

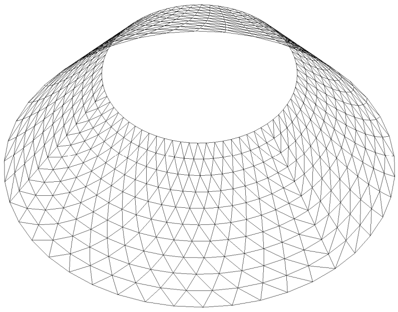

(d) Three-Dimensional Grids

Figure 12. Meshing Ways

3.5 Evaluation Functions of Grid Quality

The perfect space grid structures require that their grids are regular and the lengths of elements are uniform. Therefore, the evaluation functions of grid quality comprise statistical functions of grid shape and element length as follows:

(1) The sample of grid shape is quality coefficient (G_1, G_2, …, G_m), and the mean value is

$$\overline{G} = \frac{1}{m} \sum_{i=0}^{m} G_i \, . \tag{7}$$

The variance is

$$S_G^2 = \frac{1}{m-1} \sum_{i=0}^{m} (G_i - \overline{G})^2 \, . \tag{8}$$

(2) The sample of the element length is (L_1, L_2, …, L_n), and the mean value is

$$\overline{L} = \frac{1}{n} \sum_{i=0}^{n} L_i \, . \tag{9}$$

The variance is

$$S_L^2 = \frac{1}{n-1}\sum_{i=0}^{n}(L_i - \bar{L})^2 . \tag{10}$$

According to statistical theory, these evaluation functions represent the condition of the grid quality. For example, the bigger the mean value of quality coefficient expresses the better the grid shape, and the smaller variance means less difference of grid shape.

4. DESIGN EXAMPLES

There are several design examples to illustrate the above modeling technique for bionic space grid structure as follows:

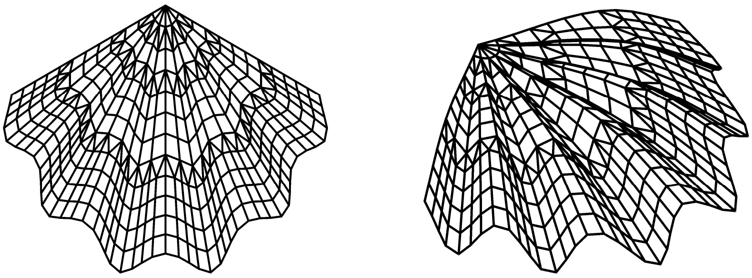

(a) Elevation View (b) Perspective View

Figure 13. *Scallop*-Shaped Space Grid Structure

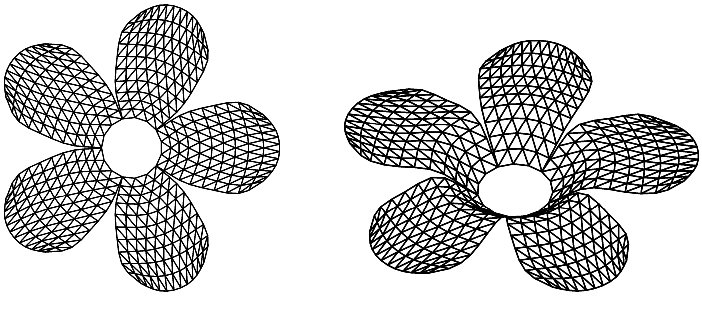

(a) Elevation View (b) Perspective View

Figure 14. *Pilosa*-Shaped Space Grid Structure

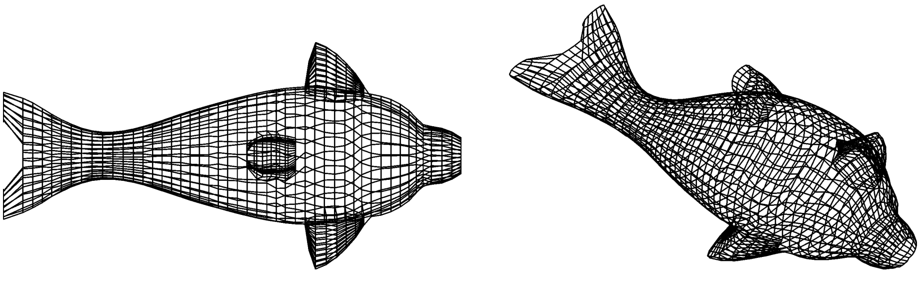

(a) Elevation View (b) Perspective View

Figure 15. *Dolphin*-Shaped Space Grid Structure

(1) *Scallop*-shaped space grid structure (Figure 13)
- Rectangular grids: set grid number.
- Rational decrease on the top.
- The variance of element length: 0.250.

(2) *Pilosa*-shaped space grid structure (Figure 14)
- Three-dimensional grids: set the number of central round and radial grids.
- The mean value of quality coefficient: 0.784.
- The variance of quality coefficient: 0.022.
- The variance of element length: 0.239.

(3) *Dolphin*-shaped space grid structure (Figure 15)
- Rectangular grids: set grid number.
- The mean value of quality coefficient: 0.864.
- The variance of quality coefficient: 0.011.

5. CONCLUSION

When utilizing the modeling technique for bionic space grid structures, there are some conclusions that may be noticed:

(1) The acquisition method of data points derived from either bionics or reverse engineering is effective and convenient to imitate the natural patterns. Especially for complex surface, 3D measurement can be used to get sufficient data points. This is a really new idea to rebuild the bionic structure.

(2) The Imageware has powerful function to reconstruct the surface from data points, but it can not get the practical space grid structures directly. So the most important process of the modeling technique is the re-interpolation reflection meshing method.

(3) The re-interpolation reflection meshing method overcomes the inherent flaw of reflection meshing method. Though the surface obtained from the re-interpolation is not exactly the same as the initial interpolation, with sufficient new data points the output of re-interpolation can express the original surface in enough precision.

(4) The meshing ways and evaluation functions of grid quality adopted in this paper are necessary in the practice.

The bionic space grid structures display vogue and natural beauty, and have great potential application in the future. This rapid modeling technique will be helpful to accelerate the development of the bionic space grid structure.

ACKNOWLEDGEMENT

This study is funded by the Key Program of National Natural Science Foundation of China (No.50638050), the Doctoral Fund (No.20050335097) and the New Century Educational Talents Plan of Chinese Education Ministry (NCET-06-0517). This financial support is gratefully acknowledged.

REFERENCES

[1] Harald, K., “Structural Design of Contemporary Free-form-architecture”, New Olympics New Shell and Spatial Structures, IASS-APCS 2006 Symposium, Beijing, China, 2006.
[2] Stach, E., “Form-optimizing in Biological Structures: the Morphology of Seashells”, Shell and Spatial Structures from Models to Realization, IASS 2004 Symposium, Montpellier, France, 2004.
[3] Raup, D.M., “Computer as Aid in Describing Form in Gastropod Shells”, Science, 1962, Vol. 138, pp. 150-152.
[4] Várady, T. Martin, R.R. and Cox, J., “Reverse Engineering of Geometric Models—An Introduction”, Computer-Aided Design, 1997, Vol. 29, No. 4, pp. 255-268.
[5] Barber, D. Mills, J. and Bryan, P., “Laser Scanning and Photogrammetry: 21st Century Metrology”, CIPA Symposium, Potsdam, Germany, 2001.
[6] Balz, M. and Böhm, J., “Generating Shell Models and Their Realization by Photogrammetric Measurement”, Shell and Spatial Structures from Models to Realization, IASS 2004 Symposium, Montpellier, France, 2004.
[7] Gong, X.Y., “Research on Generating Free Space Surface and Mesh Technology”, Master Degree Dissertation, College of Civil Engineering and Architecture, Zhejiang University, Hangzhou, China, 2004. (in Chinese)
[8] Zhang, H., “Algorithms of Surface Modeling in Spatial Structure and their Program Realization”, Master Degree Dissertation, College of Civil Engineering and Architecture, Zhejiang University, Hangzhou, China, 2005. (in Chinese)
[9] Cen P.C., “Parametric Description and Meshing Algorithm for the Surface of Spatial Structure”, Master Degree Dissertation, College of Civil Engineering and Architecture, Zhejiang University, Hangzhou, China, 2006. (in Chinese)
[10] Li, N. and Luo, Y.Z., “Modeling Method for Bionic Latticed Shell”, International Conference on Steel and Composite Structures, Manchester, 2007, pp.1005-1010.
[11] Luca, L.D. Veron, P. and Florenzano, M., “Reverse Engineering of Architectural Buildings Based on a Hybrid Modeling Approach”, Computers & Graphics, 2006, Vol. 30, pp.160-176.
[12] Farin, G., “Curves and Surfaces for Computer Aided Geometric Design: A Practical Guide”, Academic Press, New York, 1993.
[13] DeBoor, C., “A Practical Guide to Splines”, Springer, New York, 1978.
[14] Zheng, Z.Z. Li, S.J. and Li, Z.G., “Classification and Comparison of Algorithm for Surface Mesh Generation”, Computer Aided Engineering, 1998, Vol. 1, pp. 53-58. (in Chinese)

FATIGUE EXPERIMENTS ON VERY HIGH STRENGTH STEEL BASE MATERIAL AND TRANSVERSE BUTT WELDS

R.J.M. Pijpers[1,*], M.H. Kolstein[2], A. Romeijn[3] and F.S.K. Bijlaard[4]

[1] *PhD researcher, Faculty of CiTG, TU Delft, Delft, The Netherlands;*
Materials Innovation Institute, Delft, The Netherlands
**(Corresponding author: E-mail: r.j.m.pijpers@tudelft.nl)*
[2] *Senior Researcher, Faculty of CiTG, TU Delft, Delft, The Netherlands*
[3] *Associate Professor, Faculty of CiTG, Delft University of Technology, Delft, The Netherlands*
[4] *Professor, Faculty of CiTG, TU Delft, Delft, The Netherlands*

Received: 2 November 2007; Revised: 17 December 2007; Accepted: 24 December 2007

ABSTRACT: Very High Strength Steels (VHSS) with nominal strengths up to 1100 MPa have been available on the market for many years. However, the use of these steels in the civil engineering industry is still uncommon, due to lack of design and fabrication knowledge and therefore limited inclusion in codes. Moreover, in a fatigue loaded VHSS structure absolute and relative stress variation will be higher compared to stresses in structures made of lower grade steels. According to current design codes the fatigue strength of welded connections mainly depends on the applied detail, plate thickness and machining condition, not on steel grade. Recently experiments on plates made of S690 and S1100, with and without transverse butt welds, have been performed in order to study the fatigue strength. Test results show that the characteristic fatigue strengths of plates with and without transverse butt weld lay well above the values according to EN 1993-1-9, mainly because of higher slope of the S-N curves. Crack initiation phase of S1100 specimens is relatively long compared to S690 specimens, while crack propagation is relatively short. An efficient application of VHSS in welded connections requires high fabrication quality and avoidance of large stress concentration in joints.

Keywords: Very High Strength Steel; High Cycle Fatigue; Transverse Butt Welds; Eurocode

1. INTRODUCTION

Very high strength steels (VHSS) have been made available by the steel industry for many years. However, VHSS are still rarely used by manufactures in the field of civil engineering, due to lack of adequate design and fabrication rules for these steels. Table 1 shows examples and typical application of regular structural steel, conventional high strength steel and very high strength steel.

1.1 Background VHSS

Potential advantages by using VHSS are evident. The use would lead to high performance products with, for example, slender and more aesthetic appearance because of reduced cross section and plate thickness. The weights and volumes of structures would be significantly reduced, resulting in novel design possibilities as well as savings in production costs of transportation and erection. Moreover smaller sizes of structures would lead to smaller weld volumes and reduced consumption of welding consumables. Finally, the ecological balance, both for production and application of the high strength steels would be improved by reduction of material, energy consumption and associated pollution.

The emphasis of the current research is laid on the high strength quenched and tempered steels with yield strengths of 690 MPa up to 1100 MPa. These steels obtain their properties through careful control of chemical composition together with appropriate heat treatment including a rapid water quench from 900ºC to room temperature followed by tempering, to form a fine grained martensitic microstructure [1].

Table 1. Typical Examples and Application of Various Steel Types

Strength [MPa]	Description	Other descriptions	Typical examples of grades	Typical Application
<300	Regular structural steel	Mild steel	S235	Buildings
300 - 700	Conventional high strength steel (CHSS)	High performance steel/ High tensile steel	S355/S460	Bridges/High rise buildings/Offshore structures
700 - 1100	Very high strength steel (VHSS)	Ultra high strength steel/ Super high strength steel	S690/S960/S1100	Cranes/Bridges/ High rise buildings

The low alloyed VHSS are still good weldable steels. VHSS material is scarce due to lack of demand for components made of these relatively new materials. Several European steel manufacturers make VHSS plate material with yield strength up to 1100 MPa and plate thickness up to 40 mm. Hot rolled beam cross sections are only available up to 460 yield strength. Circular hollow sections (CHS) are available in yield strength up to 890 MPa and rectangular hollow sections (RHS) up to yield strength of 700 MPa. Table 2 summarises various steel types of plate material, CHS and RHS. Particularly in the civil engineering world design and fabrication rules need to be developed to enable a rising demand for VHSS. In the crane industry, where reduction of material directly influences the structural performance, S690 is already regarded as the standard steel grade, while plates up to strengths of S1100 are more and more daily practice.

High strength steels were initially excluded from the European steel design code Eurocode 3, by limiting the scope to specified yield strengths up to 355 MPa only and by limiting the strength yield ratio $f_u/f_y \geq 1{,}2$. Annex D to ENV-Eurocode 3 has been the door opener for the use of conventional high strength steels (CHSS) with yield strength of 420 MPa to 460 MPa without needing particular technical approvals. Later on, the use of high strength steel up to S690 is allowed by the following part of Eurocode 3: Design of steel structures, Part 1.12 : Additional rules for the extension of EN 1993 to steel grade S700 [2]. Crane code NPR-CEN/TS 13001-3-1 [3] is applicable to design of crane structures with high strength steel grades up to 960 MPa yield strength.

Table 2. Available Quenched and Tempered VHSS

Manufacturer	Name	Yield strength MPa]	Type
Dillinger Hütte GTS	DILLIMAX	690, 890, 960, 1100	Plate material
Thyssen Krupp	N-A-XTRA	700, 800	
	XABO	890, 960, 1100	
SSAB	WELDOX	700, 800, 900, 960, 1100, 1300	
JFE	HITEN	780, 980	
Ilsenburger-Grobblech	MAXIL	690, 890, 960, 1100	
Tenaris	TN 140	960	Circular Hollow Sections (CHS)
Europipe	X100	690	
Vallourec-Mannessmann	FGS	690, 770, 790, 890	
Ruukki	Optim HS 700 MH	700	Rectangular Hollow Sections (RHS)

Three governing design conditions should be fulfilled making use of VHSS in civil engineering structures the most efficient way: 1) VHSS should preferably be designed for lattice structures. Otherwise displacement might be the governing design criterion while not utilising the full material strength of VHSS; 2) In statically loaded structures attention should be paid to deformation capacity of joints, as yield to tensile ratio of VHSS may be close to 1; 3) In fatigue loaded structures use of joints with high stress concentrations should be avoided, whilst choosing high class details and high fabrication quality is required.

The nominal stress in a VHSS structure is usually higher than in a structure made from lower grade steels and stresses due to self weight will be lower. In absolute and relative terms this will lead to higher stress variation due to the variable load. Therefore particularly in fatigue loaded structures, a large part of all civil engineering structures, for instance bridges and offshore structures with a high number of stress cycles during their lifetime, the benefits of using VHSS are questionable if the structural design entirely depends on the fatigue strength.

In 2006 TU Delft initiated the research project ‘Very High Strength Steels for Structural Applications’ which will investigate possibilities for future application of these steels in the field of civil engineering. The main objective of the project is to supply the steel construction industry with information relevant for the design and fabrication of VHSS structures. The research work comprises an experimental and numerical study on the fatigue resistance of welded VHSS connections. The current paper presents the first research phase, an experimental study on the fatigue strength of plates made of S690 and S1100 with and without transverse butt welds [4,5].

1.2 Literature Review

Gurney [16] concluded that the higher the yield strength of base materials the more sensitive the fatigue strength of the material becomes to both the presence of notches and to the surface condition. In case of low notch values ($K_t \approx 1$) notch sensitivity of high strength steel fatigue strength is minimized. Most literature data show a linear relation between tensile or yield strength and base material fatigue strength [16,17] . The mean fatigue strength is expressed as an endurable stress range at a particular number of cycles $\Delta\sigma_{mean}$. In most cases this number of cycles is taken as $2*10^6$ resulting in the $\Delta\sigma_{mean;2*10^6}$.

In welded VHSS structures the fatigue strength is said to be equal to lower strength steels because in VHSS micro cracks are already present due to welding, while crack propagation depends on stress range, being independent of yield strength [16,17,18]. Hübner [19] investigated the fatigue strength of S960 and gives experimental results on as-rolled base material. In Figure 2 a comparison of the $\Delta\sigma_{mean;2*10^6}$ is given for plain machined specimens, millscale, as-rolled specimens and transverse butt welds, as a function of the tensile strength R_m. It shows, the more the geometry and surface condition degrade, the less effective a higher R_m will be on the fatigue strength. Wellinger and Dietmann [20] describe the influence of surface roughness on fatigue strength, by relating the ultimate tensile strength of the base material to the surface roughness depth. In case of high surface roughness depth, i.e. as-rolled specimens, the relative reduction in fatigue strength increases with ultimate tensile strength of the steel. The better the surface treatment, i.e. grinding or polishing, the better the relative fatigue strength of the higher strength steels will be compared to regular steels. In practice however machining critical details is time consuming, especially for large structures.

In 2005 members of working commission 2 (Steel, Timber and Composite Structures) of the International Association of Bridge and Structural Engineering (IABSE) initiated a state-of-the-art document [6] on the use and application of High Performance Steel (HPS, σ_y <690 MPa). In this document worldwide research is included. American design experience leads to application of High Performance Steels in bridges. Canadian fatigue research showes no clear advantage of High Performance Steels over mild steel. In Japan Bridge High-Performance Steel is developed, which in combination with so called Low Transition Temperature welding may increase fatigue strength of welded joints. From European research on fatigue strength of HPS can be concluded that by improvement of the weld connection quality, for instance by reduction of surface defects or application of post-weld treatments, higher fatigue strengths can be achieved.

The German steel journal Stahlbau pays special attention to research on high strength steel in [7,8,9]. A research project relating to the fatigue classification of high strength steel is the project 'Efficient Lifting Equipment with Extra High Strength Steel' (LIFTHIGH), initiated by the ECSC [8]. The main research topic is the fatigue behaviour of welded high strength steel details (σ_y <1100 MPa). Results show that in case of specimens with low stress concentration the use of high strength steel may result in higher fatigue strength compared to regular steel connections.

In [10] the use of high strength steel in crane structures is discussed. The paper shows fatigue results on base materials, welded and post weld treated joints of S355, S690 and S960. In the project 'Effizienter Stahlbau aus höherfesten Stählen unter Ermüdungsbeanspruchung' initiated by the Arbeitsgemeinschaft industrieller Forschungsvereinigungen 'Otto von Guericke' (AiF), the University of Stuttgart, Bauhaus University of Weimar and the Fachhochschule München, emphasis is laid on the use of weld improvement techniques for high strength steel connections [11]. According to [11] use of ultrasonic peening may increase the characteristic fatigue strength at 2 million cycles of welded transverse stiffners made of S460 with 40 up to 100%. Ultrasonic peening proves to be even more effective at stiffners made of S690.

Compared to other welded details described in codes, the transverse butt weld detail has a relatively high fatigue classification. The design fatigue curve of EN 1993-1-9 [12] is only valid if the geometry of the welded detail is valid by the requirements for execution of steel work according to prEN 1090-2 [13], which includes hot-rolled, structural steel products up to S960. The S1100 steel is thus out of the scope of this code. According to EN 1993-1-9 [12] the fatigue design strength at 2 million cycles of a transverse butt weld detail, see Figure 1, is 90 MPa. The following criteria account for this detail class: transverse splices in plates or flats; weld run-on and run-off pieces to be used and subsequently removed; plate edges to be ground flush in the direction of stress; welded from both sides in flat position; NDT applied. For the Eurocode classification a background document is available. According to crane code CEN/TS 13001-3-1 [3] the fatigue strength of a quality C butt weld is 140 MPa. Backgrounds on the classification of the details in the crane code are not known to the authors.

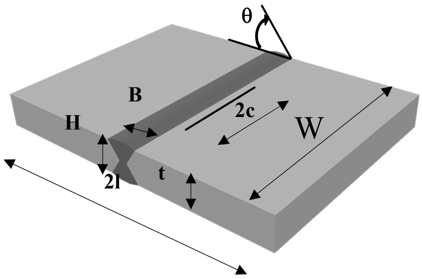

Figure 1. EN 1993-1-9 [12] Detail Category 90

Demofonti et al [14] performed axial fatigue tests on plates with 10 mm transverse butt welds made of S355 up to S960. In the investigation no significant strength differences under constant amplitude loading were found in favor of use of higher steel strengths, although advantages for the S960 steel could be noticed in case of variable amplitude loading. Machining of welds, in order to achieve low notch factors is found to give an advantage for high-strength steels.

Bergers et al. [9] performed fatigue experiments on various 6-8 mm plate V-shaped butt weld connections made of S690, S960 and S1100. For all steel grades the characteristic fatigue strength values lay above the values of EN 1993-1-9 [12] Resulting S-N curves show a slope m = 5 for S1100, which is higher than the value of m = 3 used in the design codes suitable for lower strength steels.

In Figure 2 the results of [9,14,16,17] are presented as $\Delta\sigma_{mean;2*10^6}$ as a function of R_m.

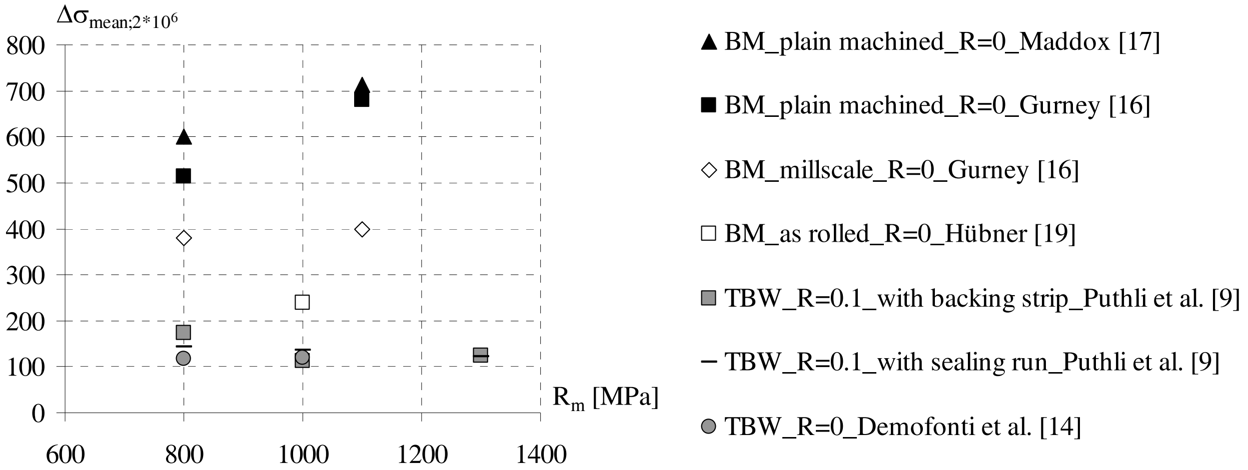

Figure 2. Fatigue Strength of Base Materials (BM) and Transverse Butt Welds (TBW)

2. TEST SETUP AND SPECIMEN SPECIFICATIONS

Tensile and fatigue tests have been performed at the Stevin Laboratory of the Delft University of Technology using a 600 kN dynamic servo hydraulic test rig, see Figure 3.

Figure 3. 600 kN Dynamic Servo Hydraulic Test rig of the Stevin Laboratory, TU Delft

2.1 Plate Material Properties

In the current research the fatigue strength of plates with and without transverse butt welds made of Naxtra M70 (S690) and Weldox S1100E (S1100) is determined. Table 3 and Table 4 give the specifications of the plate material.

Table 3. Test Material

	Steel supplier:	Grade
Naxtra M 70	Thyssen Krupp	S690
Weldox S1100 E	SSAB	S1100

Table 4. Chemical Composition

Grade	C	Si	Mn	P	S	Cr	Mo	Ni
Naxtra M 70	0.16	0.19	0.87	0.012	0.002	0.33	0.22	0.06
Weldox S1100 E	0.16	0.23	0.86	0.007	0.002	0.6	0.586	1.89
Grade	V	Nb	Al	Ti	Cu	N	B	CE
Naxtra M 70		0.026	0.085			0.0038	0.002	0.42
Weldox S1100 E	0.029	0.02	0.066	0.004	0.04	0.005	0.002	0.679

For tensile tests standard test pieces have been used. Two displacement meters (POD meters) and two strain gauges (FLA-6-11) have been attached to the test specimens. Figure 4 shows the tensile test specimens and the position of the POD meters. Table 5 summarises the tensile test results compared to data from the material specifications. The S690 specimens have been plasma cut. The S1100 specimens have been tested in a plasma cut and water cut condition. Yield strength and tensile strength of the S690 specimens is consistent with the manufacturer data. The measured values of the S1100 specimens are 12% lower than expected for the yield strength and 25% for the tensile strength when compared to the material specifications. All tensile test specimens have been cut from the plates that were welded for the fatigue specimens, after welding. Differences in measured strength and manufacturer data may be due to the fabrication influence. The Youngs modulus derived from the tensile tests is used in stress calculations in the fatigue tests using Hooks law.

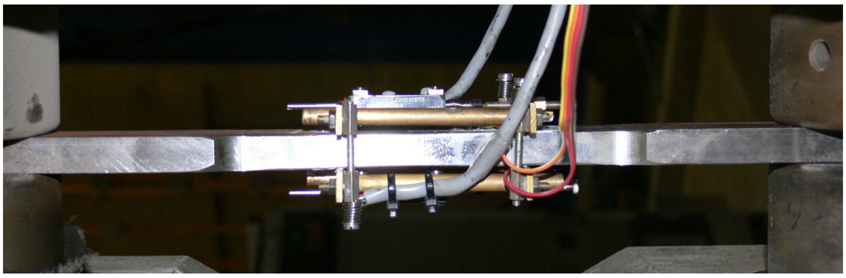

Figure 4. Tensile Test Specimen (90° Rotated)

Table 5. Tensile Test Results

Series	Grade	#	R_{eh}	R_m	R_{eh}/R_m	A	Z	E	Preparation
Measured			MPa	MPa	-	%	%	MPa	
1	S690	3	733	787	0.93	17	0.43	$2.04*10^5$	Plasma cut
2	S1100	3	1086	1135	0.96	11	0.57	$2.02*10^5$	Plasma cut
3	S1100	3	1117	1187	0.94	-	0.55	$2.04*10^5$	Water cut
Data sheet									
1	S690	-	800	830	0.96	16	-		
2	S1100	-	1197	1432	0.84	11	-		

2.2 Fatigue Test Procedure

During the force controlled fatigue tests the stress ratio is kept constant at a relatively low frequency. In the crack propagation phase tests of the small base material specimens runned displacement controlled. Table 6 summarises the fatigue test conditions.

Table 6. Fatigue Test Conditions

Loading	Constant amplitude, Axial
Stress ratio, R	0.1
Frequency	5.3 Hz

In general when determining the fatigue strength two phases can be distinguished: crack initiation and crack propagation. Until crack initiation, the first phase, mean strain and strain range data are stored. In case of crack growth near strain gauges this is immediately reflected in strain gauge data.

Figure 5 shows the monitoring of crack initiation by strain gauge measurements. In the graph the strain range values of two strain gauges are mentioned, strain gauge 1, near which a crack has initiated, and strain gauge 2 on the back side. Absolute stress values differ because of misalignment present in the strip specimens as a result welding, which causes additional bending stresses. The number of cycles N_i at which strain gauge data start to bend of the regular scheme, clearly visible in the graph, is in the current research defined as crack initiation.

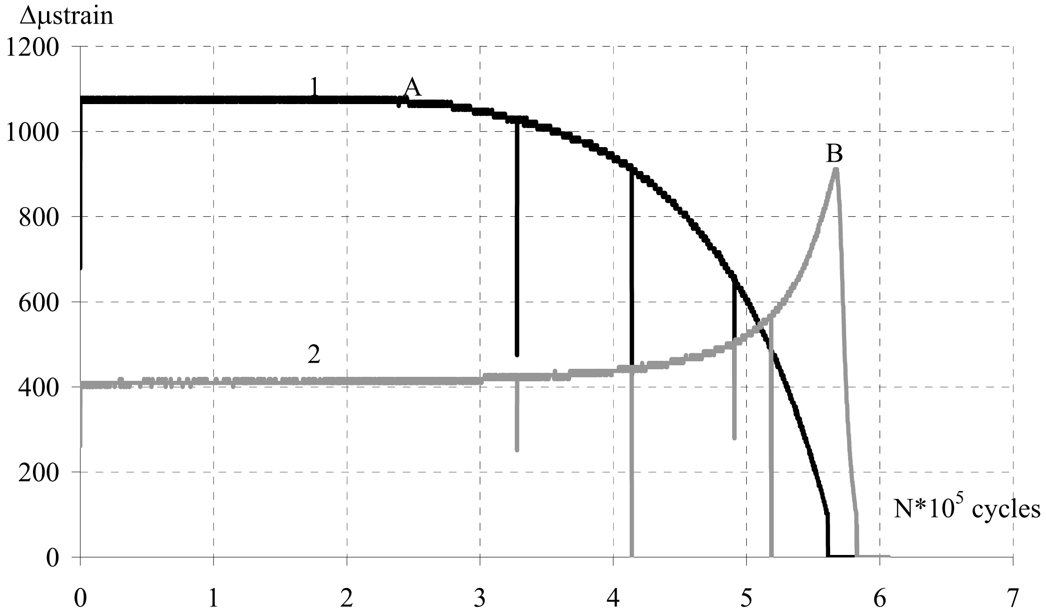

Figure 5. Strain Range Measurements of S690 Specimen FA5

An alarm system immediately shuts off the system at 10% deviation of strain ranges or strain average values, which makes it possible to indicate the locations of crack initiation. When a crack initiates the strain range values of the strain gauges near the crack decrease while the values of the strain gauge on the opposite side of the plate increase. If the crack reaches the full depth of the plate the strain range values immediately decrease, see Figure 5, point B at strain gauge 2.

The second phase of the fatigue test procedure involves the visual inspection of crack development. A liquid (petrol) is put on the crack, which bubbles if the cracks are present. Crack propagation in plate width direction and plate thickness direction is monitored visually. Manually markings are put on the test specimens linking the numbers of stress cycles and corresponding crack lengths. For determination of crack length in specimen thickness direction, if not visible, the procedure of crack marking is used. During crack marking, about 10% cycles of the expected total number of cycles until failure, the upper fatigue loads are kept constant and the lower loads are increased to 90% of the upper loads. In this way boundary lines will occur, which makes it possible to determine the crack growth, when inspecting the fracture surface at the end of the experiment.

Figure 6 shows the crack marking pattern on one of the S1100 base material specimens. In the current research the crack marking method only worked on the S1100 specimens with semi-elliptical (surface) cracks. Quarter-elliptical cracks initiating from the sides of the S690 base material specimens could not be made visible by crack marking.

In the current work the number of cycles, N_f, until a crack reaches a length of 10 mm, is defined as failure of the test specimen. In most cases this means through thickness cracking, followed by unstable crack growth because of the small size of the test specimens, with plate thicknesses of 10 and 12 mm.

Figure 6. Cross Section of S1100 Specimen Showing Crack Marking Boundary Lines

2.3 Base Material Fatigue Specimens

The base material fatigue specimens have been water cut from initially welded steel plates, used for transverse butt weld specimens. After cutting, the specimens have been milled, resulting in a radius of 3 mm at the edges in order to prevent crack initiation from the side. At the middle the specimens have been instrumented with 4 strain gauges, see Figure 7.

Crack initiation was likely to occur at the 10% tapered cross section near these strain gauges. Extra strain gauges at 80 mm from the middle were used to give insight in the misalignment in the test specimens causing strains during clamping into the test rig. Table 7 gives details on the base material fatigue specimens.

Table 7. Geometry and Instrumentation of Base Material Fatigue Specimens, See Figure 7

Steel type	S690	S1100
Number of test specimens	6	6
Number of strain gauges	4	4
Thickness [mm]	12	10
Width [mm]	40	40
Machining	Water cut; edges milled and ground	Water cut; edges milled and ground

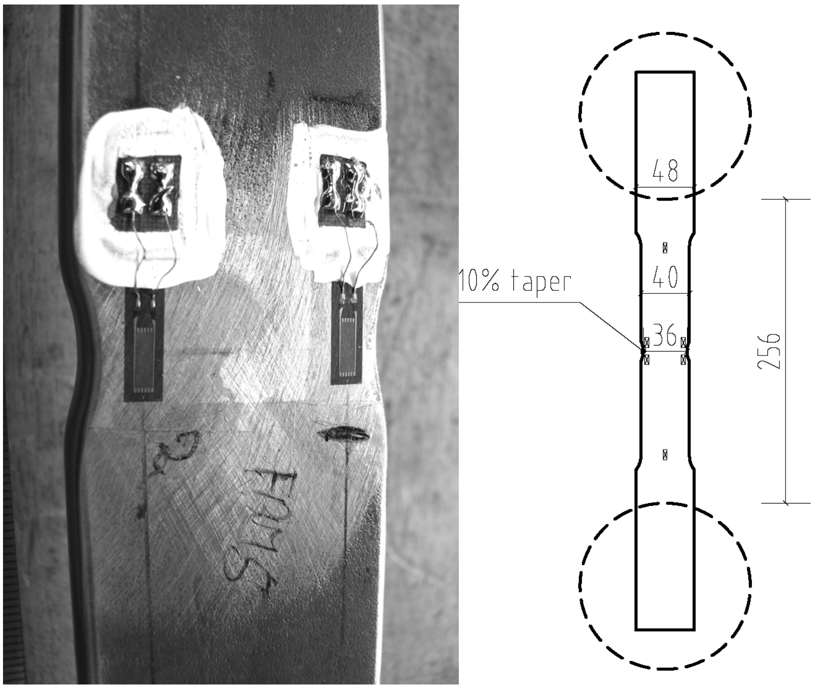

Figure 7. Base Material Fatigue Specimens

2.4 Transverse Butt Weld Specimens

The geometry of the transverse butt weld specimens was chosen to meet the qualifications of a class 90 butt weld detail according to EN 1993-1-9 [12] in the as-welded condition. In total thirteen test specimens have been tested; six made of S690, seven made of S1100.

Table 8 specifies the geometry of the transverse butt weld specimens and gives additional information on the weld parameters.

Table 8. Geometry and Instrumentation of Transverse Butt Weld Specimens, See Figure 1

Steel type	S690	S1100
Number of test specimens	6	7
Number of strain gauges	14	14
Thickness t [mm]	12	10
Length 2l [mm]	750	1000
Width W [mm]	120	100
Machining	Plasma cut; edges ground	Plasma cut; edges ground
Weld metal	Megafill 742M	Tenacito 75 (root) & SH NI 2 K 140
Weld process	FCAW	SMAW
Number of weld layers	5	9
Condition	Overmatched	Undermatched

Edges of the specimens are flame cut and ground afterwards. The X-weld shape is clearly indicated in Figure 8, which also shows Vickers Hardness test results measured at 2 mm below te surface. In the region of the heat affected zone of the S690 cross section a local hardness drop is found, whereas in the fusion zone of the S1100 specimens lower HV10 values are found, indicating the undermatched weld metal.

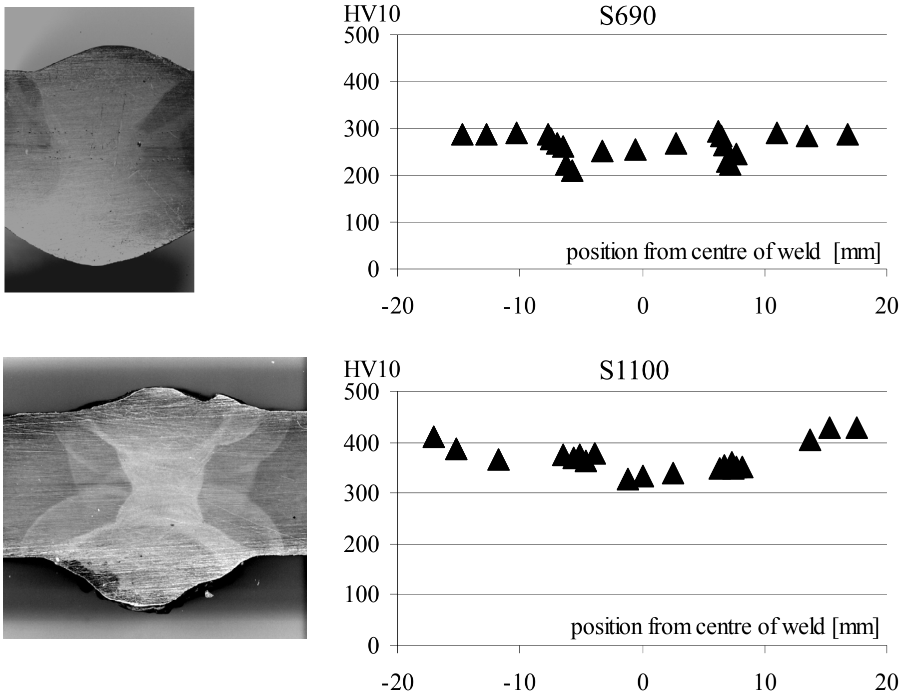

Figure 8. Cross Section of S690 and S1100 Welds and HV10 Values at 2 mm below the Specimen Surface

Figures 9 and 10 show the geometry and instrumentation of the S690 transverse butt weld specimens. In general the dimensions of the S690 specimens are identical to the S1100 specimens. The width of the test specimens is taken ten times the thickness of the plate material. The edges of the welded plates have been ground in order to reduce the chance of crack initiation at these edges.

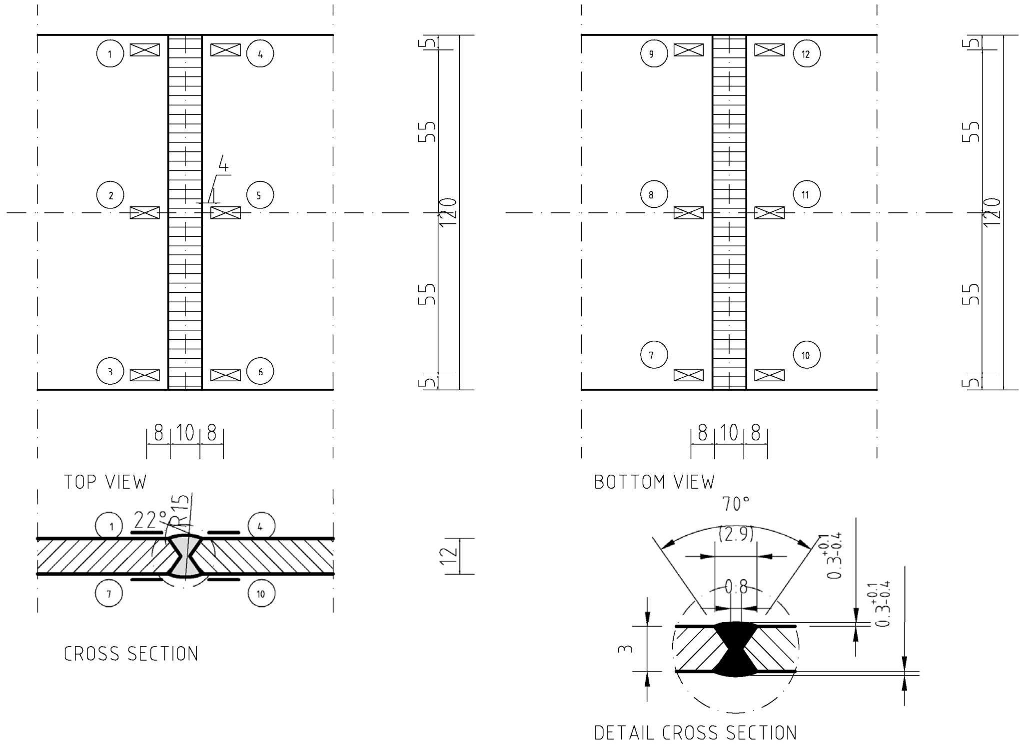

Figure 9. Instrumentation of S690 Transverse Butt Weld Fatigue Specimens

Each specimen contains strain gauges (FLA-6-11) on both sides, at 8 mm from the weld toe to measure the strain distribution in plate width direction. Some of the specimens have been instrumented with special strain gauges (FXV-1-11-002LE) for the determination of stress concentration near the weld toe.

Figure 10 shows transverse butt weld specimens with extra strain gauges on the plate length for the determination of misalignment.

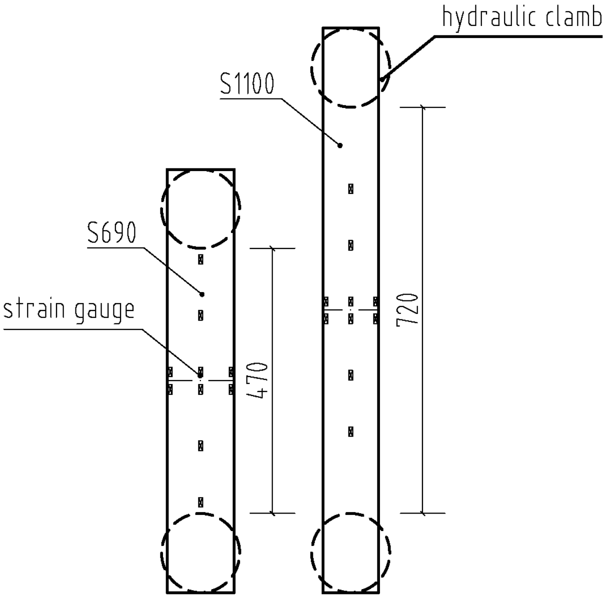

Figure 10. Transverse Butt Weld Fatigue Specimens

In order to check the strain distribution in the plate length direction the specimens have been statically loaded up to stress levels of 30% of the yield strength. Figure 11 shows the longitudinal stress pattern for various applied forces at six strain gauge positions. The measured values are the average tensile stresses at the top of the specimens near the weld, at 100 mm and 200 mm from the weld and at the middle of the plate.

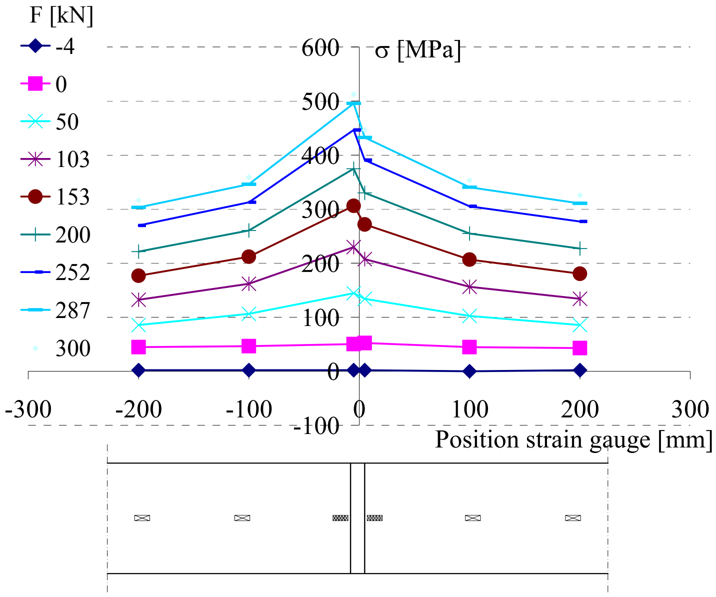

Figure 11. Longitudinal Stress Pattern

Non-linear behaviour of the stresses in longitudinal direction can be explained as follows. Due to shrinkage after welding the test specimens are all bent along the axis of the weld. This causes a non-linear behaviour of the stresses as a result of increasing the tensile load when the specimens are clamped in the test rig. At high stress levels the test rig straightens the test specimens.

Hobbacher [21] gives calculation rules, Eq. 1, Eq. 2 and Eq. 3, for a stress magnification factor, k_m, in case of misalignment in transverse butt welded plates. Figure 13 illustrates the geometrical parameters used in these formulas.

$$k_m = 1 + \frac{3y}{t} \cdot \frac{\tanh(\frac{\beta}{2})}{(\frac{\beta}{2})} \tag{1}$$

in which $\beta = \frac{2l}{t} \cdot \sqrt{\frac{3 \cdot \sigma_m}{E}}$ (2)

$$\sigma = k_m * \sigma_m \tag{3}$$

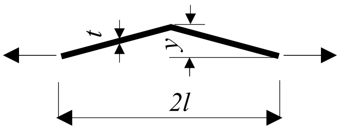

Figure 12. Misalignment Parameters After Hobbacher [21]

The formula also shows the influence of the nominal stress level σ_m on the misalignment factor. At high stress levels the effect of secondary bending stresses is large compared to low stress levels. Measured stress values at 4 mm from the weld toe are compared to calculated stress values σ according to Eq. 3. The stress measurements of both the S690 and the S1100 welds are in good correspondence with the calculated results.

Table 9 summarizes local geometry details of all fatigue tested specimens. The table gives minimum values of weld width B, measured and calculated values of the excess of weld metal h (see Figure 13) and the misalignment parameter y (see Figure 12). prEN 1090-2 [13] limits the excess of weld metal at transverse butt welds quality C according to EN-ISO 5817 [22], see Eq. 4 and Figure 13.

$$h < 1 + 0.15 * B \quad \text{[mm]} \tag{4}$$

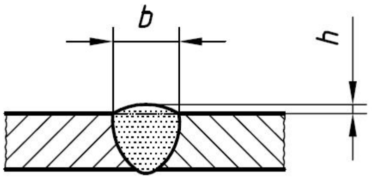

Figure 13. Weld Metal Excess According to EN-ISO 5817 [22]

In test specimen FA2 made of S690, for which code prEN 1090-2 [13] is valid, and in all specimens made of S1100 the weld metal excess value has been exceeded. The yield and tensile strength of the weld material are lower than the plate material strength of S1100. Therefore the undermatched S1100 welds have been made thicker than allowed according to prEN 1090-2 [13].

Table 9. Local Geometry Fatigue Specimens, See Figures 1, 12 and 13

	specimen	B_{min}	h	h	y
			measured	calculated	
		mm	mm	mm	mm
S690	FA1	10	2.5	2.5	4
	FA2	10.3	2.9*	2.5	-
	FA3	8	1.2	2.2	5
	FA4	9	1.3	2.4	2.5
	FA5	7	1.3	2.1	7
	FA9	9	1.5	2.4	4.5
S1100**	FB1	10	3.0*	2.5	6
	FB2	11	2.8*	2.7	3.7
	FB3	9	3.5*	2.4	7
	FB4	13	3.0*	3.0	7
	FB5	12	2.5*	2.8	8
	FB6	11.5	2.7*	2.7	8
	FB9	11	3.3*	2.7	7.5

* value does not satisfy EN-ISO 5817 [22]
**material out of scope of prEN 1090 [13]

3. FATIGUE TEST RESULTS

The current chapter presents crack growth data and S-N curves as a result from fatigue tests.

3.1 Fatigue Tests Base Materials

At all S690 specimens cracks initiated from the taper location, where the average stress level was 10% higher than in the cross section out of the tapered part. In the S1100 specimens, 10% tapered as well, cracks initiated at the cross section outside the taper location. Crack growth in plate thickness direction of both S690 and S1100 base material specimens is illustrated by Figure 14.

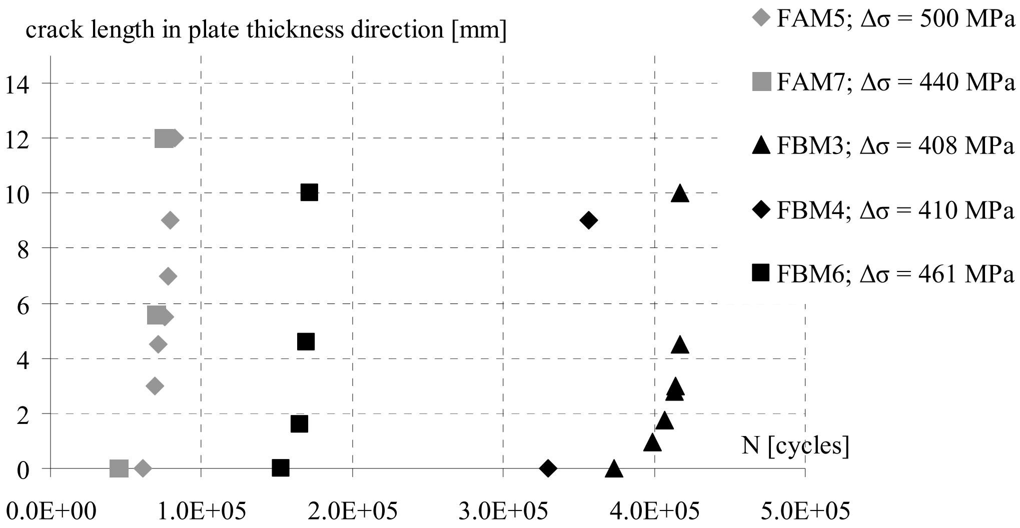

Figure 14. Crack Growth of Base Material Specimens

Most of the cracks in the S690 specimens initiated form the edges at the tapered cross section. At the S1100 specimens cracks initiated at the surface, outside of the tapered cross section. In only few S690 specimens crack propagation could be monitored properly, because the crack marking method gave no visible crack boundary lines of the fracture surface. Next to that the N_f is very close to the N_i at various stress levels, which indicates rapid crack growth after crack initiation.

According to Hobbacher [21] the characteristic stress range values at 2 million cycles, $\Delta\sigma_c$, are calculated for a 95% survival probability on a two-sided confidence level of 75% of the mean, based on Eq. 5. The number of test pieces is small; therefore the value of k is set to 3, which is a safe approximation. In Table 10 the fatigue results of the base material specimens are listed.

$$\log N_c = (a - k * Stdv) + b * \log \Delta\sigma_c \tag{5}$$

Figure 15 shows the results of the base material fatigue tests presented as a S-N curve, based on nominal stress ranges versus number of cycles until failure. As can be seen at Figure 15 the S690 characteristic fatigue values are well above class 160 of EN 1993-1-9 [12] and class 225 of the NPR-CEN/TS 13001-3-1 [3] in the high cycle fatigue region, mainly because of higher slope values.

Table 10. Fatigue results base material specimens

	Specimen	$\Delta\sigma$	N_i ($*10^5$)	N_f ($*10^5$)
		MPa	cycles	cycles
S690	FAM2	270	-*	44*
	FAM3	511	-	1.5
	FAM4	414	55.8	56.3
	FAM5	500	0.6	0.8
	FAM6	450	2.9	3.3
	FAM7	440	0.5	0.8
S1100	FBM1	587	-	0.7
	FBM2	459	-	2.0
	FBM3	408	3.7	4.2
	FBM4	410	3.3	3.6
	FBM5	378	-*	25.0*
	FBM6	461	1.5	1.7
*No crack initiation				
	S690		S1100	
$\Delta\sigma_{mean;2*10^6}$	399		339	
$\Delta\sigma_c$	391		317	
m	13.3		6.8	
#specimens	5		6	

The scatter in the S690 and S1100 results is relatively small. The calculated $\Delta\sigma_c$ level of the S690 specimens is 391 MPa, which is much higher than the S1100 value of 317 MPa, while initially a higher value for the S1100 specimens was expected. Surface roughness influence could be the cause for the different crack initiation locations.

The surface at the tapered cross section has been ground for application of strain gauges. In the locations outside of the tapered cross section, except from the edges, the as-rolled condition applies for the surface condition, having a higher surface roughness. Apparently the S1100 material is more sensitive to this higher surface roughness, causing earlier crack growth at locations with higher surface roughness at a relatively lower stress level.

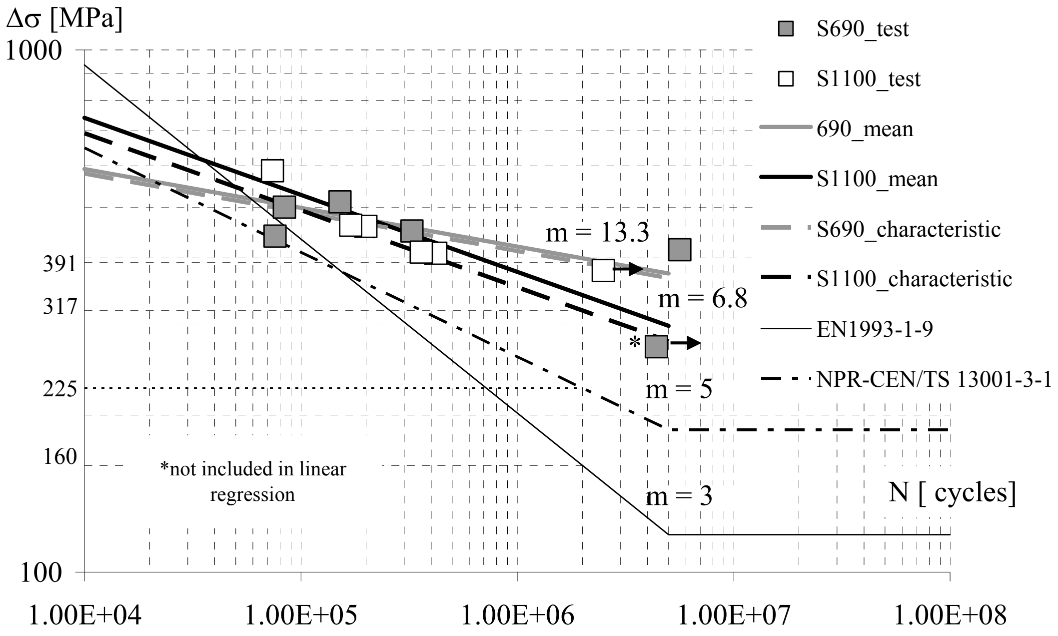

Figure 15. S-N Curve of Base Material Specimens

3.2 Fatigue Tests Transverse Butt Welds

Figure 16 shows the crack propagation in the plate thickness direction of S690 and S1100 specimens, tested at various stress levels. Except from the FA4 specimen of S690 in all specimens cracks have initiated from the plate edges near the weld toe. In the FA4 specimen cracks occurred at multiple locations, also at the surface near the weld toe.

In two specimens no cracks have occurred at high number of cycles; in one of the S690 specimens at a stress range of 110 MPa and in one of the S1100 specimens at a stress range of 200 MPa. At similar stress range level a comparison of crack growth behaviour between S690 and S1100 specimens can be made, for instance when looking at specimens FA5 (S690) and FB5 (S1100), loaded up to a comparable stress range level. The crack initiation phase of FB5 compared to FA5 is relatively long, while the crack propagation is relatively short, see Figure 16.

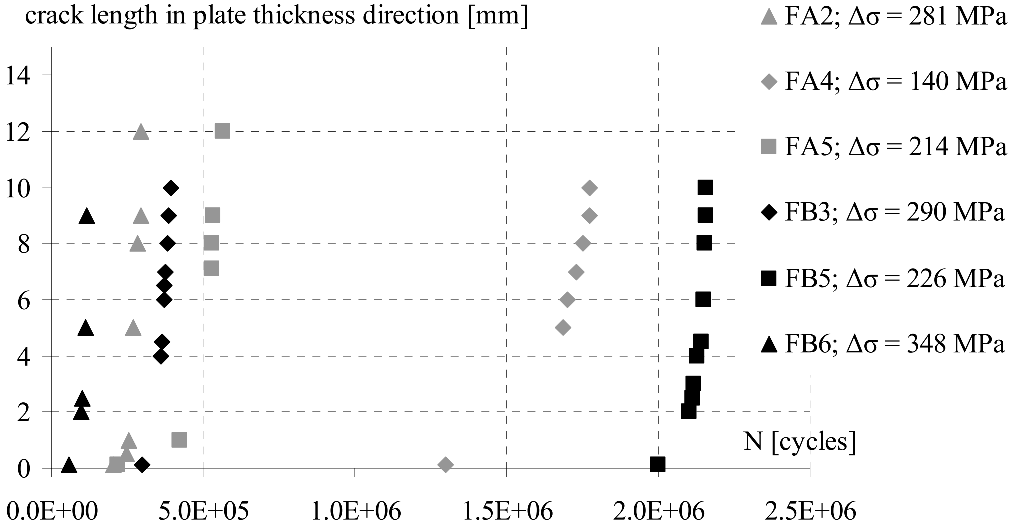

Figure 16. Crack Growth of Transverse Butt Weld Specimens

As for the base materials, the fatigue data of the transverse butt welds is evaluated according to Hobbacher [21].

Based on Eq. 5, the characteristic stress range values at 2 million cycles, $\Delta\sigma_c$, are calculated for a 95% survival probability on a two-sided confidence level of 75% of the mean. The value of the k is set to 3, which again is a safe approximation because of the relatively low amount of test specimens. In Table 11 the fatigue results of the transverse butt weld specimens are listed.

Table 11. Fatigue Results Transverse Butt Weld Specimens

	Specimen	$\Delta\sigma$	N_i ($*10^5$)	N_f ($*10^5$)
		MPa	cycles	cycles
S690	FA1	110	-*	47.0*
	FA2	281	2.0	3.0
	FA3	275	2.4	3.4
	FA4	140	13.0	18.0
	FA5	214	2.2	6.0
	FA9	132	13.0	24.1
S1100	FB1	200	-*	80.0*
	FB2	512	0.1	0.2
	FB3	290	3.0	4.1
	FB4	268	1.5	3.0
	FB5	226	19.0	21.4
	FB6	348	0.6	1.2
	FB9	246	0.8	2.1

*No crack initiation

	S690	S1100
$\Delta\sigma_{mean;2*10^6}$	143	212
$\Delta\sigma_c$	92.5	180
m	2.8	5.7
#specimens	6	7

Figure 17 shows the results of the transverse butt weld fatigue tests, presented in an S-N curve. The calculated $\Delta\sigma_c$ of the S690 specimens is 92 MPa, which is in good correspondence with a high quality butt weld of regular steel, equal to class 90 of EN 1993-1-9 [12] but is lower than $\Delta\sigma_c$ according to class 140 of NPR CEN/TS 13001-3-1 [3]. The slope value m of the S-N line of 2.8 is lower than the slope value of 3 according to both codes.

The results of the S1100 material show a fatigue behaviour different from the S690 material. The slope m of 5.7 is higher than the value of 2.8 of the S690 specimens, which is consistent with research results of Puthli et al. [9]. The calculated $\Delta\sigma_c$ level of the S1100 specimens is 180 MPa, which is also much higher than the S690 value.

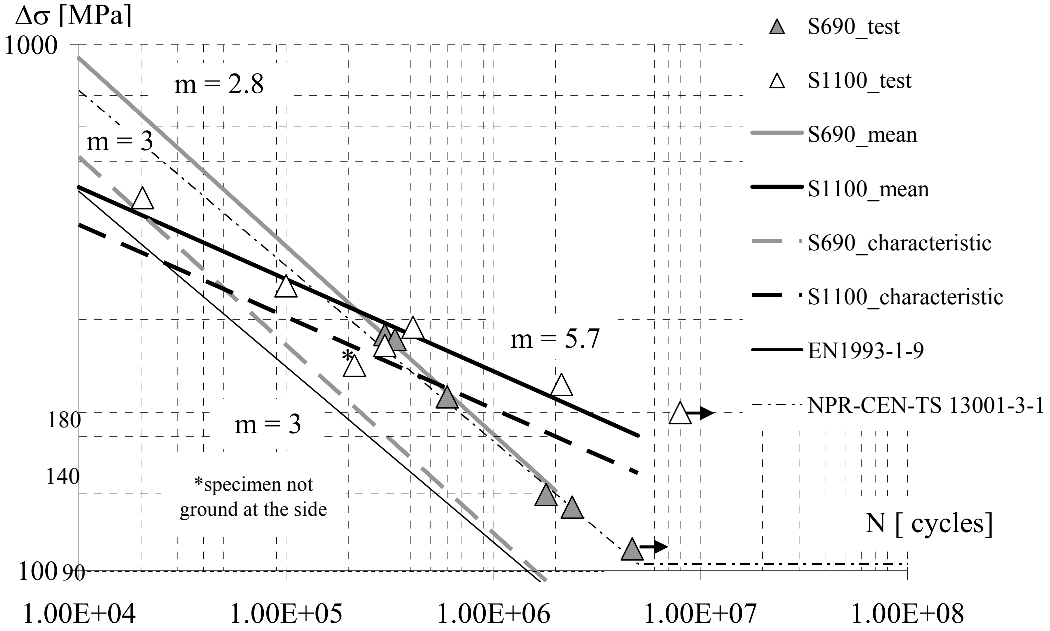

Figure 17. S-N Curve of Transverse Butt Weld Specimens

4. CONCLUSIONS

When applying S1100 in civil engineering structures it should be noticed that high fabrication quality is essential for obtaining the expected yield and tensile strengths. Especially S1100 material is very sensitive to thermal influence and surface condition.

The current research gives experimental results on the fatigue strength of plates with and without transverse butt welds. As EN 1993-1-12 [2] makes EN 1993-1-9 [12] applicable to steels up to yield strength of 700 MPa, the experimental data of the S690 specimens could be compared to this code. The characteristic fatigue strength of the S690 specimens lays well above the presented value of EN 1993-1-9 [12], mainly because of higher slope value in the S-N curve. The tests on as-rolled VHSS specimens show a relatively higher fatigue strength of S690 specimens in relation to the S1100 specimens. Cracks of S1100 specimens initiated outside the 10% tapered cross section, whereas the cracks of the S690 specimens initiated from the edges at the tapered cross section. Therefore the lower fatigue strength of the S1100 specimens is probably due to the surface roughness influence.

From experimental data of VHSS transverse butt weld specimens can be concluded that specimens made of S1100 have a higher characteristic fatigue strength than specimens made of S690, mainly because of a higher slope in the S-N curve. The characteristic fatigue strength of the S690 specimens was very close to the value of EN1993-1-9 [12] class 90.

Crack growth is monitored visually. Because of the low amount of crack propagation data of the base material specimens a comparison of crack growth between S690 and S1100 could not be made. The crack growth data of transverse butt weld specimens show, while the crack initiation phase is very long, crack propagation of the S1100 specimens is relatively short compared to the S690 specimens.

For future design recommendations making effective use of VHSS in fatigue loaded structures it will be necessary to optimise the geometrical conditions of structural details, using joints with a relatively high detail classification and low stress concentration. Optimal conditions could be reached by applying cast steel joints in combination with VHSS, resulting in joints with low stress concentration, while shifting the weld out of the most severe stress location.

ACKNOWLEDGEMENT

This research was carried out under the project number MC8.06265 in the framework of the Research Program of the Materials innovation institute M2i (www.m2i.nl), the former Netherlands Institute for Metals Research. The authors would like to thank the personnel of the Stevin Laboratory of the Delft University of Technology for the technical support and the firm Huisman Itrec for the welding of the test specimens.

REFERENCES

[1] Schröter, F., “Höherfeste Stähle für den Stahlbau – Auswahl und Anwendung”, Bauingenieur, 2003, Vol. 9, pp. 426-432.

[2] prEN 1993-1-12, “Design of Steel Structures - General - Part 1.12 : Additional Rules for the Extension of EN 1993 up to Steel Grades S700”, European Committee for Standardization, 2004.

[3] NPR-CEN/TS 13001-3-1, “Cranes – General design – Part 3.1: Limit States and Proof of Competence of Steel Structures”, European Committee for Standardization, 2004.

[4] Pijpers, R.J.M., Kolstein, M.H., Romeijn, A. and Bijlaard, F.S.K., “The Fatigue Strength of Butt Welds Made of S690 and S1100”, Proceedings of the 3rd International Conference on Steel and Composite Structures, Manchester, 2007, pp. 901-907.

[5] Pijpers, R.J.M., Kolstein, M.H., Romeijn, A. and Bijlaard, F.S.K., “The Fatigue Strength of Base Material and Butt Welds Made of S690 and S1100”, Proceedings of the 5th International Conference on Advances in Steel Structures, Singapore, 2007, Vol. III, pp. 603-608.

[6] Günther, H.P. and Kuhlmann, U., “Use and Application of High Performance Steels for Steel Structures”, IABSE Structural Engineering Documents 8, 2005.

[7] Herion, S. and Müller, C., “Untersuchung Kranspezifischer Kerbdetails”, Stahlbau, 2000, Vol. 4, No. 69, pp. 251-267.

[8] Puthli, R., Herion, S. and Bergers, J., “Untersuchungen zum Ermüdungsverhalten von hochfesten Stählen im Rahmen von LIFTHIGH”, Stahlbau, 2006, Vol. 11, No. 75, pp. 916-924.

[9] Bergers, J., Herion, S., Höhler, S., Müller, C. and Stötzel, J., “Beurteilung des Ermüdungsverhaltens von Krankonstruktionen bei Einsatz hoch- und ultrahochfester Stähle”, Stahlbau, 2006, Vol. 11, No. 75, pp. 897-915.

[10] Hamme, U, J. Hauser, A. Kern and Schriever, U., “Einsatz hochfester Baustähle im Mobilkranbau”, 2000.

[11] Kuhlmann, U., Dürr, A. and Günther, H.P., “Verbesserung der Ermüdungsfestigkeit höherfester Baustähle durch Anwendung der UIT-Nachbehandlung”, Stahlbau, 2006, Vol. 11, No. 75, pp. 930-938.

[12] EN 1993-1-9, “Design of steel structures - General - Part 1.9: Fatigue Strength of Steel Structures”, European Committee for Standardization, 2005.

[13] prEN 1090-2, “Execution of Steel Structures and Aluminium Structures - Part 2: Technical Requirements for the Execution of Steel Structures”, European Committee for Standardization, 2005.

[14] Demofonti, G., Riscuifuli, S., Sonsino, C.M., Kaufmann, H., Sedlacek, G., Müller, C., Hanus, F. and Wegmann, H.G., “High-strength Steels in Welded State for Lightweight Constructions under High and Variable Stress Peaks”, Final Report EUR 19989, Luxembourg, 2001.

[16] Gurney, T.R., “Fatigue of Welded Structures”, UK, 1979.

[17] Maddox, S.J., “Fatigue Strength of Welded Structures”, Abington Publishing, 1991

[18] Radaj, D., “Design and Analysis of Fatigue Resistant Welded Structures”, Abington Publishing, 1990.

[19] Hübner, P., “Schwingfestigkeit der hochfesten schweissbaren Baustähle StE 885 und StE 960”, Technischen Universität Bergakademie Freiberg, Germany, 1996.

[20] Wellinger, K. and Dietmann, H., “Festigkeitsberechnung”, Alfred Körner Verlag, Stuttgart, 1976.

[21] Hobbacher, A., “Recommendations for Fatigue Design of Welded Joints and Components”, IIW document XIII-1965-03 / XV-1127-03, 2004.

[22] EN-ISO 5817, Welding - Fusion-welded Joints in Steel, Nickel, Titanium and Their Alloys (Beam Welding Excluded) - Quality Levels for Imperfections, ISO Copyright Office, Switzerland, 2003.

MODIFIED ELASTIC APPROACH FOR STABILITY DESIGN OF IN-PLANE FRAME COLUMNS

Hou Hetao [1,2,3*] and Li Guoqiang [3]

[1] Associate Professor, School of Civil Engineering, Shandong University, Jinan, Shandong, China
[*](E-mail: houhetao@163.com)
[2] Postdoctor, Laiwu Steel Group Limited, Laiwu, Shandong, China
[3] Professor, School of Civil Engineering, Tongji University, Shanghai, China

Received: 16 October 2007; Revised: 25 December 2007; Accepted: 29 December 2007

ABSTRACT: In order to overcome the limitations of the current Chinese Code for Design of Steel Structures (GB50017-2003), such as the second-order analysis of the structures and the effective length method used in stability check of steel frame columns, one modified elastic approach for analysis and check for ultimate loading-carrying of steel frames is outlined and compared to the current Chinese Code method. The second-order elastic moments in a steel frame can be easily determined according to the first-order elastic analysis of the steel frame under vertical loads and lateral loads respectively. Such second-order moments are more accurate than those determined from the current Chinese Code method. By accounting for the initial geometric imperfections of the structural system and its component members directly within a second-order elastic analysis, the need for effective length or buckling solutions is eliminated, and the effective length *K*-factors can be set to be one. This paper also provides a rational means of complete frame classification that overcomes the limitations and paradoxes of the well known alignment charts for braced and unbraced frames. Simple criteria are presented that define the partially braced frames, as well as the minimum lateral bracing required by frames to achieve non-sway buckling mode. Case studies are drawn to show the detailed design procedures of the modified elastic approach. The case study covers a set of portal frames and single-bay, three-story frames. The results from the case studies are summarized to demonstrate the accuracy and validity of the approach for evaluation of the ultimate loading-carrying capacity of steel frame columns. Comparisons are made to the results from rigorous distributed plasticity of analyses. In conclusion, the modified elastic approach presented is an efficient, reliable, practical method and therefore to be recommended for general design practice.

Keywords: Steel frame column; second-order analysis; criteria of frame classification; notional lateral load; structural stability; modified elastic approach

1. INTRODUCTION

The present approach to the analysis and design of a frame structures in Chinese Code for Design of Steel Structures (GB50017-2003[1]) has to conduct essentially two separate operations, i.e. elastic analysis is conducted to determine the distribution of internal moments and forces of steel frame; inelastic analysis and design is carried out to determine the strength of each member treated as an isolated component by using the previously determined set of moments and forces. The interaction between the structural system and its members is represented by the effective length factor.

The effective length method generally provides a good method for the design of framed structures. However, the approach has major limitations. The first of these is that it does not give an accurate indication of factor against failure. The second and perhaps the most serious limitation is probably the rationale of the current two-stage process in design. There is no verification of the compatibility between the isolated member and the member as part of a frame. The effective length method is not user-friendly for a computer-based design. The other limitations of the effective length method include the difficulty of determining an effective length *K*-factor, and the inability of the method to predict the actual strength of framed member, among many others. To this end, there is an increasing awareness of the need for practical analysis/design methods that can account for the compatibility between the member and system without the use of *K*-factors (Nethercot [2], Nethercot and Gardner [3], Chen [4], Chan and Zhou [5], Liew et al. [6]).

The purpose of this paper is to present a practical design method based on the second-order elastic analysis for consideration of stability of the in-plane steel frame columns, which is expected to take the place of the effective length method.

2. SECOND-ORDER ELASTIC ANALYSIS METHOD

2.1 GB Method

In GB50017-2003(GB), the internal forces and moments may be determined using first-order elastic analysis in all cases; or second-order elastic analysis in the case of $\rho=(\sum N\times \Delta u)/(\sum H\times h)>0.1$, where ρ = non dimensional parameter, $\sum N$ = the sum of design axial forces of all columns in a story, Δu = the lateral inter-story deflection determined from the first-order elastic analysis due to design story shear $\sum H$, h = the story height. GB method does not require any consideration of initial geometric imperfections or distributed plasticity within the first-order elastic analysis, but accounts for these effects through the column strength equations. However, when performing the second-order elastic analysis, notional lateral load of H_{ni} are applied at each story level in computing the moments to account for those mentioned effects. Notional lateral load of H_{ni} is expressed as follow

$$H_{ni}=\frac{\alpha N_i}{250}\sqrt{0.2+\frac{1}{n_s}} \tag{1}$$

where N_i = the sum of column design axial forces at story i, n_s = the number of stories, α = the factor to take into account the effect of the steel strength.

For unbraced steel frames in GB method, geometrical nonlinearity is accounted for indirectly by using moment magnification factor (B_2) in lieu of a second-order elastic analysis. In using the moment magnification approach, two first-order elastic analyses are performed on the frame, as shown in Figure 1. In the first analysis, the frame is artificially prevented from sway (by providing fictitious supports at each story level) and analyzed for a given load combination with the national lateral loads of H_{ni}, the reaction forces of H_i' of the fictitious supports are obtained. In the second analysis, the frame is allowed to sway (by removing fictitious supports) and analyzed for applied reaction forces of H_i' in a reverse direction. The maximum design moments obtained for each member from these two analyses, denoted as M_{Ib} and M_{Is}, respectively, are then combined to obtain the design values for the member using the equation

$$M_{II}=M_{Ib}+B_2 M_{Is} \tag{2}$$

where the factor B_2 is given by

$$B_2=1/(1-\rho) \tag{3}$$

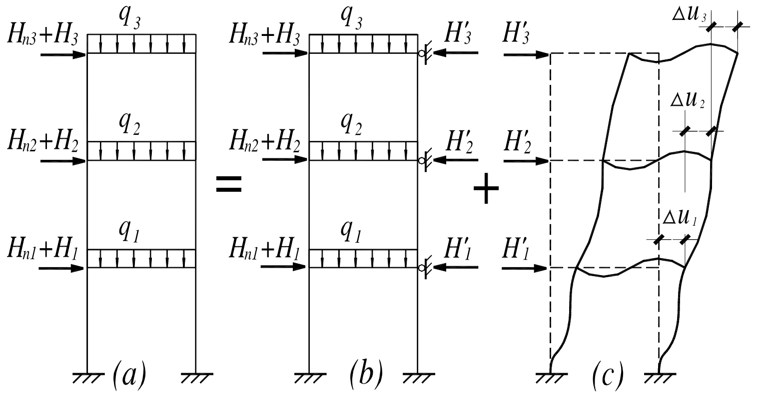

Figure 1. Approximate Second-order Elastic Analysis of Unbraced Steel Frame Using GB Method

2.2 Modified Elastic Analysis Approach

As mentioned above, one of the disadvantages of GB method is that the imperfections are not accounted for in the first-order elastic analysis, but those effects are accounted for by the use of the notional lateral load in the second-order elastic analysis. Another major disadvantage is that two different frame models (braced and unbraced frame) are utilized to calculate the approximate second-order elastic moment of the unbraced frame from Eq. 2. In order to overcome those limitations, this paper provides one modified second-order elastic analysis approach, which is made up of four parts: classification of frame; criterion of first- or second-order elastic analysis; approximate second-order elastic analysis procedure; model of the initial geometric imperfections.

Frame classification is a formalization of the engineering decision as to how the distribution of internal forces within a structure necessary for the selection of suitable members should be determined (Dario et al. [7]). Its simplest form saw all braced frames i.e. those which rely on a system of braced bays, stiff cores or shear walls to resist the applied lateral loading, classified as “non-sway” with unbraced frames (those which lateral resistance was derived from frame action within the frame itself) being either “non-sway” or “sway” depending on the extent to which second-order effects were important i.e. the extent of the differences obtained by conducting a linear or a second-order analysis(Nethercot [2]). In GB method, frames are classified into unbraced and braced cases which rely on whether there are braced bays or shear walls or not. The latter is then classified into partially-braced frame or fully braced frame. The difference between these two braced frames is that the minimum stiffness of the lateral bracing of the latter satisfies the following equation

$$S_b \geq 3(1.2\sum N_{b\,i} - \sum N_{0\,i}) \tag{4}$$

where S_b=the stiffness of the lateral bracing, $\sum N_{bi}$ and $\sum N_{0i}$ = the sum of the nominal compressive strength of all columns at story i, determined in accordance with the effective length factors of the fully braced and unbraced columns, respectively. Its difficulty is that the effective length factors of all the columns must be calculated and the design process is tedious. For the case of partially-braced frame, there is not an equation or chart to calculate the effective length factor of the column which must be used to determine the buckling load in the check for in-plane member capacity.

The LRFD Specification (1999[8]) distinguishes between columns in braced and unbraced frames. In braced frames, sidesway is inhibited by attachment to diagonal bracing or shear walls. Based upon assumptions of idealized conditions which seldom exist in real structures, the alignment chart is used to calculate the effective length factors of the braced and unbraced frame columns. However, it is very difficult to calculate the effective length factor of the partially-braced column, which must be used to determine the nominal compressive strength and the approximate second-order elastic moment.

For convenience, this paper provides an improved criterion of frame classification to check whether a frame may be regarded as braced. If the lateral bracing have a total stiffness (T, whose unit is in force/displacement) of the frame at least five times the sum of the stiffness of all the columns within the story, i.e. $T=5\sum 12i_c/L^2$(or $K_T=TL^2/i_c=60$), the frame achieves non-sway buckling mode, the frame can be defined as braced frame; otherwise, then defined as partially braced frame (Hou [9]), where L = the column length, $i_c = EI_c/L$, in which E = the modulus of elasticity, I_c = the moment of inertia, K_T = the non dimensional stiffness parameter. Following the improved criterion, the design process of frame columns therefore becomes simple and accurate. In practice, if the engineer wishes to design a steel frame, he can easily calculate the sum of the stiffness of all the columns within the story and the total stiffness of the lateral bracing, T , by hand or by performing first-order elastic analysis with computer software. According to the criterion discussed above, frame is classified as braced or partially-braced, then the effective length factor, K may be determined quickly by using the Eq. 8. Compared to GB method, major advantages of the criterion include: 1) no effective length factor calculations are required to determine the nominal compressive strength, $\sum N_{bi}$ and $\sum N_{0i}$. 2) The criterion applies in a logical and consistent way for all types of structures including steel frames, steel and composite structures.

Second-order effects shall be considered if they increase the action effects significantly or modify significantly the structural behavior. First-order elastic analysis may be used for the structure, if the increase of the relevant internal forces or moments or any other change of structural behavior caused by deformations can be neglected. In the modified second-order elastic analysis approach, the second-order elastic moments can be replaced by those obtained from the first-order elastic analysis if the following criterion is satisfied (Hou [9]):

$$\text{For } K_T \le 5,\quad \rho < 0.055 \tag{5a}$$

$$\text{For } K_T > 5,\quad \rho < 0.1 \tag{5b}$$

the terms are as defined as before.

As discussed above, GB method uses the moment magnification approach to calculate the second-order elastic moments, which is only suitable for unbraced columns and frames. One modified elastic analysis method based on GB method can be extended to partially braced frames, the second-order elastic moments, preferably determined from a second-order analysis, may be accounted for alternatively by amplifying the moments obtained from a first-order elastic analysis by the factor βB_2, under lateral loads, where β = the reduction factor to account for the effects of both the stiffness of lateral bracing and slenderness ratio of the frame column. In using the modified elastic analysis approach, two first-order elastic analyses are also performed on the frame, as shown in Figure 2. In the first analysis, the frame is analyzed under vertical loads. A second analysis is then performed with the frame subject to the real lateral loads and notional lateral loads which account for both the member out-of-straightness, δ and frame out-of-plumbness, Δ. The maximum elastic design moments obtained for each column from these two analyses, denoted as

M_{Iq} and M_{IH} , respectively, are then combined to obtain the design values for the column using the equation

$$M_{II}=M_{Iq}+\beta B_2 M_{IH} \tag{6}$$

where the reduction factor β is given by

$$\text{for } \lambda \le 60 \text{ or } \rho \le 0.32, \ \beta = 1-\eta \cdot \rho \tag{7a}$$

$$\text{for } \lambda > 60 \text{ or } \rho > 0.32, \ \beta = 1-0.25\eta \cdot \rho \tag{7b}$$

in which λ is the in-plane slenderness ratio of the column, and equals to KL/i, where K = the effective length factor obtained from Eq. 8 (Li et al. [10]), L = the column length, i = the radius of gyration; η = the reduction factor due to the lateral bracing, given by Eq. 9 (Hou [9]).
For $0 \le K_T \le 60$,

$$K=K_0/(\sqrt{1+(K_0^2/K_b^2-1)(K_T/60)^{0.5}} \tag{8}$$

$$\eta=0.1376+0.042K_T \tag{9}$$

where K_0 and K_b = effective length factors of unbraced and braced columns, respectively, which may be determined from clause 5.5.5 and Annex D of GB.

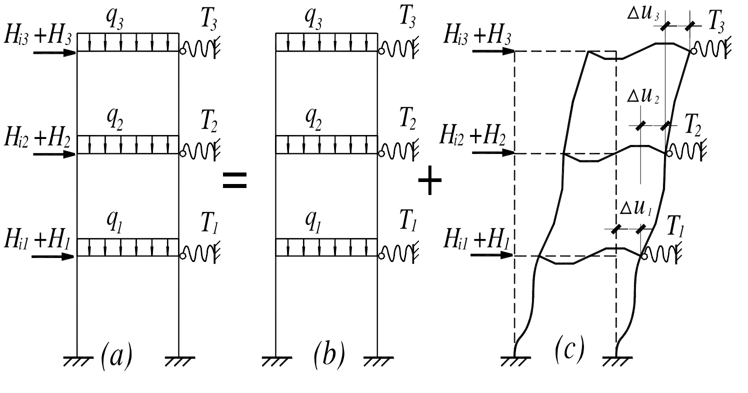

Figure 2. Approximate Second-order Elastic Analysis of
Partially Braced Steel Frame Using Modified Elastic Approach

Initial geometric imperfections in the form of member out-of-straightness, δ and frame out-of-plumbness, Δ are always present in real frameworks, which are currently assumed in many design codes are on the conservative side so that imperfection in the Perry-Robertson formula always results in a lower permissible load. The notional lateral load approach is currently used to account for the effect of frame out-of-plumbness , Δ by applying a set of notional lateral loads whose magnitudes are expressed as a friction of the gravity loads acting on the frame at each story level in the AS4100(1998[11]) , BS5950(2000[12]) and EC3(2003[13]). As mentioned above, the national lateral load approach is recommended to consider the effects of the geometric imperfections and residual stresses within the second-order elastic analysis in GB method. For the partially braced frame, those design codes do not provide the national lateral load approach to take into account of the effect of the member out-of-straightness, δ , while this effect can be accounted for implicitly in the column equations.

Referring to the Chinese Code for Construction of Steel Structure (GB50205-2001[14]), a fabrication tolerance of $\delta_0=L/1000$ for member out-of-straigtness, and $\Delta_0=h/1000$ for frame out-of-plumbness are recommended in this study, where L = the column length, h = the height of the story. This paper presents a modified notional lateral load approach to account for both δ and Δ (Hou [9]). This approach is especially suitable for calculating the elastic moments accurately in the partially braced frame. The second-order elastic analysis includes both $P-\Delta$ and $P-\delta$ effects. The modified notional lateral load applied at each story level and roof level is given by

$$H_i = \frac{N_i}{300}\sqrt{0.2+\frac{1}{n_s}} \tag{10}$$

where N_i = the sum of column design axial forces at story i, n_s= the number of stories. The modified notional lateral load is applied with all load combinations.

3. MODIFIED ELASTIC ANALYSIS AND DESIGN PROCEDURES OF FRAME COLUMNS

The present study is limited to two-dimensional steel frames, the spatial behavior of frames is not considered, and the lateral torsional buckling of members is assumed to be prevented by adequate lateral braces. The frames are subjected to static loads, not earthquake or cyclic loads. The modified elastic analysis and design approach is based on the limit-state approach to strength. Analysis and design procedures in using the modified elastic approach are summarized as follows.

(1) Calculate the dead load, live load and the load combinations based on the Load Code for the Design of Building Structures (GB50009-2001[15]), the member sizes of frames are determined from an appropriate combination of factored loads.

(2) Calculate the sum of the stiffness of all the columns within each story, $\sum 12i_c/L^2$; and the stiffness of the lateral bracing of each story, T and K_T.

(3) If K_T<60 is satisfying, the frame is defined as partially braced frame.

(4) Firstly, one first-order elastic analysis is performed on the frame to obtain the internal forces (including the design axial forces N_q and the design moments M_{Iq}) under the factored vertical loads. Secondly, another first-order elastic analysis is then performed with the frame subject to both the real and notional lateral loads to obtain the internal forces (including the design axial forces N_H and the design moments M_{IH}) and the lateral inter-story deflection, Δu. The total design axial forces of the column is the combination of the design axial forces obtained from these two first-order elastic analysis ($N=N_q+N_H$).

(5) If both the expressions $K_T \leq 5$ and $\rho>0.055$, or $K_T>5$ and $\rho>0.1$ are satisfying, the second-order elastic should be performed on the frame, the second-order moments M_{II} can be calculated using Equation 6; otherwise, the second-order elastic moments can be easily replaced by those obtained from the first-order elastic analysis ($M_{II}=M_{Iq}+M_{IH}$), since the second-order effects may be neglected.

(6) Calculate the resistance factor φ_x about x-axis for axial compressive columns according to the slenderness ratio λ_x based on K=1, the steel strength and the type of cross-section. The reduced Euler buckling load about x-axis is calculated using the equation, $N_{Ex}'=\pi^2 EA/(1.1\lambda_x)^2$, where E = the modulus of elasticity, A = the area of the cross-section.

(7) Calculate the equivalent uniform moment factor relating to in-plane x-axis bending, $\beta_{mx}=0.65+0.35M_2/M_1$, in which M_2/M_1 is the ratio of the smaller to larger moments at the ends of the column under consideration, and is taken as positive when the column is bent in single curvature, negative when bent in reverse curvature. The value may be determined in accordance with the clause 5.2.2 of GB. γ_x is the coefficient to account for the plastic distribution, defined in Table 5.2.1 of GB.

(8) The checks for ultimate loading-carrying capacity of in-plane steel frame columns are carried out, respectively.

The check for the section capacity is that

$$\frac{N}{Af}+\frac{M_x}{\gamma_x W_x f}\le 1 \tag{11}$$

The check for in-plane member capacity is

$$\frac{N}{\varphi_x Af}+\frac{\beta_{mx}M_x}{\gamma_x W_x f(1-0.8N/N'_{Ex})}\le 1 \tag{12}$$

where N = the design axial force, M_x = the design second-order elastic moment about x-axis, W_x = the section modulus of the outside fiber of the compression flange about x-axis, f = design axial steel strength.

For the case of braced frame, i.e. the $K_T\ge 60$, except the design moment $M_{II}=M_{Iq}+M_{IH}$, the other analysis and design procedures are same as those for the case of partially braced frame.

4. CASE STUDIES

A set of portal frames and two-bay, three-story frames are selected for the present case studies. The design procedures of these frames follow analysis and design guidelines described previously. The case studies are carried out by comprising the results of the proposed modified elastic approach with those of rigorous distributed plasticity of analyses and of the GB method. The stress-strain relationship for all frame members is assumed to be elastic-perfectly plastic with 235MPa yield stress (f_y) and 200000MPa elastic modulus (E). A small post-yield stiffness of $0.001E$ is used for numerical stability purposes. The maximum compressive residual stress at the flange tips is taken as $f_y/3$, shown in Figure 3.

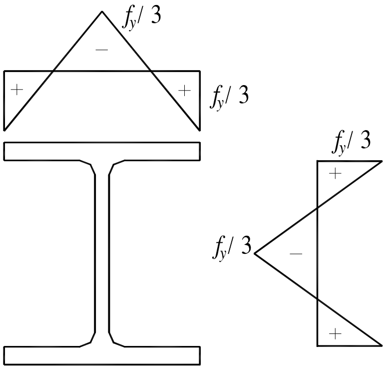

Figure 3. Residual Stress

A fabrication tolerance of $\delta_0=L/1000$ for member out-of-straightness, and $\Delta_0=h/1000$ for frame out-of-plumbness are recommended in this study. ANSYS, one of the mostly widely used and accepted commercial finite element analysis program is used in plastic zone analysis. Shell181 element is used for the analyses of frames. The residual stress distribution are modeled using the ANSYS *INITIAL STRESS* option. The initial stresses are defined as *ISFILE* using the FORTRAN user subroutine. These subroutines define the local components of the initial stress as a function of the element number by reading *ISFILE*. The pre-analysis is recommended to check the residual stress distribution. Out-of-straightness and out-of-plumbness imperfections (δ and Δ) are modeled by moving each coordinate of the nodal points.

The fixed boundary is modeled at the base of the frame columns. All frame members are bent with respect to the major axis (x-axis), and the beam-column joints are all rigid. A compact hot-rolled H-section for all frame members is assumed so that sections can develop full plastic moment capacity without local buckling. The vertical loads (including the concentrated loads and the distributed member forces) are first applied to the frame, and then the lateral loads are applied at the each floor level and roof level until the frame could not resist any more loads.

The ultimate loading-carrying capacity indicates the maximum load that the steel frame can sustain. The ultimate loads obtained from the plastic-zone analysis are applied to the frame to carry out first- or second-order elastic analysis to check the section capacity and in-plane stability of the column by using the GB method and the modified elastic approach. The errors in the checks for the section capacity and in-plane stability are calculated as Eq. 13 and Eq. 14, respectively.

$$\varepsilon_1=\frac{N}{Af}+\frac{M_x}{\gamma_x W_x f}-1 \tag{13}$$

$$\varepsilon_2=\frac{N}{\varphi_x Af}+\frac{\beta_{mx}M_x}{\gamma_x W_x f(1-0.8N/N'_{Ex})}-1 \tag{14}$$

Unconservative error is represented by a negative value ($\varepsilon_1< 0$ or $\varepsilon_2<0$), and conservative error by a positive value; as ε_1 or ε_2 equals to zero, the result of check of the member capacity represents the real ultimate loading-carrying capacity of the frame.

4.1 Single-bay Portal Frame

4.1.1 Single-bay unbraced portal frame

Figure 4 shows the unbraced portal frame subjected to a non-proportional loading. The members are HN400×200×8×13(A=8412mm^2, i_x=168mm, I_x=2.37×10^{8}mm^4, W_x=1.19×10^{6}mm^3) for the beam and HW200×200×8×12 (A=6428mm^2, i_x=86.1mm, I_x=4.77×10^{7}mm^4, W_x=4.77×10^{5}mm^3) for the columns. Factored distributed beam force of q=59.4kN/m, and concentrated gravity loads of P_l=287kN are applied to the portal frame. The stiffness of lateral bracing at the top of the column is assumed to be zero, i.e. K_T=0. The ultimate load-carrying capacity H_u of the frame is calculated to be 68.57kN using the plastic zone analysis.

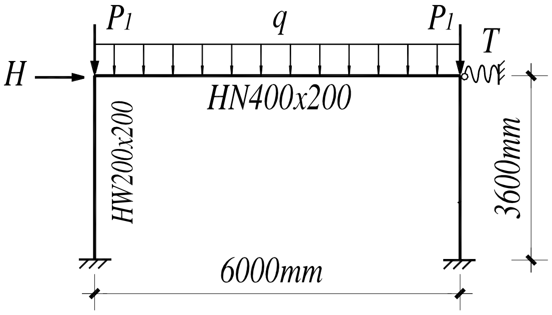

Figure 4. Configuration of Portal Frame

The unbraced portal frame is subjected to the combined action of gravity loads (q and P_l) and lateral load (H_u). The GB method is based on first- or second-order elastic analysis of the perfect structure (i.e. no notional lateral loads or modeled imperfections are included). For the modified elastic approach, notional lateral load of H_i (Eq. 10) is applied in the load combination of gravity loads and lateral load. The unbraced portal frame is analyzed by a rigorous second-order analysis to determine an accurate distribution of the moments. These moments of the right column are used for comparison to those established by the GB method and the modified elastic approach. The results of analysis and comparison are summarized in Table 1.

Table 1. Elastic Moments of Rigorous Analysis,
GB and Modified Elastic Approach for Unbraced Portal Frame

	(a) rigorous analysis	(b) GB method	(b)/(a)	(c) modified elastic approach	(c)/(a)
M (kN.m)	125.92	132.45	1.05	130.71	1.03

Table 1 indicates that the result of the GB method is approximately 5% conservative compared to the rigorous second-order analysis results. Whereas the analysis result of the modified elastic approach is only 3% conservative compared to that of the rigorous analysis. The moment of GB method larger than that of the modified elastic approach is due to the use of larger notional lateral load (Eq. 1) in GB method. The two methods are accurate to somewhat conservative for case of unbraced frame (i.e. K_T=0).

The errors in the checks for ultimate loading-carrying capacity of in-plane steel frame column determined from Eq. 13 and Eq. 14 by using the GB method and the modified elastic approach are provided in Table 2. Table 2 shows that the error ε_2 determined by the GB method is more conservative than ε_1, so the in-plane stability capacity governs the ultimate loading-carrying capacity of the frame. Conversely, the section capacity in the modified elastic approach controls the ultimate loading-carrying capacity of the frame. In addition, the error ε_2 in GB method is more conservative than ε_1 in the modified elastic approach because the second-order effects and the initial geometric imperfections are accounted for by both the global analysis and individual stability check of member in GB method. The modified elastic approach gives a more liberal accurate estimate of ultimate loading-carrying capacity of in-plane steel frame column. It can be observed that in the modified elastic approach the section capacity check is needed and the in-plane stability check is not required. The conservative error of the section capacity check in the modified elastic approach is attributed to the fact that the modified elastic approach does not consider the inelastic moment redistribution but the plastic zone analysis includes inelastic redistribution effect.

Table 2. Errors of Member Check by Using GB Method and Modified Elastic Approach for Unbraced Portal Frame

	GB method	modified elastic approach
ε_1(section capacity)	55.98%	57.06%
ε_2 (in-plane member capacity)	69.95%	-3.90%

4.1.2 Single-bay partially braced portal frame

Figure 4 shows the partially braced portal frame subjected to a non-proportional loading. The members and loads applied are all same as those of the unbraced portal frame. The stiffness of lateral bracing at the top of the column is assumed to be the sum of the stiffness of the columns within the story, i.e. $T=\sum 12i_c/L^2$ (or $K_T=12$). The ultimate load-carrying capacity H_u of the frame is calculated to be 131.08kN using the plastic zone analysis.

The partially braced portal frame under the combination of gravity loads (q and P_1) and lateral load (H_u) is also analyzed by a rigorous second-order analysis to determine an accurate distribution of the moments. These moments of the right column are used for comparison to those established by the GB method and the modified elastic approach. The results of analysis and comparison are summarized in Table 3.

Table 3. Elastic Moments of Rigorous Analysis, GB and Modified Elastic Approach for Partially Braced Portal Frame

	(a) rigorous analysis	(b) GB method	(b)/(a)	(c) modified elastic approach	(c)/(a)
M (kN.m)	116.98	115.7	0.989	117.23	1.002

Table 3 indicates that the result of the GB method is approximately 1.01% unconservative compared to the rigorous second-order analysis results. This difference is attributed to the fact that the GB method does not consider the second-order effects and the initial geometric imperfections (δ and Δ). Whereas the analysis result of the modified elastic approach is only 0.2% conservative compared to that of the rigorous analysis since this approach accounts for the second-order effects and the initial geometric imperfections (δ and Δ) when performing the elastic analysis on the steel frame.

The errors in the checks for ultimate loading-carrying capacity of in-plane steel frame column determined from Eq. 13 and Eq. 14 by using the GB method and the modified elastic approach are provided in Table 4. Table 4 shows that the error ε_2 determined by the GB method is also more conservative than ε_1, so the in-plane stability capacity governs the ultimate loading-carrying capacity of the frame. Conversely, the section capacity in the modified elastic approach controls the ultimate loading-carrying capacity of the frame. In addition, the error ε_2 in GB method is more conservative than ε_1 in the modified elastic approach. The modified elastic approach gives a more liberal accurate estimate of ultimate loading-carrying capacity of in-plane steel frame column. It can be observed that in the modified elastic approach the section capacity check is needed and the in-plane stability check is not required. The conservative error of the section capacity check in the modified elastic approach is attributed to the fact that the modified elastic approach does not consider the inelastic moment redistribution but the plastic zone analysis includes inelastic redistribution effect.

Table 4. Errors of Member Check by Using
GB Method and Modified Elastic Approach for Partially Braced Portal Frame

	GB method	modified elastic approach
ε_1(section capacity)	47.52%	48.03%
ε_2 (in-plane member capacity)	56.20%	-6.47%

4.1.3 Single-bay braced portal frame

Figure 4 shows the braced portal frame subjected to a non-proportional loading. The members are same as those of the unbraced portal frame. Factored distributed beam force of q=59.4kN/m are applied to the braced portal frame. The stiffness of lateral bracing at the top of the column is assumed to be five times the sum of the stiffness of the columns within the story, i.e. $T=\sum 60i_c/L^2$ (or K_T=60). According to the criteria of frame classification discussed above, this frame can be defined braced frame which achieves non-sway buckling mode. The ultimate load-carrying capacity P_u of the frame is calculated to be 981.60kN using the plastic zone analysis.

The braced portal frame is subjected to the gravity loads (q and P_u) while using the GB method based on first-order elastic analysis of the perfect structure. For the modified elastic approach, notional lateral load of H_i (Eq. 10) is applied in the load combination of gravity loads. The braced portal frame is also analyzed by a rigorous second-order analysis to determine an accurate distribution of the moments. These moments of the right column are used for comparison to those established by the GB method and the modified elastic approach. The results of analysis and comparison are summarized in Table 5.

Table 5. Elastic Moments of Rigorous Analysis,
GB and Modified Elastic Approach for Braced Portal Frame

	(a) rigorous analysis	(b) GB method	(b)/(a)	(c) modified elastic approach	(c)/(a)
M (kN.m)	80.45	80.32	0.998	80.35	0.999

Table 5 indicates that the results of the GB method and the modified elastic approach are approximately same and agree well with the rigorous second-order analysis result. These results may be attributed to the fact that the effects of second-order and the initial geometric imperfections (δ and Δ) can be neglected in this case.

The errors in the checks for ultimate loading-carrying capacity of in-plane steel frame column determined from Eq. 13 and Eq. 14 by using the GB method and the modified elastic approach are provided in Table 6. Table 6 shows that the section capacity governs the ultimate loading-carrying capacity of the frame in the GB method and the modified elastic approach. In addition, the error of the check for section capacity in GB method is approximately same as that in the modified elastic approach. The conservative error of the section capacity check in the modified elastic approach and GB method is attributed to the fact that the modified elastic approach does not consider the inelastic moment redistribution but the plastic zone analysis includes inelastic redistribution effect.

Table 6. Errors of Member Check by Using
GB Method and Modified Elastic Approach for Braced Portal Frame

	GB method	modified elastic approach
ε_1(section capacity)	67.18%	67.2%
ε_2 (in-plane member capacity)	48.33%	64.07%

4.2 Three-story Frame

4.2.1 Three-story unbraced frame

A two-bay, three-story unbraced frame is selected to demonstrate the accuracy and validity of the modified elastic approach for evaluation of the loading-carrying capacity of steel frame columns. The configuration of the frame is shown in Figure 5.

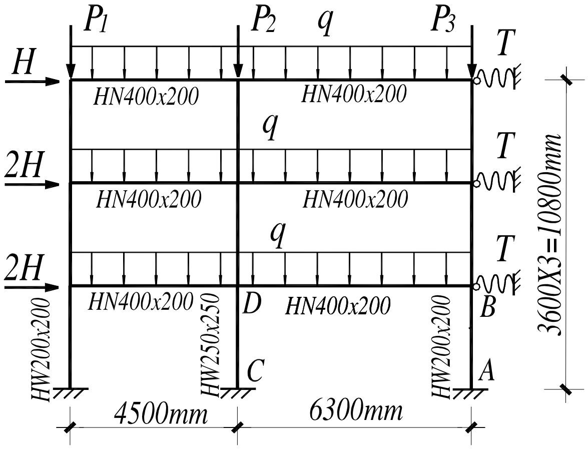

Figure 5. Configuration of Three-story Frame

The members are HN400x200x8x13 for the beams and HW200×200 ×8×12 for the exterior columns, HW250×250×9×14 (A=9218mm^2, i_x=108mm, I_x=1.08×10^{8}mm^4, W_x=8.67×10^{5}mm^3) for the interior columns. The beams are subjected to factored distributed member forces of q=70.3kN/m, and the concentrated gravity loads of P_1=158.18kN, P_2=379.62kN, P_3=221.45kN are simultaneously applied to the top of the columns of the frame, respectively. The stiffness of lateral bracing at each floor level is assumed to be zero, i.e. K_T=0. The ultimate load-carrying capacity H_u of the frame is calculated to be 23.84kN using the plastic zone analysis.

The elastic analysis results of the right exterior column AB of the three-story frame using the rigorous second-order analysis, the GB method and the modified elastic approach are presented in Table 7. Similar to the unbraced portal frame, the analysis result of the modified elastic approach is 5.7% conservative compared that of the rigorous analysis, but 7.7% conservative in the GB method. This difference between these two methods is due to the larger notional lateral loads applied to the frame to account for both residual stresses and the initial geometric imperfections (δ and Δ) in GB method.

Table 7. Elastic Moments of Rigorous Analysis,
GB and Modified Elastic Approach for Three-story Unbraced Frame.

	(a) rigorous analysis	(b) GB method	(b)/(a)	(c) modified elastic approach	(c)/(a)
M (kN.m)	82.96	89.32	1.077	87.63	1.057

Table 8 presents the errors in the checks for ultimate loading-carrying capacity of in-plane steel frame column determined from Eq. 13 and Eq. 14 by using the GB method and the modified elastic approach. Table 8 shows that the GB method is also controlled by the check for the member section capacity of the three-story frame; and the modified elastic approach does not rely on effective length factors to assess the in-plane capacity, its design check is based on the member section capacity. The error ε_1 in the GB method is more conservative than ε_1 in the modified elastic approach. Consequently, the section capacity check in GB method and the modified elastic approach is needed only. However, the modified elastic approach provides the more accurate prediction of the ultimate loading-carrying capacity of steel frame, and also produces an economical design than the GB method. The smaller conservative errors compared to those of portal frame are observed here, which may be due to the larger axial load applied on the column and stories of frame. The conservative error of the section capacity check of the two methods is attributed to the fact that the two methods do not consider the inelastic moment redistribution but the plastic zone analysis includes inelastic redistribution effect.

Table 8. Errors of Member Check by Using
GB Method and Modified Elastic Approach for Three-story Unbraced Frame

	GB method	modified elastic approach
ε_1(section capacity)	35.55%	26.36%
ε_2 (in-plane member capacity)	-13.80%	-15.57%

4.2.2 Three-story partially braced frame

A two-bay, three-story partially braced frame is selected to demonstrate the accuracy and validity of the modified elastic approach for evaluation of the loading-carrying capacity of steel frame columns. The configuration of the frame is also shown in Figure 5.

The members and loads applied are all same as those of the unbraced three-story frame. The stiffness of lateral bracing at each floor level is assumed to be the sum of the stiffness of the columns within the story, i.e. $T=\sum 12i_c/L^2$ (or $K_T=12$). The ultimate load-carrying capacity H_u of the frame is calculated to be 142.86kN using the plastic zone analysis.

The elastic analysis results of the right exterior column *AB* of the three-story frame using the rigorous second-order analysis, the GB method and the modified elastic approach are presented in Table 9. Similar to the portal frame, the analysis result of the modified elastic approach is only 1.6% conservative compared to that of the rigorous analysis, but the unconservtive error in the GB method is up to 5.5% due to ignoring the geometric nonlinearity and the initial geometric imperfections (δ and Δ).

Table 9. Elastic Moments of Rigorous Analysis,
GB and Modified Elastic Approach for Three-story Partially Braced Frame.

	(a) rigorous analysis	(b) GB method	(b)/(a)	(c) modified elastic approach	(c)/(a)
M (kN.m)	86.93	82.2	0.945	88.32	1.016

Table 10 presents the errors in the checks for ultimate loading-carrying capacity of in-plane steel frame column determined from Eq. 13 and Eq. 14 by using the GB method and the modified elastic approach. As previously discussed about the partially braced portal frame, Table 10 shows that the GB method is also controlled by the check for the in-plane capacity of the three-story frame; and the modified elastic approach does not rely on effective length factors to assess the in-plane capacity, its design check is based on the member section capacity. The error ε_2 in the GB method is more conservative than ε_1 in the modified elastic approach. The conservative error ε_1 in the modified elastic approach is attributed to the fact that the modified elastic approach does not consider the inelastic moment redistribution but the plastic zone analysis includes inelastic redistribution effect. In conclusion, the section capacity check in the modified elastic approach is needed only. The modified elastic approach provides the more accurate prediction of the ultimate loading-carrying capacity of steel frame, and also produces an economical design than the GB method.

Table 10. Errors of Member Check by Using
GB Method and Modified Elastic Approach for Three-story Partially Braced Frame

	GB method	modified elastic approach
ε_1(section capacity)	25.89%	30.71%
ε_2 (in-plane member capacity)	34.48%	-20.50%

4.2.3 Three-story braced frame

Figure 5 shows the braced three-story frame subjected to a non-proportional loading. The members of the frame are same as those of the unbraced frame. The beams are subjected to factored distributed member forces of q=85kN/m. The stiffness of lateral bracing at each floor level is assumed to be five times the sum of the stiffness of the columns within the story, i.e. $T=\sum 60 i_c/L^2$ (or K_T=60). The ultimate load-carrying capacity $P_{1u}=4.5nq/2$=207.70kN, $P_{2u}=5.4nq$=498.47kN, $P_{3u}=6.3nq/2$=290.78kN are obtained by using the plastic zone analysis, which are simultaneously applied to the top of the columns of the frame, respectively.

The elastic analysis results of the right exterior column *AB* of the three-story frame using the rigorous second-order analysis, the GB method and the modified elastic approach are presented in Table 11. Similar to the braced portal frame, the analysis results of the GB method and the modified elastic approach are approximately same and agree well with the rigorous second-order analysis result. These results may be attributed to the fact that the effects of second-order and the initial geometric imperfections (δ and Δ) can be neglected in this case.

Table 11. Elastic Moments of Rigorous Analysis,
GB and Modified Elastic Approach for Three-story Braced Frame.

	(a) rigorous analysis	(b) GB method	(b)/(a)	(c) modified elastic approach	(c)/(a)
M (kN.m)	48.30	48.11	0.996	48.12	0.996

Table 12 presents the errors in the checks for ultimate loading-carrying capacity of in-plane steel frame column determined from Eq. 13 and Eq. 14 by using the GB method and the modified elastic approach. As previously discussed about the braced portal frame, the comparison of the results also shows that the section capacity controls the ultimate loading-carrying capacity of the braced frame in both the GB method and the modified elastic approach. In addition, the error of the check for section capacity in GB method is approximately same as that in the modified elastic approach. The conservative error of the section capacity check in the modified elastic approach and GB method is attributed to the fact that the modified elastic approach does not consider the inelastic moment redistribution but the plastic zone analysis includes inelastic redistribution effect.

Table 12. Errors of Member Check by Using
GB Method and Modified Elastic Approach for Three-story Braced Frame

	GB method	modified elastic approach
ε_1(section capacity)	23.57%	23.58%
ε_2 (in-plane member capacity)	3.86%	18.50%

5. CONCLUSIONS

A modified second-order elastic approach has been developed for analysis and check for ultimate loading-carrying of steel frames. The conclusions of this study may be summarized as follows.

(1) Compared to GB method, the modified elastic approach provides an improved criterion of frame classification.
(2) By using the modified elastic approach, the second-order elastic moments in a steel frame can be easily determined according to the first-order elastic analysis of the steel frame under vertical loads and lateral loads respectively. The case studies shows that such second-order elastic moments are more accurate than those determined from the GB method.
(3) The case studies show that the section capacity in the modified elastic approach controls the ultimate loading-carrying capacity of the frame, whereas the in-plane stability capacity in the GB method governs the ultimate loading-carrying capacity of the frame. The check errors of the section capacity in the modified elastic approach are less than that of the in-plane stability capacity in the GB method, as a result, the modified elastic approach captures well the ultimate load-carrying capacity of the steel frame including its individual members.
(4) The modified elastic approach is time-effective in design process because it completely eliminates tedious and often confused member capacity checks including the calculation of *K*-factors in the GB method.
(5) The modified elastic approach presented is an efficient, reliable, practical method and therefore to be recommended for general design practice.

ACKNOWLEDGEMEMT

The work in this paper was supported by the Ph.D. Fund of Shandong Province (Grant No. 2006BS10004).

REFERENCES

[1] GB50017-2003, “Code for Design of Steel Structures, Ministry of Construction”, China, 2003.
[2] Nethercot, D.A., “Frame Structures: Global Performance, Static and Stability Behavior General Report”, Journal of Constructional Steel Research, 2000, Vol. 55, pp.109-124.
[3] Nethercot, D.A. and Gardner, L., “The EC3 Approach to the Design of Columns, Beams and Beam-columns”, Steel and Composite Structures, 2005, Vol.5, No. 2-3, pp. 127-140.
[4] Chen, W.F., “Structural Stability : From Theory to Practice”, Engineering Structures, 2000, Vol. 22, pp. 116-122.
[5] Chan, S.L. and Zhou, Z.H., “Non-linear Integrated Design and Analysis of Skeletal Structures by 1 Element per Member”, Engineering Structures, 2000, Vol. 22, pp. 246-257.
[6] Liew, J.Y.R., Chen, W.F. and Chen, H., “Advanced Inelastic Analysis of Frame Structures”, Journal of Constructional Steel Research, 2000, Vol. 55, pp. 245-265.
[7] Dario, J. and Aristizabal-Ochoa, “Braced, Partially Braced and Unbraced Columns: Complete Set of Classical Stability Equations”, Structural Engineering and Mechanics, 1996, Vol. 4, No. 4, pp. 365-381.
[8] AISC, “Load and Resistance Factor Design Specification for Structural Steel Buildings”, American Institute of Steel Construction, Chicago, IL, 1999.
[9] Hou, H.T., “The Research on Check Method for Limit State Strengths of Steel Frame Columns”, Ph.D. Thesis, Tongji University, China, 2005.

[10] Li, G.Q., Liu, Y.S. and Zhao, X., “Advanced Analysis and Design of Reliability of the Steel Structure Frame”, Beijing, Press of Chinese Building Industry, China, 2006.
[11] AS-4100, “Australia Standard for Steel Structures”, Sydney, 1998.
[12] BS5950, “Structural Use of Steel in Building, Part 1”, British Standards Institution, U.K, 2000.
[13] CEN. prEN 1993-1-1:2003 Eurocode 3: “Design of Steel Structures, Part 1-1: General Rules and Rules for Buildings”, European Committee for Standardization, Brussels, 2003.
[14] GB50205-2001, “Code for Construction of Steel Structure”, Ministry of Construction, China, 2001.
[15] GB50009-2001, “Load Code for the Design of Building Structures”, Ministry of Construction, China, 2001.

Advanced Steel Construction Vol. 5, No. 1, pp. 49-71 (2009)

DIRECT STRENGTH PREDICTION OF LIPPED CHANNEL COLUMNS EXPERIENCING LOCAL-PLATE/DISTORTIONAL INTERACTION

N. Silvestre, D. Camotim* and P.B. Dinis

Department of Civil Engineering and Architecture, ICIST/IST, Technical University of Lisbon, Portugal
**(Corresponding author: E-mail: dcamotim@civil.ist.utl.pt)*

Received: 9 November 2007; Revised: 3 January 2008; Accepted: 7 January 2008

ABSTRACT: This paper reports an ongoing investigation intended to assess the performance of the Direct Strength Method (DSM) to estimate the ultimate strength of lipped channel columns affected by local-plate/distortional mode interaction. First, the DSM approaches to safety check columns against local-plate and distortional failures are briefly reviewed, with special attention devoted to a recently proposed extension that takes into account the above buckling mode interaction. Next, one presents and discusses the results of a parametric study, carried out by means of the code ABAQUS and involving the evaluation of the "exact" ultimate loads of *63* lipped channel columns with various geometries, all exhibiting local-plate/distortional interaction. Then, these ultimate strength data are compared with the estimates provided by the available DSM formulae and, on the basis of this comparison, one identifies several features that a DSM approach successfully accounting for local-plate/distortional interaction must incorporate.

Keywords: Direct Strength Method (DSM), cold-formed steel, lipped channel columns, strength, local-plate buckling, distortional buckling, local-plate/distortional interaction

---

1. INTRODUCTION

The Direct Strength Method (DSM) was originally proposed by Schafer and Peköz [1], about nine years ago, and has been continuously improved since, mainly due to the research activity carried out by Schafer [2, 3]. Moreover, one should mention that the inclusion of the DSM in the AS/NZS and NAS specifications for cold-formed steel design has been very recently approved – they already appear in the current (new) versions of these codes [4, 5]. The method has been shown to provide an efficient general approach to estimate the ultimate strength of cold-formed steel columns and beams (i) exhibiting global (flexural, torsional or flexural-torsional), distortional or local-plate failure modes or (ii) failing in mechanisms that involve interaction between global and local-plate buckling modes. Indeed, the most recent DSM version stipulates the need to perform two independent safety checks, regardless of the member critical buckling mode nature: (i) one against a distortional failure and (ii) the other against a local-plate or a combined local-plate/global collapse. In the latter case, the DSM provides an efficient alternative to the more traditional and conservative "effective width method". However, as pointed out by Schafer [2, 3, 6, 7], further research is needed before the DSM approach can be successfully applied to members (i) under compression and bending [8, 9] or (ii) influenced by interaction phenomena involving distortional buckling modes [10-13]. Since it has been recently shown that the post-buckling and ultimate strength behaviours of various commonly used lipped channel cross-section shapes can be strongly affected by coupling between local-plate and distortional buckling modes [14-16], it would be obviously very convenient to have this mode interaction phenomenon also covered by the DSM.

The objective of this work is to contribute towards the extension of the domain of application of the available DSM, by making it able to estimate the ultimate strength of lipped channel columns affected by interaction involving local-plate and distortional buckling modes. In order to achieve this goal, one begins by presenting the main results of a shell finite element investigation (performed with the code ABAQUS [17]) concerning the elastic-plastic post-buckling behaviour (up to collapse) of lipped channel columns experiencing local-plate/distortional buckling mode interaction. Then, one reports an extensive parametric study involving the determination of the elastic-plastic failure loads of lipped channel columns with distinct cross-section dimensions, lengths and yield stresses, and containing critical-mode (distortional) small-amplitude initial geometrical imperfections – the columns were carefully selected, in order to exhibit strong local-plate/distortional interaction effects. All second-order elastic-plastic analyses were performed in the finite element code ABAQUS and discretising the columns into 4-node shell elements. These ultimate strength values then provide a "data bank" that makes it possible to propose and validate preliminary recommendations concerning the use of a DSM approach to estimate collapse loads of columns affected by local-plate/distortional mode interaction – as already mentioned, the results reported here deal with an ongoing investigation aimed at proposing (slight) modifications to the existing DSM equations, thus making them applicable to the design of lipped channel columns against this mode interaction phenomenon.

2. LOCAL-PLATE/DISTORTIONAL BUCKLING MODE INTERACTION

One reports here the main results of a recent investigation on the elastic-plastic post-buckling behaviour and ultimate strength of simply supported (plain) lipped-channel columns that are strongly affected by local-plate/distortional buckling mode interaction – the columns analysed (i) have the cross-section dimensions, length and elastic constants indicated in Figure. 1(a) and (ii) buckle elastically for $\sigma_{cr}=100.5\ MPa$ in arbitrary combinations of (ii_1) a *3* half-wave local-plate mode and (ii_2) a single half-wave distortional mode, as illustrated in Figure. 1(b) [16]. The ultimate strengths were obtained through *finite element* analyses (FEA) carried out in the code ABAQUS [17] and adopting *shell* elements to discretise the columns. As far as the performance of these FEA is concerned, the following aspects deserve to be mentioned here [14, 18]:

(i) Discretisation. The column mid-surfaces were discretised into S4 finite elements (ABAQUS nomenclature: isoparametric 4-node shell elements with the shear stiffness yielded by a *full* integration rule), which were found to be the most adequate to carry out this task. One considered *20-30* elements along the cross-section mid-line (width of about *10 mm*) and previous convergence/accuracy studies showed that the finite element length-to-width ratio should be comprised between *1* and *2*.

(ii) Support Conditions. All columns have end sections locally/globally pinned and free to warp. Concerning the first aspect, these support conditions were modelled by imposing null transverse membrane and flexural displacements at all end section nodes – in order to preclude a spurious longitudinal rigid-body motion, the axial displacement was prevented at one mid-span cross-section node.

(iii) Loading. Compressive forces, statically equivalent to a uniform normal stress distribution, are applied at the nodes of the column end-sections. Since the reference value of the *load parameter p* is *t N/mm* (*t* is the wall thickness), which corresponds to a *1 MPa* uniform stress distribution, the value of *p* yielded by ABAQUS is numerically equal to the *average stress* acting on the column (expressed in *MPa*).

(iv) Material Modelling. The column (carbon steel) material behaviour, deemed isotropic and homogeneous, was modelled through (iv_1) linear elastic (bifurcation analysis) and (ii) elastic/perfectly-plastic (post-buckling analysis) stress-strain laws. In the latter case, the well-known Prandtl-Reuss model (J_2-flow theory), which combines Von Mises's yield criterion with the associated flow rule, was adopted. These stress-strain laws are readily available in the ABAQUS material behaviour library and one just needs to provide the values of E, ν and f_y – one considered $E=210\ GPa$ (Young's modulus), $\nu=0.3$ (Poisson's ratio) and five different yield stresses, which correspond to yield-to-critical stress ratios equal to $f_y/\sigma_{cr}\approx 1.2$, 2, 3.5, 5.5 (in elastic columns, included here for the sake of completeness, one obviously considered $f_y/\sigma_{cr}=\infty$).

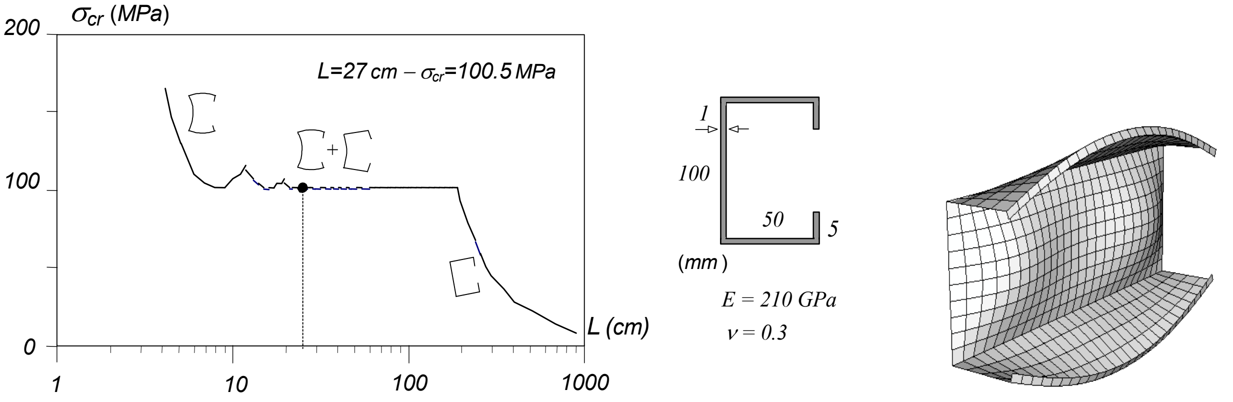

(a) (b)

Figure 1. Buckling Results: (a) σ_{cr} *vs.* L Curves (b) Critical "Combined" LP/D Mode Shape

2.1 Initial Geometrical Imperfections

The shape of the initial geometrical imperfections plays a crucial role in mode interaction investigations, since its choice may alter considerably the post-buckling behaviour and ultimate strength of the structural system under consideration. Indeed, the usual approach of including critical-mode imperfections ceases to be well defined, due to the presence of two "competing" buckling modes that may be combined arbitrarily – in this case, a three half -wave local-plate and a single half-wave distortional buckling modes. Thus, in order to obtain column equilibrium paths that (i) cover the whole imperfection shape range and (ii) can be compared in a meaningfully way, the following approach was adopted:

(i) To determine "pure" critical buckling modes with unit mid-span (i_1) mid-web flexural displacement (local-plate – $w_{LP}=1$) and (i_2) flange-lip corner vertical displacement (distortional – $v_D=1$)[1] – these two modes were obtained through preliminary linear stability analyses, based on a finite element mesh *identical* to the one adopted in the post-buckling analyses. Then, a given "combined" (critical) imperfection is obtained as a linear combination of the pure modes, with coefficients $w_{LP.0}$ and $v_{D.0}$. Note that, in general, both buckling modes will contribute to w_0 and v_0, *i.e.*, one has

$$w_0 = w_{D.0} + w_{LP.0} \qquad v_0 = v_{D.0} + v_{LP.0} \tag{1}$$

where $w_{D.0}$, $w_{LP.0}$, $v_{D.0}$ and $v_{LP.0}$ quantify the aforementioned contributions.

(ii) All initial imperfections share the same overall magnitude, equal to *10%* of the wall thickness t. In order to achieve this, one begins by normalising the pure modes in such a way that $w_{LP.0}=0.1\,t$ and $v_{D.0}=0.1\,t$ (in this particular case, $0.1\,t=0.1\,mm$). Then, one ensures the above combined amplitude by simply enforcing the condition

$$(v_{D.0})^2 + (w_{LP.0})^2 = 0.1^2 \tag{2}$$

---

[1] In order to be able to "separate" the local-plate and distortional modes, it was necessary to perform buckling FEA in columns with slightly altered wall thickness values.

(iii) A better visualisation and “feel” of the initial imperfection shape can be obtained by looking at the *0.1 mm* radius circle drawn in the $w_{LP.0}$-$v_{D.0}$ plane and shown in Figure. 2(a): each “acceptable” imperfection shape lies on this circle and corresponds to an angle θ, measured counter clockwise from the horizontal ($v_{D.0}$) axis and defining the ratio $v_{D.0}$ / $w_{LP.0}$ ($v_{D.0}=0.1\cos\theta$ and $w_{LP.0}=0.1\sin\theta$). Figure. 2(b) shows the FEM-based initial imperfections associated with $\theta=0, 180^o$ and $\theta=90, 270^o$ – pure distortional and pure local-plate. Finally, note that (iii$_1$) $\theta=0^o$ and $\theta=180^o$ correspond to *inward* and *outward* flange-lip motions and (iii$_2$) $\theta=90^o$ and $\theta=270^o$ to *outward* and *inward* mid-span web bending.

(iv) In this work, initial imperfections associated with angles multiple of 15^o were considered – *i.e.*, the *14* imperfection shapes defined by $\theta=0$, *30*, *45*, *60*, *90*, *120*, *150*, *180*, *210*, *240*, *270*, *300*, *315*, *330°*.

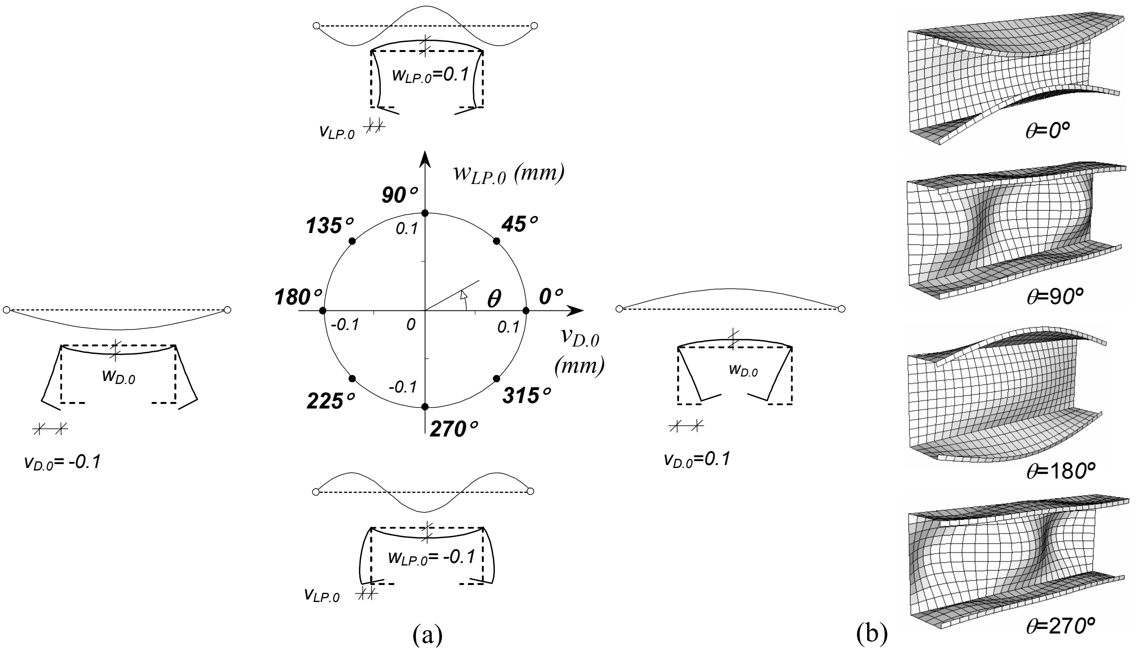

(a) (b)

Figure 2. (a) Initial Geometrical Imperfection Representation in the $w_{LP.0}-v_{D.0}$ Plane and (b) Four FEM-Based Imperfection Shapes ($\theta=0$, *90*, *180*, *270°*)

2.2 Post-Buckling Equilibrium Paths

One addresses now the influence of the local-plate/distortional mode interaction in the elastic-plastic post-buckling behaviour of lipped channel columns (i) containing the *14* initial imperfection shapes defined above (all with the same overall amplitude) and (ii) exhibiting the *5* yield-to-critical stress ratios f_y/σ_{cr} given earlier (recall that one has $\sigma_{cr.LP}=\sigma_{cr.D}=100.5\ MPa$, which corresponds to $P_{cr}=21.1\ kN$). Figures. 3(a)-(b) show the upper portions ($P/P_{cr}>0.8$) of the elastic and elastic-plastic equilibrium paths P/P_{cr} *vs.* v/t describing the post-buckling behaviours of columns with (i) initial imperfections defined by $0\leq\theta\leq180^o$ (Figure. 3(a)) and $180\leq\theta\leq360^o$ (Figure. 3(b)), and (ii) yield-to-critical stress ratios $f_y/\sigma_{cr}\approx2$, *3.5*, *5.5*. On the other hand, Figures. 4(a)-(b) show the upper portions ($P/P_{cr}>0.7$) of similar equilibrium paths of columns with the lowest stress ratio ($f_y/\sigma_{cr}\approx1.2$). Finally, Figures. 5(a)-(b) provide information about the evolution of the plastic strains in the two columns defined by $\theta=0^o+f_y/\sigma_{cr}\approx3.5$ and $\theta=90^o+f_y/\sigma_{cr}\approx3.5$ – in each case, one presents *4* plastic strain diagrams, corresponding to different equilibrium states located along the post-buckling equilibrium path (their locations are indicated in Figure. 5(a)). It is worth noting that (i) the deformed configurations corresponding to the points **1** are amplified *10* times with respect to the remaining ones and that (ii) the points **4** always correspond to equilibrium states immediately after the column collapse – *i.e.*, the associated deformed configurations provide information about the column *failure modes*.

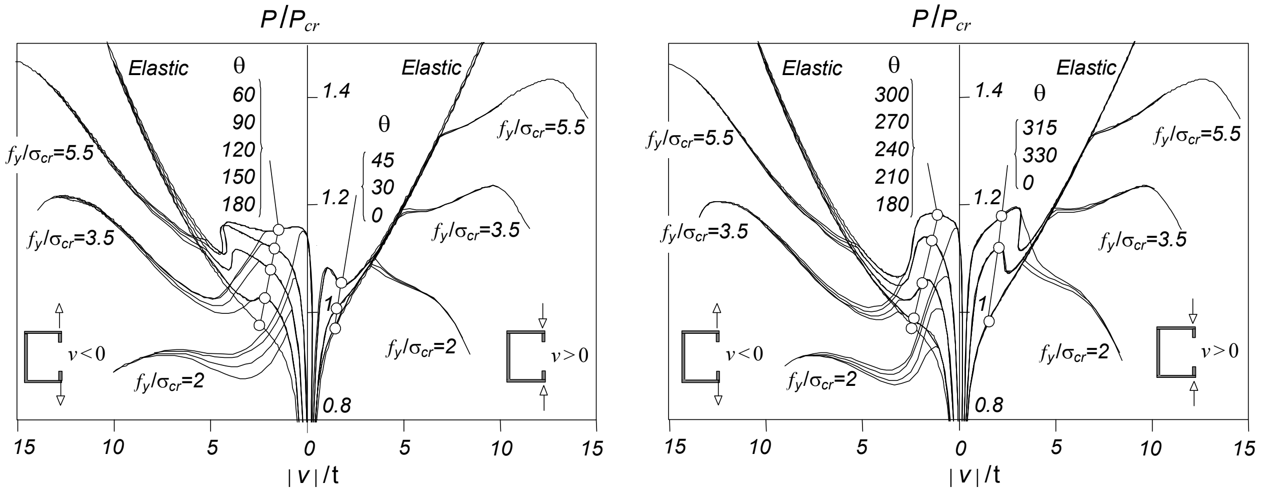

(a) (b)

Figure 3. Column Elastic and Elastic-Plastic ($f_y/\sigma_{cr}\approx 2,\ 3.5,\ 5.5$) Post-Buckling Equilibrium Paths P/P_{cr} *vs.* v/t: (a) $0^o\leq\theta\leq 180^o$ and (b) $180^o\leq\theta\leq 360^o$

The observation of the post-buckling results presented in Figures. 3 to 5 prompts the following remarks:

(i) Even under local-plate/distortional (LP/D) mode interaction, there is a visible elastic post-buckling asymmetry concerning the columns with pure distortional imperfections: the $\theta=0^o$ (inward) column exhibits slightly higher post-buckling strengths than its $\theta=180^o$ (outward) counterpart. However, note that, regardless of the imperfection "sign", the column post-buckling strength is always a bit higher than in the absence of LP/D interaction, which stems from the progressive emergence of a (rather small) local-plate component, known to exhibit a much larger post-critical strength reserve – Figures 6(a)-(b) compare the evolutions of the $\theta=0^o$ and $\theta=180^o$ column web deformed configurations with an *exact sinusoid shape* – these comparisons clearly reveal the presence of the local-plate *3* half-wave sinusoidal component, thus confirming the occurrence of the buckling mode interaction [16].

(ii) All elastic equilibrium paths associated with predominantly local-plate imperfections (namely the ones concerning the $\theta=90^o$ and $\theta=270^o$ columns) exhibit a distinct "irregular" behaviour: regardless of the $w_{LP.0}$ sign, they (ii$_1$) are less "smooth" then the $\theta=0^o$ and $\theta=180^o$ column paths, which always evolve in a monotonic fashion, (ii$_2$) exhibit limit points, associated with "snap-through" phenomena[2], and, for $P/P_{cr}>1.1$, (ii$_3$) merge with either the $\theta=180^o$ column (majority of them) or $\theta=0^o$ column paths. This means that, even in the presence of pure *3* half-wave local-plate imperfections ($v_{D.0}=0$), the column evolves towards a predominantly distortional single half-wave deformed configuration – this evolution often includes significant web *bending reversal*, which explains the occurrence of the limit points appearing in the (elastic) equilibrium paths displayed in Figures. 3(a)-(b).

(iii) Generally speaking, the elastic-plastic equilibrium paths of the various columns also merge with the ones corresponding to $\theta=0^o$ or $\theta=180^o$. Depending on the f_y/σ_{cr} value, this merging may occur after or before the column has reached its ultimate strength – see Figures. 3(a)-(b). However, merging never occurs for $f_y/\sigma_{cr}\approx 1.2$ – an explanation for this fact is provided below, in item (vi).

---

[2] The "snap-through" becomes more "abrupt" as the amplitude of the initial imperfection local-plate component grows. When the imperfections are pure or "almost pure", one even observes a minor "snap-back" phenomenon (*e.g.*, the $\theta=90^o$ column).

(iv) The onset of yielding always takes place inside the load interval $0.8 < P/P_{cr} < 1.3$ (obviously, the exact load value depends on the yield-to-critical stress ratio and initial imperfection shape) and defines the point of separation between the elastic and elastic-plastic equilibrium paths. For a given f_y / σ_{cr} value, this separation takes place for higher load levels in columns with pure local-plate imperfections (θ=90° or θ=270°) than in columns with pure distortional ones (θ=0° or θ=180°) – the difference may reach about 20% (*e.g.*, θ=180° *vs.* θ=270°, for $f_y/\sigma_{cr} \approx 2$).

(v) For $f_y / \sigma_{cr} \geq 2$, plasticity appears first at the free ends of the mid-span cross-section section lips, as shown in Figures. 5(b_1)-(b_2).

(vi) For $f_y / \sigma_{cr} \approx 1.2$, yielding starts while the column is still subjected to a fairly uniform stress distribution, leading to a very "sudden" collapse – a large portion of the column yields at practically the same time. In this case, the shape of the initial imperfection governs the location of zone where yielding begins.

(vii) For $f_y/\sigma_{cr} \geq 3.5$, collapse only occurs after the full yielding of the column mid-span zones located around the web-flange corners, as shown in the right side of Figures. 5(b_1)-(b_2). However, one should point out that the collapse mechanism is different in columns with outward and inward flange-lip motions. In the former, one observes the formation of a "three hinge flange mechanism" – see the right side of Figure. 5(b_2). In the latter, the plastic deformation is restricted to the close vicinity of the mid-span cross-section – see the right side of Figure. 5(b_1).

(viii) For $f_y / \sigma_{cr} \geq 3.5$, the onset of yielding does not precipitate failure, even when associated with a "snap-through" phenomenon (*e.g.*, $f_y / \sigma_{cr} \approx 3.5$ and any imperfection shape with a local-plate component) – the column still exhibits a certain amount of post-bucking strength reserve, which is more substantial for $f_y/\sigma_{cr} \approx 5.5$ and outward flange-lip motion – see Figure. 3(a). It is still worth noting that failure occurs after the various equilibrium paths have already merged together, which means that the initial imperfection shape has little influence on the column load-carrying capacity and failure mechanism.

(ix) The outward pure distortional initial imperfection is the most *detrimental* one, as it leads to the lowest column load-carrying capacities. This feature has far-reaching implications in the design of cold-formed steel columns affected by local-plate/distortional mode interaction – see the next subsection.

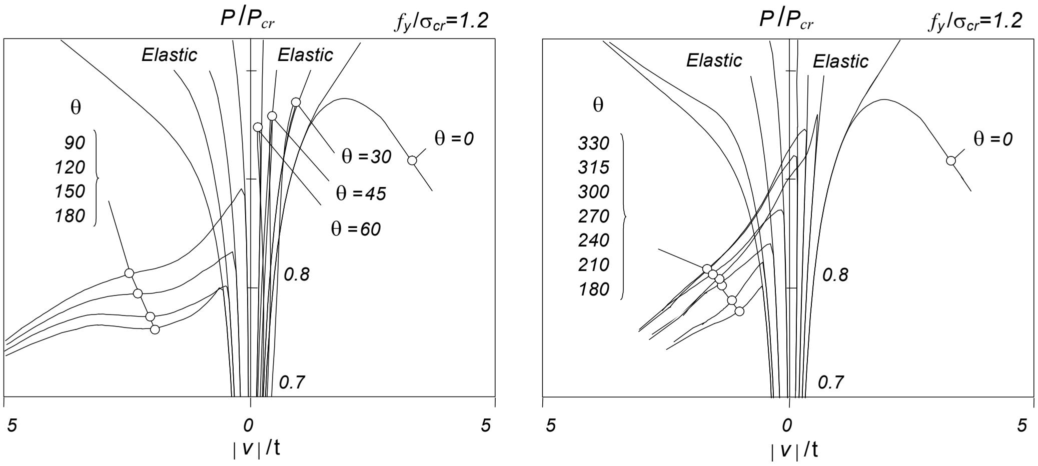

(a) (b)

Figure 4. Column Elastic and Elastic-Plastic ($f_y/\sigma_{cr} \approx 1.2$) Post-Buckling Equilibrium Paths P/P_{cr} *vs.* v/t: (a) $0° \leq \theta \leq 180°$ and (b) $180° \leq \theta \leq 360°$

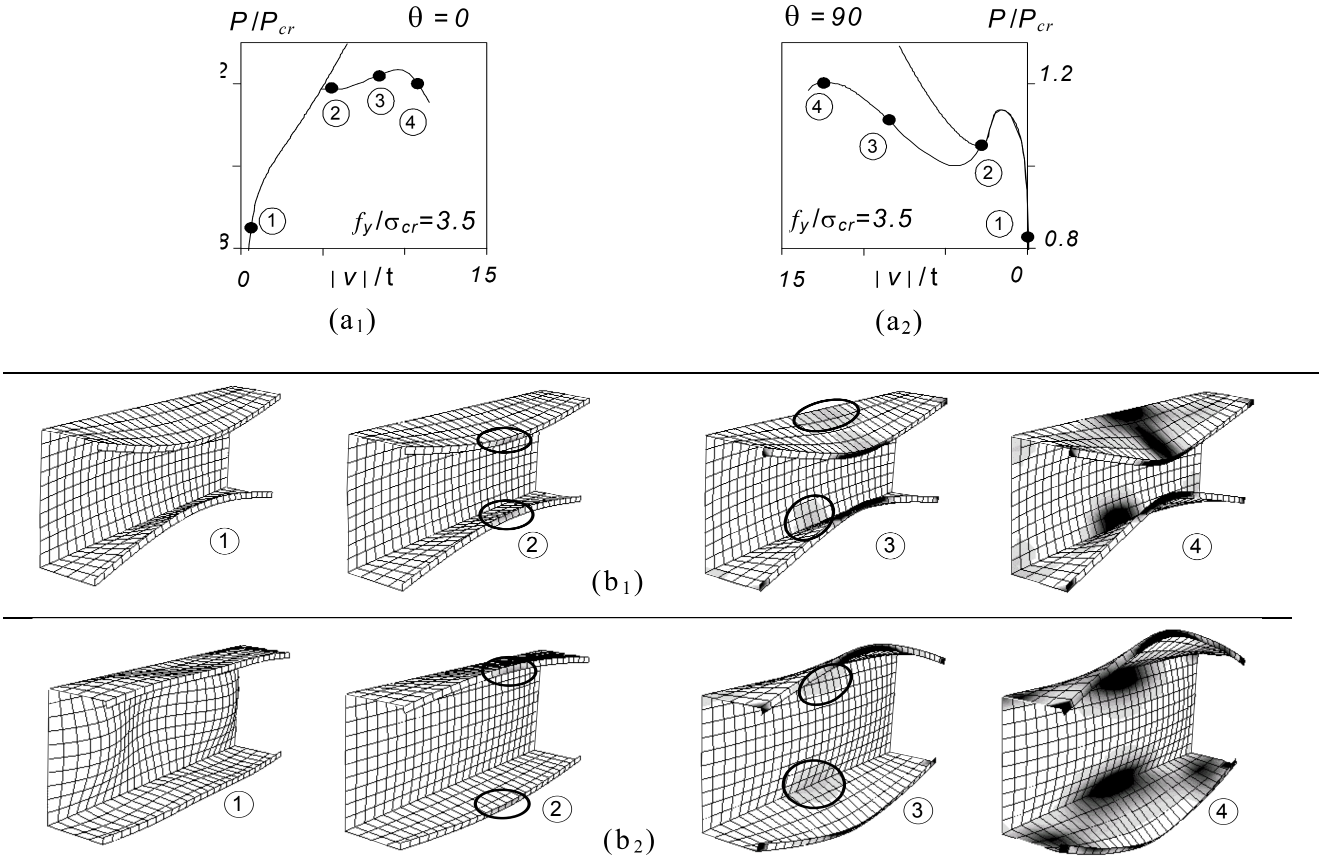

Figure 5. (a) Equilibrium Points on P/P_{cr} *vs.* v/t Post-Buckling Paths and (b) Associated Plastic Strain Diagrams and Failure Modes for Columns Defined by: (1) $\theta=0^o+f_y/\sigma_{cr}\approx 3.5$ and (2) $\theta=90^o+f_y/\sigma_{cr}\approx 3.5$

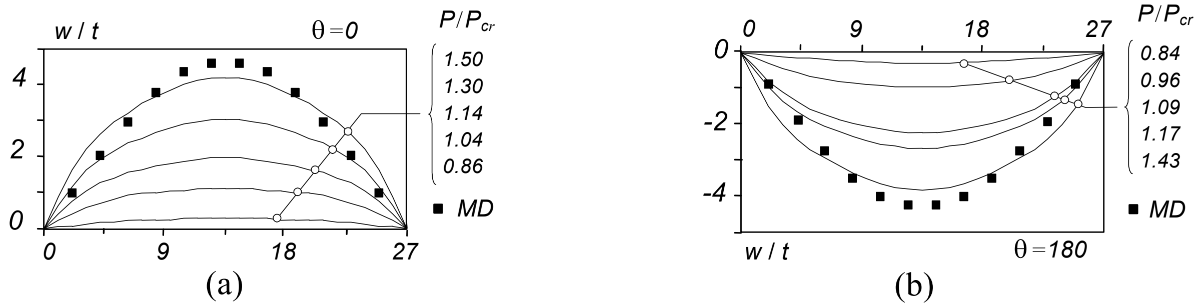

Figure 6. Web Deformed Configuration Evolution for the (a) $\theta=0^o$ and (b) $\theta=180^o$ Columns

3. DIRECT STRENGTH METHOD

Next, one presents the results of an investigation aimed at developing and assessing the performance of an approach based on the Direct Strength Method (DSM) and intended to estimate the ultimate strength of lipped channel columns affected by LP/D mode interaction [12, 13]. In order to achieve this goal in a proper fashion, it is indispensable to possess a significant amount of reliable experimental and/or numerical ultimate strength values concerning columns with close (almost coincident) local-plate and distortional critical buckling stresses. Therefore, it was decided to carry out an extensive parametric study, destined to acquire a fairly large data bank of column ultimate strengths on which to base the assessment and/or improvement of the current DSM design methodology – these ultimate strengths were obtained through second-order elastic-plastic shell finite element analyses performed in the code ABAQUS [17], as briefly described earlier.

3.1 Current DSM Design Approach

When compared with the traditional "*effective width* approach", the DSM exhibits three major innovative features, all stemming from the fact that the cross-section is now viewed as a *whole*: (i) wall-restraint effects are automatically taken into account, (ii) no effective width calculations are needed and (iii) it is possible to provide strength estimates for members failing in *distortional* modes. Moreover, the DSM provides a rational and systematic framework for the design of thin-walled members with arbitrary cross-section shapes, loadings or failure modes – of course, a given application needs proper calibration and validation (*i.e.*, comparison with a fair number of experimental and/or numerical results). Finally, note that both the DSM and effective width approaches share the same basic assumption: the member ultimate strength can be accurately predicted solely on the basis of its elastic buckling and yield stresses.

The available DSM applications adopt "Winter-type" design curves, which have been calibrated against a large number of experimental and/or numerical results [19]. It was shown that, whenever a given column fails in pure local-plate or distortional modes, it is possible to obtain safe and accurate ultimate strength estimates on the basis of the elastic buckling and yield stress values. Thus, the DSM prescribes that the column *nominal strengths* against *local-plate* and *distortional* failure (P_{NL} and P_{ND}) are given by the expressions [2]

$$\begin{cases} P_{NL} = P_Y & if \quad \lambda_L \leq 0.776 \\ P_{NL} = P_Y \left(\dfrac{P_{CRL}}{P_Y} \right)^{0.4} \left[1 - 0.15 \left(\dfrac{P_{CRL}}{P_Y} \right)^{0.4} \right] & if \quad \lambda_L > 0.776 \end{cases} \tag{3}$$

$$\begin{cases} P_{ND} = P_Y & if \quad \lambda_D \leq 0.561 \\ P_{ND} = P_Y \left(\dfrac{P_{CRD}}{P_Y} \right)^{0.6} \left[1 - 0.25 \left(\dfrac{P_{CRD}}{P_Y} \right)^{0.6} \right] & if \quad \lambda_D > 0.561 \end{cases} \tag{4}$$

where (i) $\lambda_L=(P_Y /P_{CRL})^{0.5}$ and $\lambda_D=(P_Y /P_{CRD})^{0.5}$, (ii) P_Y is the squash load and (iii) P_{CRL} and P_{CRD} are the *local-plate* and *distortional* critical buckling loads. In order to capture the local-plate/global or distortional/global interaction, the DSM approach proposes the replacement of P_Y by P_{NE} in Eq. 3 or Eq. 4, where P_{NE} is the column buckling strength associated with *global* (Euler) failure. At this point, it is worth noting that an accurate prediction of the column distortional failure load has considerable practical relevance, since (i) the distortional post-critical strength reserve is considerably lower and more imperfection-sensitive than its local-plate counterpart and (ii) there exists clear (numerical) evidence that the collapse of columns buckling in local-plate modes is often associated with a distortional failure mechanism [14].

3.2 DSM for Local-Plate/Distortional Interaction

Following a strategy similar to the one used to develop safety-checking rules that account for local-plate/global effects, it is possible to propose expressions to estimate the ultimate strength of columns experiencing local-plate/distortional interaction. This was first achieved by Schafer [20, 21], who proposed two distinct approaches: (i) replacing P_Y by P_{ND} in Eq. 3 (NLD approach – schematically depicted in the flowchart shown in Figure. 7(a)) or (ii) replacing P_Y by P_{NL} in Eq. 4 (NDL approach – see Figure. 7(b)), where P_{ND} and P_{NL} are the distortional and local-plate buckling strengths also given by Eqs. 3 and 4. Yang and Hancock [10] recently adopted the NLD approach to investigate the LP/D interaction in lipped channel columns with "v-shape" web and flange intermediate stiffeners. After comparing the ultimate strength estimates provided by the NLD approach with the results of a series of experimental tests performed in Sydney, which provided evidence of adverse local-plate/distortional interaction, these authors concluded that (i) the above estimates were always safe and reasonably accurate (differences within the *10-20%* range) and also that (ii) further investigation is required on the design of columns with nearly coincident local-plate and distortional buckling stresses. Finally, note that the use of Eqs. 3 and 4 requires the knowledge of *accurate* local-plate and distortional buckling loads (P_{CRL}, P_{CRD}), which can be obtained through shell finite element analyses, finite strip analyses or Generalised Beam Theory (GBT) analyses.

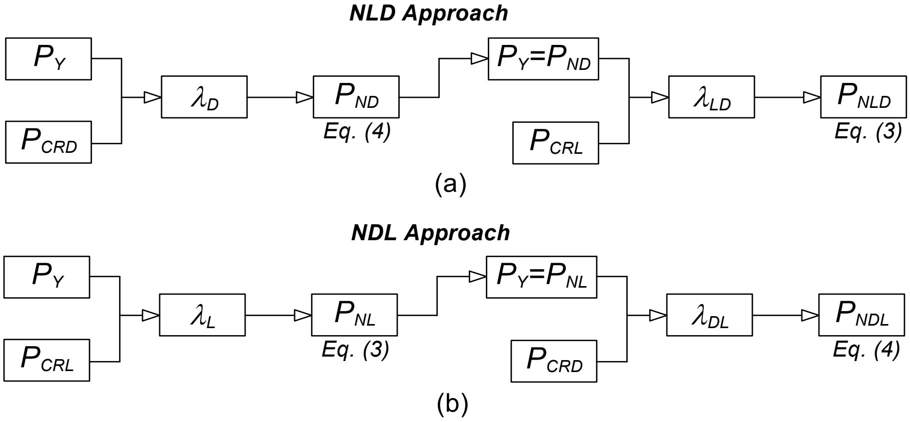

Figure 7. Flowcharts Concerning the Determination of the Nominal Strength of Columns Experiencing LP/D Interaction Effects: (a) P_{NLD} and (b) P_{NDL} Approaches

4. PARAMETRIC STUDY: SCOPE AND NUMERICAL RESULTS

In order to be able to carry out a fairly large parametric study involving the ultimate strength of lipped channel columns affected by local-plate/distortional interaction, their geometries had to be carefully selected: it was necessary to find sets of cross-section dimensions and length values making it possible to "control" the closeness between the column local-plate and distortional critical buckling stresses (σ_{CRL} and σ_{CRD}) or loads (P_{CRL} and P_{CRD}). This goal was achieved by adopting the following strategy:

(i) Initially, a trial-and-error approach was employed to find six "basic cross-section shapes", displaying commonly used dimensions and ensuring the coincidence between σ_{CRL} and σ_{CRD}. This search led to the three *slender* ($1.4 \leq \lambda_D \leq 2.6$) and three *stocky* ($0.6 \leq \lambda_D \leq 1.4$) cross-sections exhibiting the following dimensions (web width b_w, flange width b_f, stiffener/lip width b_s and wall thickness t)

(i.1) Slender cross-sections: (i_1) $b_w=100, b_f=50, b_s=5, t=1.0mm$ (Slender Column 1 – SLC1), (i_2) $b_w=120, b_f=80, b_s=10, t=1.3mm$ (SLC2) and (i_3) $b_w=95, b_f=80, b_s=10, t=0.95mm$ (SLC3).

(i.2) Stocky cross-sections: (i_1) $b_w=180, b_f=100, b_s=20, t=3.4mm$ (Stocky Column 1 – STC1), (i_2) $b_w=110, b_f=78, b_s=30, t=2.8mm$ (STC2) and (i_3) $b_w=100, b_f=100, b_s=26, t=2.0mm$ (STC3).

One should mention that all the above six column cross-section dimensions satisfy the requirements that have been adopted in the existing DSM approach – i.e., they are "pre-qualified columns".

(ii) Subsequently, the closeness between σ_{CRL} and σ_{CRD} was slightly altered, by just changing a single basic cross-section dimension: either the flange width b_f, the web width b_w or the stiffener width b_s. This procedure led to the identification of various columns with (ii_1) cross-section dimensions generated from the six basic shapes and (ii_2) very close (but not necessarily coincident) σ_{CRL} and σ_{CRD} values – the alterations were made in such a way that one has always $0.90 \leq \sigma_{CRL} / \sigma_{CRD} \leq 1.10$ (*i.e.*, the critical stresses are never more than *10%* apart).

Concerning the column lengths considered, they always correspond to single distortional half-waves associated with the buckling stresses σ_{CRD} and were determined by means of finite strip analyses. As for the column steel material behaviour, it is characterised by $E=210\ GPa$ (Young's modulus), $\nu=0.3$ (Poisson's ratio) and $f_y=250\text{-}350\text{-}550\ MPa$ (three yield stress values are considered in this work, all of them also meeting the DSM limit stress requirements for "pre-qualified columns"). Finally, it is worth (i) mentioning that no residual stresses have been taken into account (it has been shown that have very little impact on the column ultimate strength – *e.g.*, [22, 23]) and (ii) addressing the criterion adopted to select the initial geometrical imperfections included in the non-linear analyses that provide the column ultimate strengths:

(i) Regardless of their critical stress ratios $\sigma_{CRL}/\sigma_{CRD}$, all the columns analysed contained initial geometrical imperfections with a single-wave distortional buckling mode shape, having an amplitude (mid-span flange-lip corner displacement) equal to *10%* of the wall thickness t and involving *outward* motions of the flange-lip assemblies – previous studies involving lipped channel columns with $\sigma_{CRL}=\sigma_{CRD}$ showed that this imperfection shape is the *most detrimental* one, in the sense that it corresponds to the lowest column post-buckling strength and collapse load [15, 16].

(ii) The *slender* columns with $\sigma_{CRL}/\sigma_{CRD} < 1.0$ (*i.e.*, with critical *local-plate* buckling modes exhibiting several half-waves) were also analysed in the presence of *critical-mode* initial geometrical imperfections, again with amplitude $0.1\,t$ – it now corresponds to the mid-web flexural displacement at mid-span.

(iii) All initial geometrical imperfections defined earlier (buckling mode shapes with amplitude $0.1\,t$) are included in the analyses through a specific ABAQUS command. In the columns buckling in local-plate modes ($\sigma_{CRL} < \sigma_{CRD}$), the single-wave distortional imperfection is, effectively, the column higher-order buckling mode most resembling it, which means that it is not possible to guarantee the complete "purity" of the distortional shape – in other words, a small participation of a multiple half-wave local-plate mode is virtually undetectable (but with only a very minute affect the column ultimate strength).

A total of *66 slender* and *45 stocky* columns were analysed, corresponding to all possible combinations of *16* (*15*) different cross-section shapes and *3* yield stress values. All cross-section dimensions (b_w, b_f, b_s, t), lengths (L), critical stresses (σ_{CRL}, σ_{CRD}), yield stresses (f_y) and initial imperfection shapes (D, LP) considered in this work are given in Tables 1-2 (*slender* columns) and 3-4 (*stocky* columns), presented further ahead.

The numerical results displayed in Tables 1 to 4 consist of column average stresses at collapse ($\sigma_U=P_U/A$) and the nature of the corresponding failure mechanisms. In order to convey the meaning of these results, they are illustrated in Figure. 8(a), which shows the post-buckling equilibrium paths (σ/σ_{CR} *vs.* v/t) concerning columns with (i) $\sigma_{CRL}=\sigma_{CRD}$ ($\equiv\sigma_{CR}$), (ii) identical outward distortional imperfections and (iii) four different yield stresses ($f_y/\sigma_{CR}\approx 1.2, 2.0, 3.5, 5.5$). It is worth noting that the onset of yielding, which always takes place in the stiffener free ends (see Figure. 8(b_1)), occurs at the equilibrium points **A** and may or may not trigger the column failure – it depends on the particular f_y/σ_{CR} value. Indeed, for large enough f_y/σ_{CR} values, failure occurs at a limit point **B**, following (i) a "snap-through" phenomenon and (ii) the yielding of the column central regions located around the web-flange corners (see Figure. 8(b_2)) – Figure. 8(c) shows the corresponding (predominantly distortional) failure mechanism.

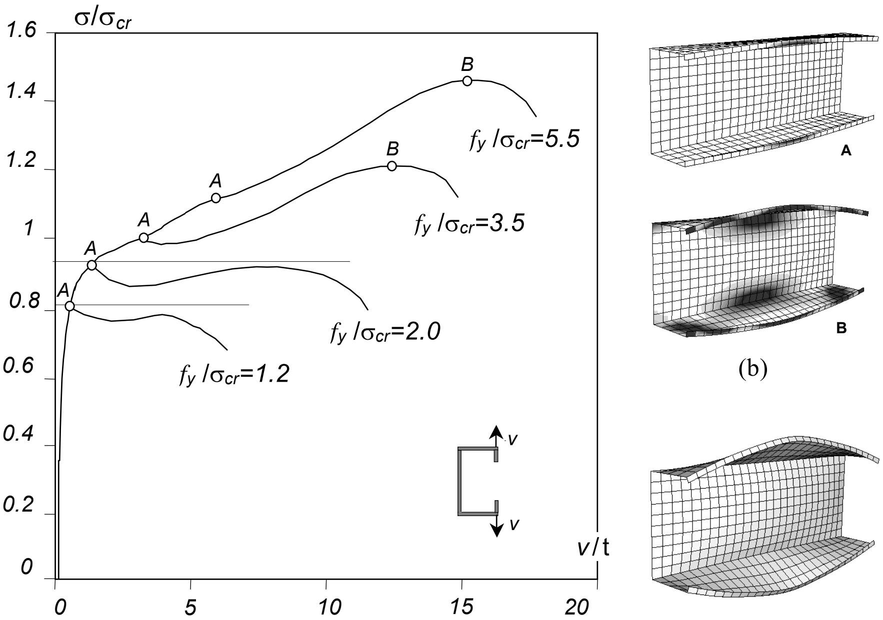

(a) (c)

Figure 8. Column (a) Post-Buckling Equilibrium Paths,
(b) Plastic Strain Distributions and (c) Failure Mechanism

Table 1(a). Comparison Between the "Exact" and DSM (σ_{NLD}) Ultimate Strength Estimates (SLC1)

					FEA				DSM				
	b_f	L	Imp.	f_y	σ_L	σ_D	σ_U	Fail.	λ_D	σ_{ND}	λ_{LD}	σ_{NLD}	σ_{NLD}/σ_U
b_w=100mm, b_s=5mm, t=1mm	55	300	D	250	101	91	94	B	1.66	117	1.08	95	1.01
				350			110	B	1.97	138	1.17	106	0.96
				550			131	A	2.46	171	1.30	121	0.93
	52.5	280	D	250	101	96	97	B	1.61	121	1.09	97	1.00
				350			114	B	1.91	143	1.19	108	0.95
				550			137	A	2.39	176	1.32	124	0.91
	50	270	D	250	102	102	102	B	1.57	125	1.11	99	0.97
				350			120	B	1.85	147	1.20	110	0.92
				550			147	A	2.32	182	1.34	127	0.86
	47.5	260	D	250	102	108	107	B	1.52	128	1.12	101	0.94
				350			127	B	1.80	151	1.22	113	0.89
				550			156	A	2.26	187	1.35	130	0.83
	45	260	D	250	103	113	115	B	1.48	131	1.13	103	0.90
				350			136	B	1.76	155	1.23	115	0.85
				550			168	A	2.20	193	1.37	132	0.79
	47.5	260	LP	250	102	108	118	A	1.52	128	1.12	101	0.86
				350			127	B	1.80	151	1.22	113	0.89
				550			157	B	2.26	187	1.35	130	0.83
	45	260	LP	250	103	113	128	A	1.48	131	1.13	103	0.80
				350			142	B	1.76	155	1.23	115	0.81
				550			168	B	2.20	193	1.37	132	0.79

Table 1(b). Comparison Between the "Exact" and DSM (σ_{NLD}) Ultimate Strength Estimates (SLC2)

					FEA				DSM				
	b_w	L	Imp.	f_y	σ_L	σ_D	σ_U	Fail.	λ_D	σ_{ND}	λ_{LD}	σ_{NLD}	σ_{NLD}/σ_U
b_f=80mm, b_s=10mm, t=1.3mm	130	550	D	250	100	110	105	A	1.51	129	1.14	101	0.96
				350			107	B	1.78	153	1.24	113	1.05
				550			123	B	2.24	189	1.38	130	1.05
	125	550	D	250	107	113	107	A	1.49	131	1.11	104	0.97
				350			109	A	1.76	155	1.20	116	1.07
				550			123	B	2.21	192	1.34	134	1.09
	120	550	D	250	115	115	109	A	1.47	133	1.07	108	0.99
				350			111	A	1.74	157	1.17	120	1.08
				550			124	B	2.18	194	1.30	139	1.12
	115	550	D	250	124	118	112	A	1.45	134	1.04	111	0.99
				350			114	A	1.72	159	1.13	124	1.09
				550			122	B	2.16	197	1.26	143	1.18
	110	550	D	250	135	121	114	A	1.44	136	1.00	115	1.01
				350			116	A	1.70	161	1.09	129	1.11
				550			121	A	2.13	199	1.22	149	1.23
	100	550	D	250	157	127	119	A	1.40	139	0.94	123	1.03
				350			122	A	1.66	164	1.02	138	1.13
				550			126	A	2.08	204	1.14	159	1.26
	125	550	LP	250	107	113	119	A	1.49	131	1.11	104	0.88
				350			120	A	1.76	155	1.20	116	0.97
				550			122	B	2.21	192	1.34	134	1.10
	130	550	LP	250	100	110	120	A	1.51	129	1.14	101	0.84
				350			121	A	1.78	153	1.24	113	0.93
				550			123	B	2.24	189	1.38	130	1.05

Table 1(c). Comparison Between the "Exact" and DSM (σ_{NLD}) Ultimate Strength Estimates (SLC3)

					FEA				DSM				
	b_s	L	Imp.	f_y	σ_L	σ_D	σ_U	Fail.	λ_D	σ_{ND}	λ_{LD}	σ_{NLD}	σ_{NLD}/σ_U
b_w=95 mm, b_f=80 mm, t=0.95 mm	11	650	D	250	92	100	94	A	1.58	123	1.16	95	1.01
				350			95	A	1.87	145	1.26	106	1.11
				550			99	A	2.35	180	1.40	122	1.23
	10.5	650	D	250	92	96	91	A	1.62	121	1.15	94	1.03
				350			92	A	1.91	142	1.25	104	1.13
				550			97	A	2.40	176	1.39	120	1.24
	10	600	D	250	91	91	86	A	1.65	118	1.14	92	1.07
				350			87	A	1.96	139	1.23	103	1.17
				550			92	A	2.45	171	1.37	118	1.28
	9.5	600	D	250	91	87	83	A	1.70	115	1.12	91	1.10
				350			84	A	2.01	135	1.22	101	1.20
				550			91	B	2.51	167	1.35	116	1.27
	9	550	D	250	91	83	78	A	1.74	112	1.11	89	1.14
				350			79	A	2.06	132	1.20	99	1.25
				550			84	A	2.58	162	1.34	114	1.35
	10.5	650	LP	250	92	96	109	A	1.62	121	1.15	94	0.86
				350			109	A	1.91	142	1.25	104	0.96
				550			109	A	2.40	176	1.39	120	1.10
	11	650	LP	250	92	100	114	A	1.58	123	1.16	95	0.83
				350			114	A	1.87	145	1.26	106	0.93
				550			114	A	2.35	180	1.40	122	1.07

Table 2(a). Comparison Between the “Exact” and DSM (σ_{NDL}) Ultimate Strength Estimates (SLC1)

					FEA				DSM				
	b_f	L	Imp.	f_y	σ_L	σ_D	σ_U	Fail.	λ_L	σ_{NL}	λ_{DL}	σ_{NDL}	σ_{NDL}/σ_U
b_w=100mm, b_s=5mm, t=1mm	55	300	D	250	101	91	94	B	1.58	156	1.31	92	0.98
				350			110	B	1.86	193	1.46	103	0.94
				550			131	A	2.34	258	1.69	119	0.91
	52.5	280	D	250	101	96	97	B	1.57	156	1.27	95	0.98
				350			114	B	1.86	194	1.42	106	0.93
				550			137	A	2.33	258	1.64	123	0.90
	50	270	D	250	102	102	102	B	1.57	156	1.24	97	0.96
				350			120	B	1.85	194	1.38	109	0.91
				550			147	A	2.32	259	1.59	127	0.86
	47.5	260	D	250	102	108	107	B	1.56	157	1.21	100	0.94
				350			127	B	1.85	194	1.34	112	0.89
				550			156	A	2.32	259	1.55	130	0.84
	45	260	D	250	103	113	115	B	1.56	157	1.18	103	0.89
				350			136	B	1.84	195	1.31	115	0.85
				550			168	A	2.31	260	1.51	134	0.80
	47.5	260	LP	250	102	108	118	A	1.56	157	1.21	100	0.85
				350			127	B	1.85	194	1.34	112	0.89
				550			157	B	2.32	259	1.55	130	0.83
	45	260	LP	250	103	113	128	A	1.56	157	1.18	103	0.80
				350			142	B	1.84	195	1.31	115	0.81
				550			168	B	2.31	260	1.51	134	0.80

Table 2(b). Comparison Between the “Exact” and DSM (σ_{NDL}) Ultimate Strength Estimates (SLC2)

					FEA				DSM				
	b_w	L	Imp.	f_y	σ_L	σ_D	σ_U	Fail.	λ_L	σ_{NL}	λ_{DL}	σ_{NDL}	σ_{NDL}/σ_U
b_f=80mm, b_s=10mm, t=1.3mm	130	550	D	250	100	110	105	A	1.58	155	1.19	101	0.96
				350			107	B	1.87	193	1.32	113	1.06
				550			123	B	2.35	257	1.53	131	1.07
	125	550	D	250	107	113	107	A	1.53	159	1.19	103	0.96
				350			109	A	1.81	198	1.32	116	1.06
				550			123	B	2.27	264	1.53	135	1.09
	120	550	D	250	115	115	109	A	1.47	163	1.19	106	0.97
				350			111	A	1.74	203	1.33	119	1.07
				550			124	B	2.18	271	1.53	138	1.11
	115	550	D	250	124	118	112	A	1.42	168	1.19	108	0.97
				350			114	A	1.68	209	1.33	122	1.07
				550			122	B	2.10	278	1.53	142	1.16
	110	550	D	250	135	121	114	A	1.36	172	1.19	111	0.98
				350			116	A	1.61	214	1.33	125	1.08
				550			121	A	2.02	287	1.54	145	1.20
	100	550	D	250	157	127	119	A	1.26	182	1.20	117	0.98
				350			122	A	1.49	226	1.34	132	1.08
				550			126	A	1.87	303	1.55	153	1.21
	125	550	LP	250	107	113	119	A	1.53	159	1.19	103	0.87
				350			120	A	1.81	198	1.32	116	0.97
				550			122	B	2.27	264	1.53	135	1.10
	130	550	LP	250	100	110	120	A	1.58	155	1.19	101	0.84
				350			121	A	1.87	193	1.32	113	0.93
				550			123	B	2.35	257	1.53	131	1.07

Table 2(c). Comparison Between the “Exact” and DSM (σ_{NDL}) Ultimate Strength Estimates (SLC3)

					FEA				DSM				
	b_s	L	Imp.	f_y	σ_L	σ_D	σ_U	Fail.	λ_L	σ_{NL}	λ_{DL}	σ_{NDL}	σ_{NDL}/σ_U
b_w=95 mm, b_f=80 mm, t=0.95 mm	11	650	D	250	92	100	94	A	1.65	150	1.23	95	1.00
				350			95	A	1.96	187	1.37	106	1.12
				550			99	A	2.45	249	1.58	123	1.24
	10.5	650	D	250	92	96	91	A	1.65	150	1.25	93	1.02
				350			92	A	1.96	187	1.40	104	1.13
				550			97	A	2.45	249	1.61	120	1.24
	10	600	D	250	91	91	86	A	1.65	150	1.28	91	1.05
				350			87	A	1.96	187	1.43	102	1.17
				550			92	A	2.45	249	1.65	118	1.28
	9.5	600	D	250	91	87	83	A	1.66	150	1.31	89	1.08
				350			84	A	1.96	187	1.46	99	1.19
				550			91	B	2.46	248	1.69	115	1.26
	9	550	D	250	91	83	78	A	1.66	150	1.35	87	1.11
				350			79	A	1.96	186	1.50	97	1.22
				550			84	A	2.46	248	1.73	112	1.33
	10.5	650	LP	250	92	96	109	A	1.65	150	1.25	93	0.85
				350			109	A	1.96	187	1.40	104	0.95
				550			109	A	2.45	249	1.61	120	1.10
	11	650	LP	250	92	100	114	A	1.65	150	1.23	95	0.83
				350			114	A	1.96	187	1.37	106	0.93
				550			114	A	2.45	249	1.58	123	1.08

5. ASSESSMENT OF THE DSM ESTIMATES

The numerical and DSM results given in Tables 1 and 2 concern the *66 slender* columns analysed (geometries SLC1, SLC2 and SLC3) and enable the comparison between the “exact” ultimate strengths ($\sigma_U = P_U / A$) and the estimates yielded by the two proposed DSM approaches, namely $\sigma_{NDL} = P_{NDL} / A$ and $\sigma_{NLD} = P_{NLD} / A$ – also indicated are the values of the σ_{ND} and σ_{NL} estimates. The observation of the results presented in these two tables prompts the following remarks:

(i) The σ_U values concerning local-plate (LP) imperfections never fall below their distortional (D) counterparts, thus confirming that the distortional imperfections are the *most detrimental* ones. As the DSM does not capture the effect of the imperfection shape, its estimates should preferably approximate well the σ_U values concerning the D imperfections. If this is the case, then the DSM estimates will be more or less conservative for columns containing LP imperfection components.

(ii) The σ_{NDL} and σ_{NLD} estimates are very similar, even if the “quality” of the former is slightly higher – the σ_{NDL} / σ_U and σ_{NLD} / σ_U means and standard deviations are *1.01* vs. *1.02* and *0.13* vs. *0.14*. Although the whole sets of σ_{NDL} and σ_{NLD} estimates may be viewed as quite accurate (means very close to *1.00*), one must also recognise that their scatters are rather high (standard deviations above *0.12*).

(iii) Out of the *66* σ_{NDL} estimates, *1* is exact, *19* are safe and accurate ($\sigma_{NDL} / \sigma_U \geq 0.9$), *16* are too safe ($0.80 \leq \sigma_{NLD} / \sigma_U < 0.90$), *15* are a bit unsafe ($\sigma_{NDL} / \sigma_U \leq 1.10$) and *15* are too unsafe ($1.10 < \sigma_{NDL} / \sigma_U \leq 1.33$).

(iv) Out of the *66* σ_{NLD} estimates, *1* is exact, *16* are safe and accurate ($\sigma_{NLD}/\sigma_U \geq 0.9$), *15* are too safe ($0.79 \leq \sigma_{NLD}/\sigma_U < 0.90$), *17* are a bit unsafe ($\sigma_{NLD}/\sigma_U \leq 1.10$) and *17* are too unsafe ($1.10 < \sigma_{NLD}/\sigma_U \leq 1.35$).

(v) Both the local-plate (σ_{NL}) and distortional (σ_{ND}) DSM expressions clearly overestimate the ultimate strengths (σ_U) of the slender columns affected by local-plate/distortional mode interaction.

As for Tables 3 and 4, they display similar numerical ($\sigma_U = P_U/A$) and DSM ($\sigma_{NDL} = P_{NDL}/A$, $\sigma_{NLD} = P_{NLD}/A$) results for the *45 stocky* columns considered in this study (geometries STC1, STC2 and STC3). The observation of these results leads to the following comments:

(i) Although the σ_{NDL} and σ_{NLD} estimates are once more very similar, the slightly higher "quality" belongs this time to the latter – the σ_{NDL}/σ_U and σ_{NLD}/σ_U means and standard deviations are *0.88* vs. *0.90* and *0.061* vs. *0.057*. One notices that the whole sets of σ_{NDL} and σ_{NLD} estimates are now a bit conservative (means around *0.90*), but exhibit relatively low scatters (standard deviations around *0.06*) – moreover, there are no unsafe predictions at all.

(ii) Out of the *45* σ_{NLD} estimates, *24* are both safe and accurate ($\sigma_{NLD}/\sigma_U \geq 0.9$) and *21* are excessively safe ($0.80 \leq \sigma_{NLD}/\sigma_U < 0.90$).

(iii) Out of the *45* σ_{NDL} estimates, *19* are both safe and accurate ($\sigma_{NDL}/\sigma_U \geq 0.9$) and *26* are excessively unsafe ($0.78 \leq \sigma_{NLD}/\sigma_U < 0.90$).

(iv) Unlike in the case of the slender columns, the distortional DSM expressions (σ_{ND}) now provide reasonably accurate ultimate strength estimates for the stocky columns affected by local-plate/distortional interaction – indeed, only in *8* columns (out of *45*), all of them concerning the higher yield stress ($f_y = 550\ MPa$), are the σ_{ND} estimates larger than the σ_U values. Conversely, the local-plate DSM expressions (σ_{NL}) often lead mostly to an overestimation of the stocky column σ_U values – only in *10* columns do the σ_{NL} values fall below the σ_U ones.

In view of the facts outlined and explained above, the authors believe that the σ_{NLD} approach is superior to the σ_{NDL} one (although the differences are not at all substantial) – therefore, the results presented hereafter are based on the assumption that the σ_{NLD} approach is adopted. In this context, Figures. 9 (slender columns) and 10 (stocky columns) make it possible to assess how the stress ratios $\sigma_{CRD}/\sigma_{CRL}$ and σ_{NLD}/σ_U vary with the cross-section dimensions b_f, b_w, b_s – the latter for $f_y = 250$, *350*, *550 MPa*. From the observation of these two figures, one readily concludes that:

(i) Both the slender and stocky columns have stress ratios $\sigma_{CRD}/\sigma_{CRL}$ and σ_{NLD}/σ_U that always exhibit opposite variations with the cross-section dimensions – this suggests that the $\sigma_{CRD}/\sigma_{CRL}$ value may be used to improve the σ_{NLD} estimates (and also the σ_{NDL} ones, for that matter).

(ii) The slender column σ_{NLD} estimates are all safe in the first plots, mostly unsafe in the second and almost all unsafe in the third. This "safety drop" is most likely related to the b_f/b_w ratio increase: *0.45-0.55* (first plot), *0.61-0.73* (second) and *0.84-0.84* (third).

Table 3(a). Comparison Between the “Exact” and DSM (σ_{NLD}) Ultimate Strength Estimates (STC1)

					FEA			DSM				
	b_f	L	Imp.	f_y	σ_{CRL}	σ_{CRD}	σ_U	λ_D	σ_{ND}	λ_{LD}	σ_{NLD}	σ_{NLD}/σ_U
b_w=180mm, b_s=20mm, t=3.4mm	90	650	D	250	361	399	240	0.79	221	0.78	220	0.92
				350			298	0.94	276	0.87	256	0.86
				550			361	1.17	360	1.00	306	0.85
	95	650	D	250	358	377	231	0.81	218	0.78	217	0.94
				350			287	0.96	270	0.87	252	0.88
				550			341	1.21	351	0.99	300	0.88
	100	650	D	250	355	355	222	0.84	213	0.78	213	0.96
				350			276	0.99	264	0.86	247	0.90
				550			323	1.24	342	0.98	294	0.91
	105	650	D	250	353	338	217	0.86	210	0.77	210	0.97
				350			267	1.02	259	0.86	243	0.91
				550			307	1.28	334	0.97	289	0.94
	110	650	D	250	350	320	211	0.88	206	0.77	206	0.98
				350			256	1.04	253	0.85	239	0.93
				550			292	1.31	326	0.96	284	0.97

Table 3(b). Comparison Between the “Exact” and DSM (σ_{NLD}) Ultimate Strength Estimates (STC2)

					FEA			DSM				
	b_f	L	Imp.	f_y	σ_{CRL}	σ_{CRD}	σ_U	λ_D	σ_{ND}	λ_{LD}	σ_{NLD}	σ_{NLD}/σ_U
b_f=78mm, b_s=30mm, t=2.8mm	100	800	D	250	736	656	249	0.62	247	0.58	247	0.99
				350			345	0.73	324	0.66	324	0.94
				550			508	0.92	442	0.77	442	0.87
	105	800	D	250	680	641	249	0.62	246	0.60	246	0.99
				350			344	0.74	322	0.69	322	0.94
				550			503	0.93	438	0.80	429	0.85
	110	800	D	250	630	625	248	0.63	246	0.62	246	0.99
				350			344	0.75	320	0.71	320	0.93
				550			499	0.94	434	0.83	416	0.83
	115	800	D	250	581	611	248	0.64	245	0.65	245	0.99
				350			342	0.76	318	0.74	318	0.93
				550			493	0.95	430	0.86	403	0.82
	120	800	D	250	538	596	248	0.65	244	0.67	244	0.98
				350			341	0.77	316	0.77	316	0.93
				550			489	0.96	426	0.89	391	0.80

Table 3(c). Comparison Between the “Exact” and DSM (σ_{NLD}) Ultimate Strength Estimates (STC3)

					FEA			DSM				
	b_f	L	Imp.	f_y	σ_{CRL}	σ_{CRD}	σ_U	λ_D	σ_{ND}	λ_{LD}	σ_{NLD}	σ_{NLD}/σ_U
b_w=100 mm, b_f=100 mm, t=2 mm	22	950	D	250	317	285	226	0.94	197	0.79	195	0.86
				350			262	1.11	241	0.87	224	0.85
				550			276	1.39	308	0.99	265	0.96
	24	950	D	250	317	299	227	0.92	201	0.80	198	0.87
				350			270	1.08	246	0.88	227	0.84
				550			287	1.36	315	1.00	268	0.94
	26	950	D	250	317	314	230	0.89	205	0.80	200	0.87
				350			279	1.06	251	0.89	230	0.83
				550			300	1.32	323	1.01	273	0.91
	28	950	D	250	316	331	232	0.87	208	0.81	202	0.87
				350			288	1.03	257	0.90	233	0.81
				550			316	1.29	331	1.02	277	0.88
	30	950	D	250	315	350	234	0.85	212	0.82	205	0.88
				350			297	1.00	263	0.91	237	0.80
				550			337	1.25	339	1.04	281	0.83

Table 4(a). Comparison Between the "Exact" and DSM (σ_{NDL}) Ultimate Strength Estimates (STC1)

					FEA			DSM				
	b_f	L	Imp.	f_y	σ_{CRL}	σ_{CRD}	σ_U	λ_L	σ_{NL}	λ_{DL}	σ_{NDL}	σ_{NDL}/σ_U
b_w=180mm, b_s=20mm, t=3.4mm	90	650	D	250	361	399	240	0.83	239	0.77	215	0.89
				350			298	0.98	301	0.87	251	0.84
				550			361	1.23	406	1.01	302	0.84
	95	650	D	250	358	377	231	0.84	239	0.80	211	0.91
				350			287	0.99	300	0.89	245	0.85
				550			341	1.24	405	1.04	295	0.86
	100	650	D	250	355	355	222	0.84	238	0.82	206	0.93
				350			276	0.99	299	0.92	240	0.87
				550			323	1.24	404	1.07	287	0.89
	105	650	D	250	353	338	217	0.84	238	0.84	203	0.93
				350			267	1.00	298	0.94	235	0.88
				550			307	1.25	403	1.09	281	0.91
	110	650	D	250	350	320	211	0.84	237	0.86	199	0.94
				350			256	1.00	298	0.96	230	0.90
				550			292	1.25	402	1.12	274	0.94

Table 4(b). Comparison Between the "Exact" and DSM (σ_{NDL}) Ultimate Strength Estimates (STC2)

					FEA			DSM				
	b_w	L	Imp.	f_y	σ_{CRL}	σ_{CRD}	σ_U	λ_L	σ_{NL}	λ_{DL}	σ_{NDL}	σ_{NDL}/σ_U
b_f=78mm, b_s=30mm, t=2.8mm	100	800	D	250	736	656	249	0.58	250	0.62	247	0.99
				350			345	0.69	350	0.73	324	0.94
				550			508	0.86	514	0.88	423	0.83
	105	800	D	250	680	641	249	0.61	250	0.62	246	0.99
				350			344	0.72	350	0.74	322	0.94
				550			503	0.90	501	0.88	412	0.82
	110	800	D	250	630	625	248	0.63	250	0.63	246	0.99
				350			344	0.75	350	0.75	320	0.93
				550			499	0.93	489	0.88	402	0.81
	115	800	D	250	581	611	248	0.66	250	0.64	245	0.99
				350			342	0.78	350	0.76	318	0.93
				550			493	0.97	476	0.88	392	0.80
	120	800	D	250	538	596	248	0.68	250	0.65	244	0.98
				350			341	0.81	342	0.76	311	0.91
				550			489	1.01	464	0.88	383	0.78

Table 4(c). Comparison Between the "Exact" and DSM (σ_{NDL}) Ultimate Strength Estimates (STC3)

					FEA			DSM				
	b_s	L	Imp.	f_y	σ_{CRL}	σ_{CRD}	σ_U	λ_L	σ_{NL}	λ_{DL}	σ_{NDL}	σ_{NDL}/σ_U
b_w=100 mm, b_f=100 mm, t=2 mm	22	950	D	250	317	285	226	0.89	230	0.90	187	0.83
				350			262	1.05	288	1.00	215	0.82
				550			276	1.32	388	1.17	256	0.93
	24	950	D	250	317	299	227	0.89	230	0.88	190	0.84
				350			270	1.05	288	0.98	219	0.81
				550			287	1.32	388	1.14	261	0.91
	26	950	D	250	317	314	230	0.89	229	0.85	193	0.84
				350			279	1.05	288	0.96	223	0.80
				550			300	1.32	388	1.11	267	0.89
	28	950	D	250	316	331	232	0.89	229	0.83	197	0.85
				350			288	1.05	288	0.93	228	0.79
				550			316	1.32	388	1.08	273	0.86
	30	950	D	250	315	350	234	0.89	229	0.81	200	0.86
				350			297	1.05	287	0.91	232	0.78
				550			337	1.32	387	1.05	279	0.83

(iii) While in the slender columns with narrow flanges (first plot) a f_y increase leads to a σ_{NLD}/σ_U drop (*i.e.*, to safer but less accurate estimates), precisely the opposite behaviour is exhibited by the slender columns with moderate-to-wide flanges (second and third plots): a higher f_y leads to a σ_{NLD}/σ_U increase (i.e., to more unsafe results). Thus, the DSM estimate accuracy always drops as f_y increases.

(iii) While in the slender columns with narrow flanges (first plot) a f_y increase leads to a σ_{NLD}/σ_U drop (*i.e.*, to safer but less accurate estimates), precisely the opposite behaviour is exhibited by the slender columns with moderate-to-wide flanges (second and third plots): a higher f_y leads to a σ_{NLD}/σ_U increase (*i.e.*, to more unsafe results). Therefore, it seems logical to assume that the DSM estimate accuracy always drops as the yield stress f_y increases.

(iv) The stocky column σ_{NLD} estimates are always safe in all the three plots – unlike in the slender columns, an increase of the b_f/b_w ratio does not lead to unsafe estimates.

(v) In stocky columns with moderate flanges (second plot), a f_y increase leads to a σ_{NLD}/σ_U drop (*i.e.*, to safer but less accurate results). Conversely, in stocky columns with narrow or wide flanges (first and third plots), there is no visible tendency, as far as the influence of f_y on the safety level of the σ_{NLD} estimates is concerned.

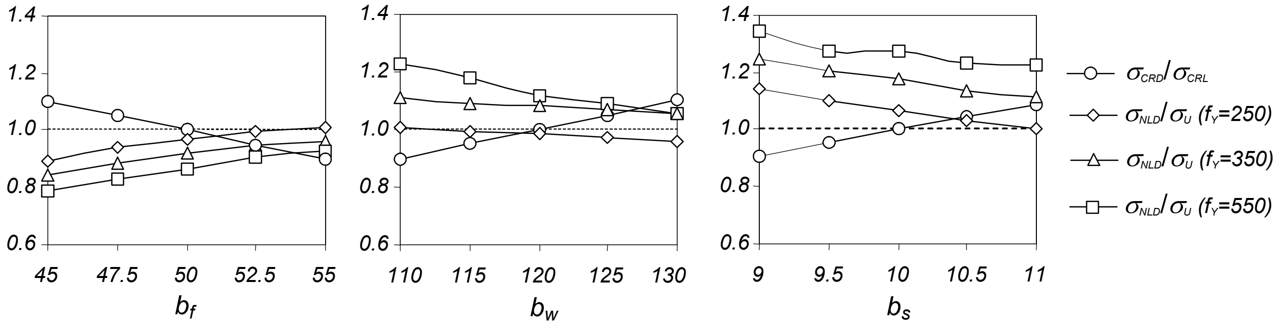

Figure 9. Slender Columns: Variation of $\sigma_{CRD}/\sigma_{CRL}$ and σ_{NLD}/σ_U Ratios with the Cross-Section Dimensions

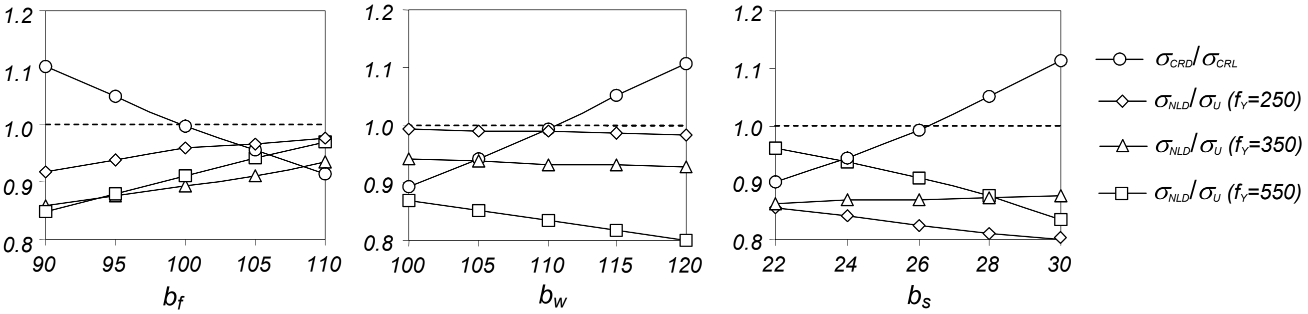

Figure 10. Stocky Columns: Variation of $\sigma_{CRD}/\sigma_{CRL}$ and σ_{NLD}/σ_U Ratios with the Cross-Section Dimensions

Figures. 11(a)-(b) show the variation of σ_{NLD}/σ_U with (i) the flange-to-web width ratio b_f/b_w ratio and (ii) the yield stress f_y (f_y=*250, 350, 550 MPa*). These plots provide the following information:

(i) For the slender columns, it is clear that an increase in b_f/b_w always leads to an increase in the value of the stress ratio σ_{NLD}/σ_U. Moreover, the σ_{NLD} estimates are (i_1) mostly safe for columns with narrow flanges ($b_f/b_w<0.6$) and (i_2) mostly unsafe for columns with moderate-to-wide flanges ($b_f/b_w>0.6$).

(ii) For the stocky columns, a b_f/b_w increase does not cause a similar increase in the stress ratio σ_{NLD}/σ_U.

(iii) In slender columns, a f_y increase leads to a spreading of the σ_{NLD}/σ_U values around (above and below) 1.0 – see Figure. 11(b). In stocky columns, on the other hand, a higher yield stress does not alter significantly the scatter of the σ_{NLD}/σ_U vaules.

(iv) In columns with moderate-to-wide flanges, the LPM is triggered by the flange (not the web) instability. Since the DM is always caused by the flange-stiffener/lip instability, the flange local-plate deformations will certainly have a deteriorating effect on the column distortional post-buckling behaviour.

(v) Whenever the yield stress f_y is much higher than the σ_{CRD} and σ_{CRL} values (this is the case in the slender columns with moderate-to-wide flanges and $f_y=550MPa$), there is lots of "room" for the local-plate/distortional mode interaction to develop before the applied stresses reach their ultimate value σ_U. This feature will certainly have a weakening impact on the ultimate strength of the columns affected by LP/D mode interaction.

Finally, Figure. 12 shows the variation of the σ_U/f_y (white dots) and σ_{NLD}/f_y (black dots) stress ratios with the columns *distortional slenderness* $\lambda_D=(f_y/\sigma_{CRD})^{0.5}$, for the three yield stress values. Also included are the two DSM "Winter-type" curves providing the *local-plate* and *distortional* column ultimate strengths, which were defined in Eqs. 3 and 4. The joint observation of all these results prompts the following comments:

(i) The proposed DSM predictions (σ_{NLD}) concerning the *slender* columns ($\lambda_D>1.4$) always lie well below both the local-plate and distortional DSM curves. On the other hand, these same predictions for the *stocky* columns ($\lambda_D<1.4$) are always located near the distortional DSM curve. This means that, at least for the critical stress ratio range considered ($0.90 \leq \sigma_{CRD}/\sigma_{CRL} \leq 1.10$), the local-plate/distortional interaction always causes a substantial strength erosion in the *slender* columns (with respect to the values associated with the individual local-plate and distortional collapses).

(ii) Unlike the σ_{NLD} estimates, which always remain quite "aligned" (*i.e.*, define a single curve), the "exact" ultimate strengths exhibit a "vertical dispersion" that grows with f_y. This trait indicates that, as f_y increases, the column σ_U values become "more dependent" on the value of the slenderness λ_D.

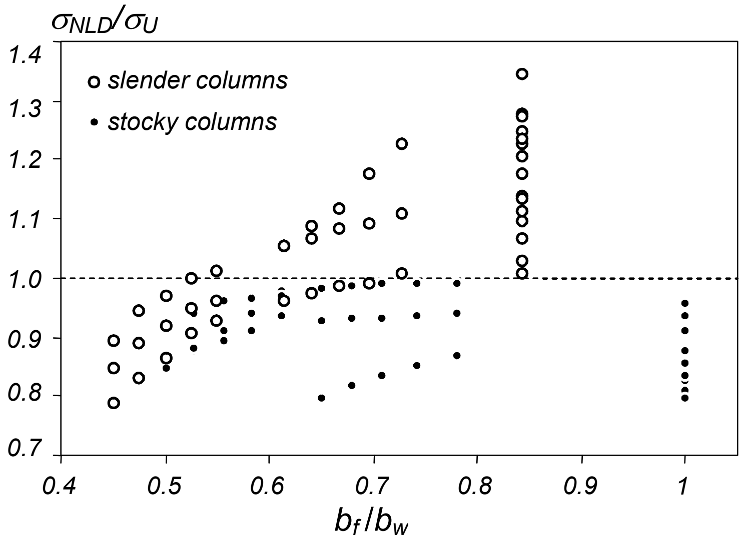

(a)

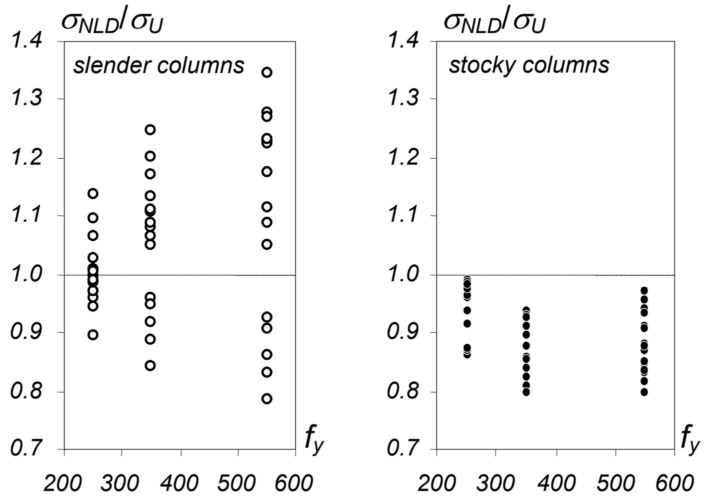

(b)

Figure 11. Variation of the Stress Ration σ_{NLD}/σ_U with (a) b_f/b_w and (b) f_y

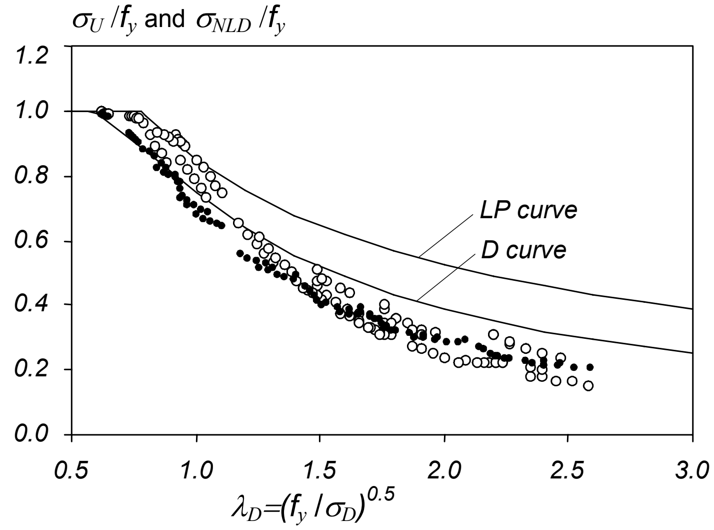

Figure 12. Variation of σ_{NLD}/f_y and σ_U/f_y with the Distortional Slenderness λ_D, Plus the LP and D DSM Curves

5. CONCLUSION

The results of an ongoing investigation concerning the use of a DSM (Direct Strength Method) approach to estimate the ultimate strength of lipped channel columns affected by local-plate/distortional mode interaction were reported. The columns analysed (a total of *111*) were all simply supported and had either low-to-moderate ($0.6 \leq \lambda_D \leq 1.4$ – *stocky* columns) or moderate-to-high ($1.4 \leq \lambda_D \leq 2.6$ – *slender* columns) distortional slenderness – therefore, they covered the slenderness range inside which the individual local-plate and distortional DSM curves were experimentally and/or numerically calibrated and validated. On the basis of the ultimate load values obtained by means of a FEM-based parametric study, it was possible (i) to assess the performance of two basic DSM approaches that are based on the already well established expressions derived to estimate the ultimate strengths of columns failing in individual ("pure") local-plate and distortional modes, and also (ii) to identify a number of features that must be included in a more elaborate DSM approach, specifically developed to take into account the local-plate/distortional buckling mode interaction phenomenon.

Concerning the use of the two basic DSM approaches (*NDL* and *NLD*) to predict the ultimate strength (σ_U) of columns experiencing strong local-plate/distortional mode interaction (the local-plate and distortional critical stresses, σ_{CRL} and σ_{CRD}, are never more than *10%* apart), it was possible to conclude that:

(i) In columns with low-to-moderate distortional slenderness ($\lambda_D \leq 1.4$), the σ_{ND} values provide accurate estimates of their load-carrying capacities – *i.e.*, the use of the existing DSM provisions for distortional buckling yields satisfactory results.

(ii) For moderate-to-high column distortional slenderness ($1.4 \leq \lambda_D \leq 2.6$), the σ_{NLD} values provide reasonably accurate ultimate strength estimates – in particular, the "quality" of these estimates is slightly superior to that of their σ_{NDL} counterparts. However, it was noticed that the σ_{NLD} values consistently overestimated the σ_U ones in the columns exhibiting wide flanges and high yield stresses.

(iii) Nevertheless, it is fair to say that, at least for the simply supported columns dealt with in this study, the σ_{NLD} values provide much better column ultimate strength predictions than the existing DSM provisions (for pure local-plate and distortional failures). Indeed, these values are mostly safe and fairly accurate, regardless of the distortional slenderness value, which confirms the assessment made by Yang and Hancock [10], on the basis of an experimental investigation involving lipped channel columns with "v-shape" web and flange intermediate stiffeners.

In spite of the fairly good performance of the *NLD* DSM approach to account for the local-plate/distortional mode interaction effects, the authors of this paper (i) are aware that further investigations are required (*e.g.*, one must analyse fixed columns and additional experimental evidence is necessary) and also (ii) feel that there is still room for improvement, particularly for the slender columns that exhibit wide flanges and high yield stresses, *i.e.*, the ones for which the σ_{NLD} predictions excessively overestimate the "exact" σ_U values. Therefore, the ultimate goal of the research effort currently under way is to develop, validate and calibrate (through the comparison with additional numerical simulations and experimental results) a direct strength approach that is able to cover adequately all columns affected by local-plate/distortional interactive buckling. Hopefully, this goal will be achieved for lipped channel columns in a not too distant future – some fixed column numerical results were very recently reported [24, 25] and an experimental test program is currently being carefully programmed.

REFERENCES

[1] Schafer, B.W. and Pekoz, T., "Direct Strength Prediction of Cold-Formed Steel Members Using Numerical Elastic Buckling Solutions", Thin-Walled Structures - Research and Development (ICTWS'98 – Singapore, 2-4/12), N. Shanmugam, J.Y.R. Liew, V. Thevendran (eds.), Elsevier, 1998, pp. 137-144.

[2] Schafer, B.W., "Direct Strength Method Design Guide", AISI – American Iron & Steel Institute, Washington DC, 2005.

[3] Schafer, B.W., "Review: The Direct Strength Method of Cold-Formed Steel Member Design", Proceedings of International Colloquium on Stability and Ductility of Steel Structures (SDSS'06 – Lisbon, 6-9/9), D. Camotim, N. Silvestre, P.B. Dinis. (eds.), IST-Press, 2006, pp. 49-66.

[4] Standards of Australia and Standards of New Zealand (SA-SNZ), Australian/New Zealand Standard on Cold-Formed Steel Structures – AS/NZ*S 4600* (Second Edition), Sydney-Wellington, 2005.

[5] American Iron and Steel Institute (AISI), Appendix I of the North American Specification (NAS) for the Design of Cold-Formed Steel Structural Members: Design of Cold-Formed Steel Structural Members with the Direct Strength Method, Washington DC, 2004.

[6] Schafer, B.W., "Progress on the Direct Strength Method", Proceedings of 16th International Specialty Conference on Cold-Formed Steel Structures (Orlando, 17-18/10), R. LaBoube, W.-W. Yu (eds.), 2002, pp. 647-662.

[7] Schafer, B.W., "Advances in the Direct Strength Design of Thin-Walled Members", Advances in Structures (ASSCCA'03 – Sydney, 23-25/6), G.J. Hancock et al. (eds.), Lisse, Balkema, 2003, pp. 333-339.

[8] Duong, H.M. and Hancock, G.J., "Recent Developments in the Direct Strength Design of Thin-Walled Members", Thin-Walled Structures: Recent Advances and Future Trends in Thin-Walled Structures Technology (Loughborough, 25/6), J. Loughlan (ed.), Bath, Canopus Publishing, 2004, pp. 43-62.

[9] Rasmussen, K.J. and Hossain, M.S., "Design of Slender Angle Section Beam-Columns by the Direct Strength Method", Proceedings of Fourth International Conference on Coupled Instabilities in Metal Structures (CIMS'04 – Rome, 27-29/9), M. Pignataro, J. Rondal, V. Gioncu (Eds.), Editura Orizonturi Universitare, Timisoara, 2004, pp. 331-344.

[10] Yang, D. and Hancock, G.J., "Compression Tests of High Strength Steel Channel Columns with Interaction between Local and Distortional Buckling", Journal of Structural Engineering (ASCE), Vol. 130, Issue 12, 2004, pp. 1954-1963.

[11] Kwon, Y.B., Kim, N.G. and Kim, B.S., "A Study on the Direct Strength Method for Compression Members Undergoing Mixed Mode Buckling", Proceedings of Third International Symposium on Steel Structures (Seoul, 10-11/3), 2005, pp. 108-119.

[12] Silvestre, N., Camotim, D. and Dinis, P.B., "On the Use of the Direct Strength Method to Design Lipped Channel Columns Affected by Local-Plate/Distortional Mode Interaction", Proceedings of 4th European Conference on Steel and Composite Structures (EUROSTEEL 2005 – Maastricht, 8-10/6), B. Hoffmeister, O. Hechler (eds.), 2005, pp. 125-133.

[13] Silvestre, N., Camotim, D. and Dinis, P.B., "DSM Design Against Local-Plate/Distortional Interactive Buckling", STEEL – A New and Traditional Material for Building (ICMS'06 – Poiana Braşov, 20-22/9), D. Dubina, V. Ungureanu (eds.), Taylor & Francis, 2006, pp. 225-233.

[14] Dinis, P.B. and Camotim, D., "Local-Plate and Distortional Post-Buckling Behavior of Cold-Formed Steel Columns: Elastic and Elastic-Plastic FEM Analysis", Proceedings of SSRC Annual Stability Conference (Long Beach, 24-27/3), 2004, pp. 475-498.

[15] Dinis, P.B.; Camotim, D., "FEM Elastic and Elastic-Plastic Analysis of the Local-Plate/Distortional Mode Interaction in Cold-Formed Steel Columns", Proceedings of Fourth International Conference on Coupled Instabilities in Metal Structures (CIMS'04 – Rome, 27-29/9), M. Pignataro, J. Rondal, V. Gioncu (eds.), Editura Orizonturi Universitare (Timisoara), 2004, pp. 477-492.

[16] Dinis, P.B., Camotim, D. and Silvestre, N., "FEM-Based Analysis of the Local-Plate/Distortional Mode Interaction in Cold-Formed Steel Lipped Channel Columns", Computers & Structures, Vol. 85, Issue 19-20, 2007, pp. 1461-1474.

[17] Hibbit, Karlsson and Sorensen Inc. (HKS), *ABAQUS Standard* (Version 6.3-1), 2002.

[18] Dinis, P.B. and Camotim, D., "On the Use of Shell Finite Element Analysis to Assess the Local Buckling and Post-Buckling Behaviour of Cold-Formed Steel Thin-Walled Members", Submitted for Publication, 2008.

[19] Schafer, B.W., "Cold-Formed Steel Design by the Direct Strength Method: Bye-Bye Effective Width", Proceedings of SSRC Annual Technical Session & Meeting (Baltimore, 2-5/4), 2003, pp. 357-377.

[20] Schafer, B.W., "Distortional Buckling of Cold-Formed Steel Columns", AISI Report, American Iron & Steel Institute, Washington DC, 2000.

[21] Schafer, B.W., "Local, Distortional and Euler Buckling in Thin-Walled Columns", Journal of Structural Engineering (ASCE), Vol. 128, Issue 3, 2002, pp. 289-299.

[22] Narayanan, S. and Mahendran, M., "Ultimate Capacity of Innovative Cold-Formed Steel Columns", Journal of Constructional Steel Research, Vol. 59, Issue 4, 2003, pp. 489-508.

[23] Ellobody, E. and Young, B., "Behavior of Cold-Formed Steel Plain Angle Columns", Journal of Structural Engineering (ASCE), Vol. 131, Issue 3, 2005, pp. 457-466.

[24] Silvestre, N., Camotim, D. and Dinis, P.B., "DSM Design of Fixed Lipped Channel Columns Against Local-Plate/Distortional Interactive Buckling", Proceedings of 6th International Conference on Steel & Aluminium Structures (ICSAS'07 – Oxford, 24-27/7), R. Beale (ed.), 2007, pp. 752-759.

[25] Silvestre, N., Dinis, P.B. and Camotim, D., "Direct Strength Design of Fixed Lipped Channel Columns Against Multiple-Wave Local/Distortional Interactive Buckling", Proceedings of 5th International Conference on Thin-Walled Structures – Recent Innovations and Developments (ICTWS 2008 – Brisbane, 18-20/6), M. Mahendran (ed.), 2008, pp. 281-288 (vol. 1).

EFFECTS OF STEEL FIBRE REINFORCEMENT ON THE BEHAVIOUR OF HEADED STUD SHEAR CONNECTORS FOR COMPOSITE STEEL-CONCRETE BEAMS

O.Mirza[1] and B.Uy [2, *]

[1] PhD Candidate, School of Engineering, University of Western Sydney, Australia
Telephone: + 612 4736 0402, Fax: +612 4736 0137, Email: o.mirza@uws.edu.au
[2] Professor and Head of School of Engineering, University of Western Sydney, Australia
Telephone: + 612 4736 0228, Fax: +612 4736 0137
**(Corresponding author: Email: b.uy@uws.edu.au)*
Locked Bag 1797 Penrith South DC, NSW 1797, Australia

Received: 31 October 2007; Revised: 10 January 2008; Accepted: 16 January 2008

ABSTRACT: Composite steel-concrete beams are becoming increasingly popular in multistorey buildings due to their higher span/depth ratio, reduced deflections and increased stiffness value. However, their performance is highly dependent on the load-slip characteristics of the shear connectors. More recently, trapezoidal profiled slabs are becoming increasingly more popular for high rise buildings when compared with solid slabs because they can achieve large spans with little or no propping and they require less concrete and plywood formwork. However, the profiles used to achieve these savings can have a detrimental effect on the shear connector behaviour. This paper describes a nonlinear finite element model developed using ABAQUS to study the behaviour of shear connectors in both solid and profiled steel sheeting slabs. In addition to analysing the influence of the shear connectors on the structural performance, steel fibres are introduced to further augment the ductility and strength of the shear connection region in the slab. The results obtained from the finite element analyses were verified against experimental results and indicate that the strength and load-slip behaviour are significantly influenced by the inclusion of steel fibres.

Keywords: Composite steel-concrete beams; steel fibres; finite element analysis

---

1. INTRODUCTION

Martin [1] stated that currently, composite structures have been commonly used in construction in order to save time in construction and subsequently reduce structural costs. Composite beam designs are greatly affected by the behaviour of the shear connection. The main factors affecting shear connection are the strength of the shear connectors and the strength of the concrete that surrounds the shear connectors. In the 1960's, composite beams used welded wire fabric (WWF) as secondary reinforcement for temperature and shrinkage in the concrete. The apparent problems that arose were the correct positioning of the WWF and the cost of labour and time. One improvement to the existing concept is with the application of steel fibres. Steel fibres are preferred to steel reinforcement/mesh because they reduce dead loads; subsequently they reduce the load transferred to the foundations and at the same time improve the moment capacity, fire resistance and control cracking.

A three dimensional finite element model has been developed by Lam and El-Lobody [2] to simulate the behaviour of shear connectors in composite steel-concrete beams for solid slabs. The finite element results compared well with the experimental results and all the modes of failure were accurately predicted by the finite element model. Kim et al. [3] studied the behaviour of shear connection for composite steel and concrete beams using experimental studies and the results were compared using a two dimensional finite element analysis using the LUSAS finite element programme. The authors concluded that the inclusion of profiled steel sheeting led to an increase in strength and the finite element result and experimental results were in good agreement. Furthermore the authors also showed that the behaviour of shear connection in composite steel-concrete beams is greatly influenced by the loading and boundary conditions. More advanced finite element analysis was performed by El-Lobody and Young [4] to describe the structural performance of shear connectors in composite steel-concrete beams with profiled slabs. A three dimensional nonlinear finite element analysis was used to compare the experimental results and it was concluded that the capacity of shear connection, load-slip behaviour and failure modes predicted were in good correlation with the experimental results.

Previously, experimental push tests have been used to evaluate the shear connector capacity, and in this paper the load versus slip relationship of the connectors was compared against a three dimensional finite element model developed using a finite element software package known as ABAQUS. The main objectives of this paper are to develop a three dimensional finite element model to simulate the shear connector behaviour for both solid and profiled slabs with the addition of steel fibres into the concrete slab for the push test and to determine the advantages related to the finite element analysis of push tests.

2. ADVANTAGES OF FIBRES TO SHEAR CONNECTOR BEHAVIOUR AND STRENGTH

Lam and Nip [5] performed horizontal push off tests on six composite beams. The parameters considered were transverse reinforcement and steel fibres. The push off specimens consisted of four 600 mm wide hollow core units connected to a 254 x 254 x 73 universal column with six 19 mm diameter x 100 mm height pre-welded headed shear studs at 150 mm centres. Four 1100 mm long transverse bars were placed in the opened cores and in-situ concrete was placed and compacted in the central gap.

Lam and Nip's experiments showed that by adding 2 % of steel fibres, both the compressive and flexural strength increased by 25 and 20 %, respectively. Shear stud failure occurred where transverse bars of T16 specification were used. Concrete with steel fibres were observed to have a higher ultimate load than their counterparts. Meanwhile, there was greater slip ductility where the increment was up to 75 % and the shear capacity was at 16 % increment.

Craig et al. [6] compared the behaviour of composite steel-concrete beams using steel fibres and conventional reinforcement. The authors established that the composite steel-concrete with steel fibres could sustain higher loads than plain concrete. When steel fibre reinforcement was added to the concrete, the concrete exhibited improved confinement and better bond. Moreover, steel fibres also enhanced the rotational and moment capacity.

The combination of steel fibres with a composite slab not only increases structural stiffness and ductility, they also provide slabs with a fire rating ranging from 60 to 90 minutes. Two aspects are to be considered when steel fibre reinforced concrete is used in composite beams; shear stud resistance and ductility and the ability of steel fibre reinforced concrete to resist transverse shear in the slabs adjacent to the shear studs, Robery [7].

Roberts-Wollmann et al. [8] used steel fibres to replace welded wire fabric (WWF) as secondary reinforcement and verified that both deflection and cracks decreased in composite beams. They also demonstrated that it was preferable to use steel fibres rather than synthetic fibres. A slab reinforced with 29.6 kg/m^3 of steel fibres had a higher ultimate strength (18 %) than a slab reinforced with WWF. Using steel fibres also resulted in a higher ultimate capacity. The researchers also showed that the composite beam reinforced with 0.9 kg/m^3 of synthetic fibres failed at a load equivalent to the WWF.

3. EXPERIMENTAL INVESTIGATION

3.1 Description of Push Test Specimens

Two types of experimental investigations were considered for comparison with the finite element models developed in this paper. They include Becher [9] for solid slabs and Wu [10] for profiled slabs. All experimental tests were based on Eurocode 4, British Standards Institution [11] where a push test specimen consists of a steel beam connected to two concrete slabs, either a solid slab or profiled slab through shear connectors. The concrete slabs were embedded in mortar or gypsum onto the test bed and a uniformly distributed load was applied onto the upper end of the web of the steel beam. However, some compromise has been made due to time limits, equipment and budget restrictions. The modified push test, as shown in Figures 1 and 2 involve a standard push test as described with a roller support at one end to eliminate any horizontal resistance being imposed on the slab. The slab dimensions were 600 mm x 600 mm x 120 mm; 50 mm shorter and 30 mm thinner than that suggested by Eurocode 4, British Standards Institution [11]. In order to provide identical lateral and longitudinal reinforcement strength, 4 x 4 reinforcing mesh bar was used as a substitute for 5 x 4 reinforcing mesh which was outlined in Eurocode 4, British Standards Institution [11]. The steel beam used was a 200UB25. Each specimen was initially loaded to 40 % of the expected failure load then cycled 25 times between 5 % and 40 % of the expected failure load. Finally, each specimen was loaded until failure occurred.

Twelve push tests were carried out to determine the load-slip behaviour of the shear connectors for both the solid slab and profiled slab configurations. Three specimens of different steel fibre reinforcement concentrations with two push tests each were tested, as illustrated in Table 1.

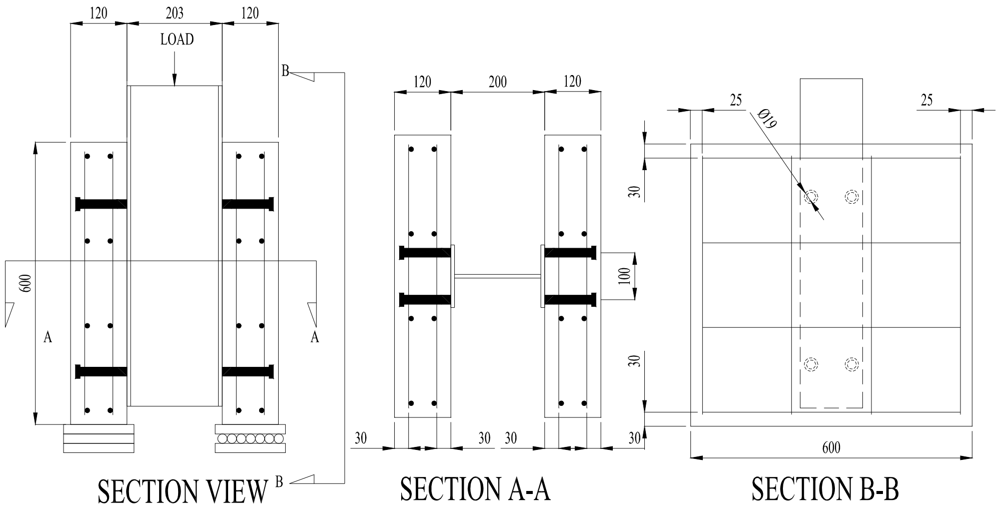

4 x 4 reinforcing mesh are provided in both ways with 10 mm diameter reinforcing bars with 180 mm spacing.

Figure 1. Details of Push Test Specimen for Solid Slab

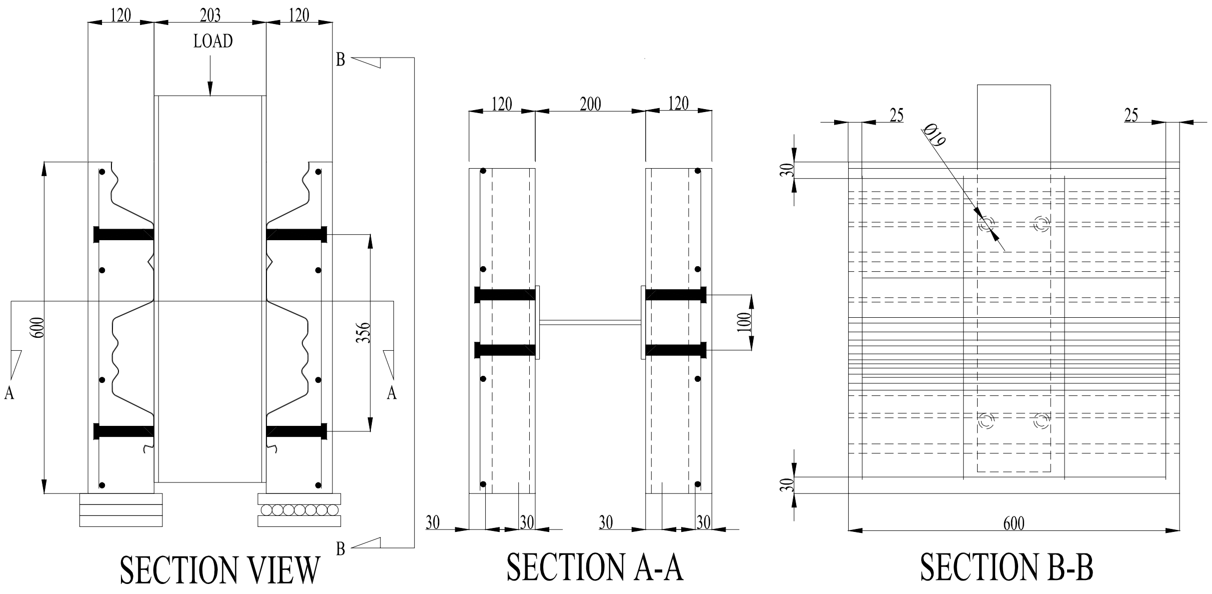

4 x 4 reinforcing mesh are provided in both ways with 10 mm diameter reinforcing bars with 180 mm spacing.

Figure 2. Details of Push Test Specimen for Profiled Slab

Table 1. Beam parameters

Test No.	Slab Profile	Percentage of steel fibres
1	Solid slab	0.0
2	Solid slab	0.3
3	Solid slab	0.6
4	Lysaght W-Dek Profiled slab	0.0
5	Lysaght W-Dek Profiled slab	0.3
6	Lysaght W-Dek Profiled slab	0.6

4. FINITE ELEMENT MODEL

4.1 General

The finite element program ABAQUS, Karlsson and Sonrensen [12], [13] and [14] was used to quantify the behaviour of the shear connection in composite beams. The main components affecting the behaviour of the shear connection in composite beams were the concrete slab, steel beam, profiled steel sheeting, reinforcing bars and shear connectors. These components must be carefully modelled to obtain an accurate result from the finite element analysis. A three dimensional finite element model has been developed to simulate the geometric and material nonlinear behaviour of composite beams. The accuracy of the analysis is heavily dependent on the constitutive laws used to define the mechanical behaviour.

4.2 Concrete

4.2.1 Plain concrete

To model the nonlinear behaviour of the concrete slab, plain concrete was recommended by Carreira and Chu [15], where the stress in compression is linear up to a stress of $0.4f'_c$. Beyond this point, it is in the plastic region. The ratio of biaxial compressive stress and uniaxial compressive stress based on Liang et al. [16] was taken to be 1.16 for the analysis.

$$\sigma_c = \frac{f'_c \gamma(\varepsilon_c / \varepsilon'_c)}{\gamma - 1 + (\varepsilon_c / \varepsilon'_c)^{\gamma}} \tag{1}$$

where σ_c is the compressive stress in the concrete in N/mm^2, ε_c is the strain of the concrete, ε'_c is the strain corresponding to $f_c^{'}$ and usually is taken to be 0.002, $f_c^{'}$ is defined as the cylinder compressive strength of concrete , where $\gamma = \left|\frac{f'_c}{32.4}\right|^3 + 1.55$

For the concrete in tension, the tensile stress is assumed to increase linearly with tensile strain until the concrete cracks. After the concrete cracks, the tensile stresses decrease linearly to zero. The value of strain at zero stress is usually taken as 10 times the strain at failure which is illustrated in Figure 3.

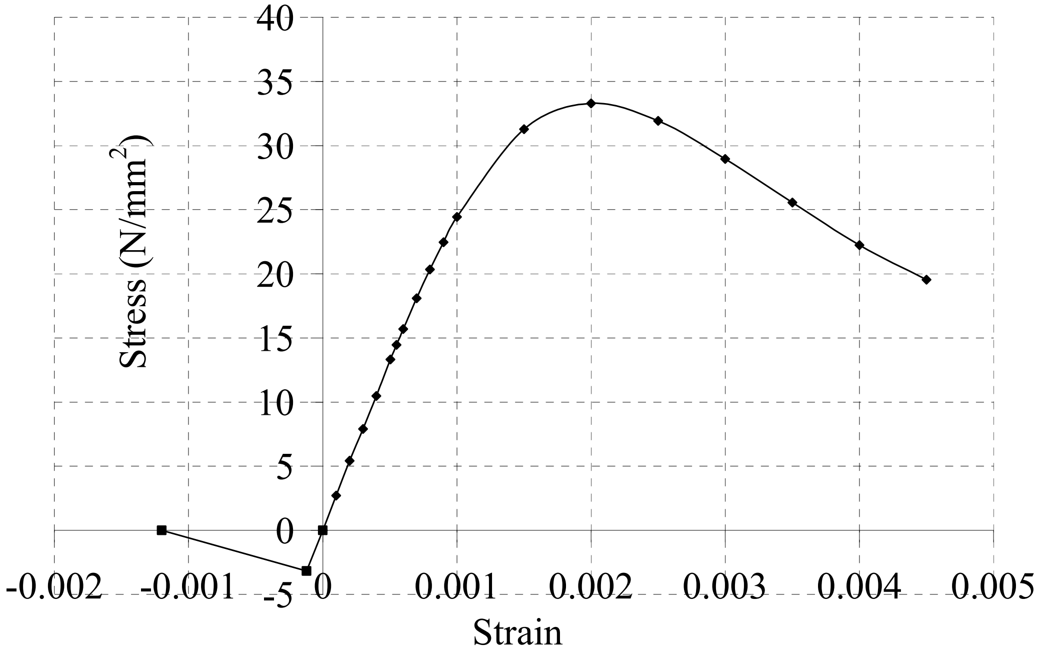

Figure 3. Stress-strain Relationship for Plain Concrete, Carreira and Chu [15]

4.2.2 Concrete with steel fibres

According to Lok and Xiao [17], even though concrete is weak in tension and lacks the necessary toughness and ductility, once it is reinforced, its mechanical properties will be altered. For concrete with steel fibres, Lok and Xiao [17] described the stress-strain relationship as:

$$\sigma = f_c\left[2\left(\frac{\varepsilon}{\varepsilon_{co}}\right)-\left(\frac{\varepsilon}{\varepsilon_{co}}\right)^2\right] \Rightarrow, \varepsilon \leq \varepsilon \tag{2}$$

$$\sigma = f_c \Rightarrow (\varepsilon_0 \leq \varepsilon \leq \varepsilon_{cu}) \tag{3}$$

where f_c is the compressive strength taken from the compressive cylinder strength test and usually is defined as $0.85f'_c$, the strain ε_{co} is defined as the strain value at the yield stress, ε is the concrete strain value and ε_{cu} is the ultimate compressive strain and a conservative value for fibre reinforced concrete of 0.003 was used. However, improved values suggested by different researchers which include Swamy and Al-Ta'an [18] recommended the value to be 0.0035 for a 1 % steel fibre concentration.

Hassoun and Sahebjam [19] recommended a value of 0.004 for 1 to 3 % of fibre concentration and Lok and Xiao [17] suggested that the recommended value be 0.0038 for 0.5 to 2 % of steel fibres. For the purposes of the finite element analysis, the authors have used the values suggested by Lok and Xiao [17].

For concrete in tension, Lok and Xiao [17] expressed the stress-strain relationship as:

$$\sigma = f_t\left[2\left(\frac{\varepsilon}{\varepsilon_{co}}\right)-\left(\frac{\varepsilon}{\varepsilon_{co}}\right)^2\right] \Rightarrow, 0 \leq \varepsilon \leq \varepsilon_{co} \tag{4}$$

$$\sigma = f_t\left[1-\left(1-\frac{f_{tu}}{f_t}\right)\left(\frac{\varepsilon-\varepsilon_{t0}}{\varepsilon_{t1}-\varepsilon_{t0}}\right)\right] \Rightarrow, \varepsilon_{t0} \leq \varepsilon \leq \varepsilon_{t1} \tag{5}$$

$$\sigma = f_{tu} \Rightarrow, \varepsilon_{t1} \leq \varepsilon \leq \varepsilon_{tu} \tag{6}$$

where f_t is defined as the ultimate tensile strength which can be determined through a direct tensile test, ε_{t0} is defined as the ultimate strain, f_{tu} is known as the residual strength and is defined as $\eta V_f \tau_d \frac{L}{d}$ by Lok and Xiao [20], ε_{t1}= $\tau_d \frac{L}{d}\frac{1}{E_s}$, V_f = the fibre volume fraction, τ_d = the bond stress, $\frac{L}{d}$ = the fibre aspect ratio, E_s = the elastic modulus of steel fibres, η = the fibre orientation in three dimensional random distribution. Hannant [21] suggested that $\eta = 0.5$, and Lok and Xiao [17] suggested that the value of $\eta = 0.405$, which is used in this paper. The stress-strain relationship of concrete with steel fibre reinforcement is shown in Figure 4. This model is adopted in the analysis due to details that are provided to distinguish the softening behaviour as a result of strain hardening of the steel fibre reinforced concrete. The predicted strengths using the derived expressions were compared with the experimental data, and good agreement was evident. In order to avoid significant error in the prediction, limitations in the material properties and the amount of steel fibres are provided.

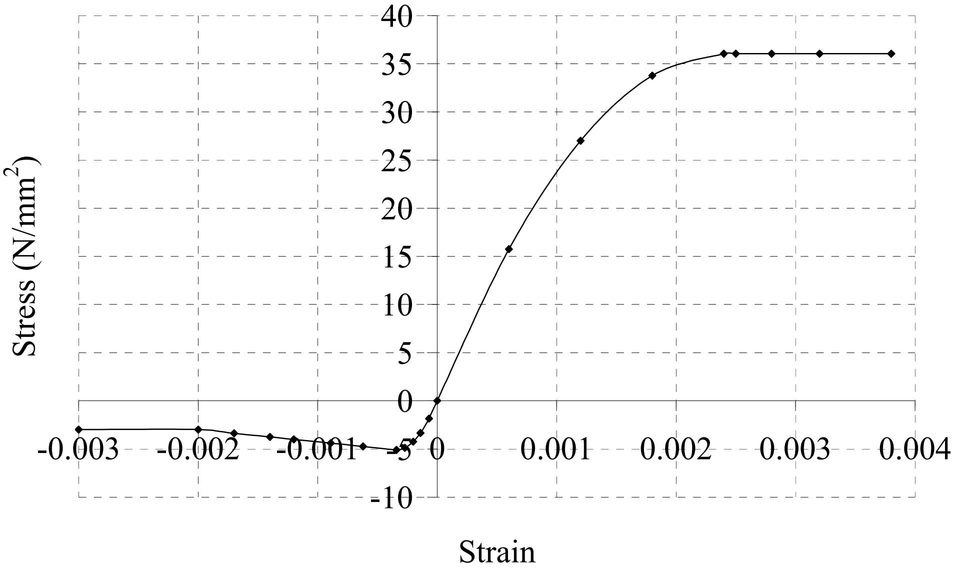

Figure 4. Stress-strain Relationship for Concrete with Steel Fibres, Lok and Xiao [17]

4.3 Structural Steel Beam, Profiled Steel Sheeting and Steel Reinforcing

According to Loh et al. [22], the stress-strain relationship for structural steel and profiled steel sheeting is modelled in a piecewise linear fashion as an elastic-plastic material with strain hardening which proved to be sufficiently accurate. The mechanical behaviour for both compression and tension is assumed to be similar. Even though the steel reinforcing mainly transfers large tensile forces, a bilinear model represents the stress-strain relationship adequately. The model according to Loh et al. [22] is shown in Figure 5, and Table 2 indicates the different values of stress and strain for different materials.

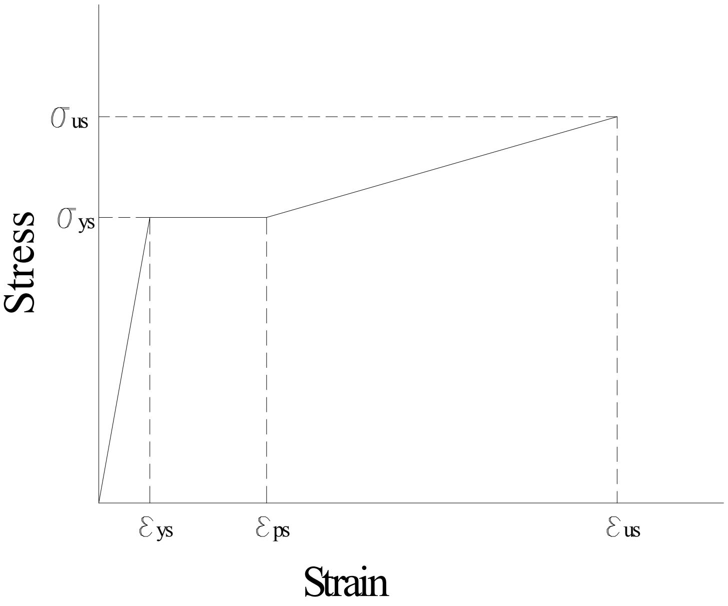

Figure 5. Stress-strain Relationship for Structural Steel Beam, Profiled Steel Sheeting and Steel Reinforcing Loh et al. [22]

Table 2. Stress-strain value for structural steel beam, shear connectors, profiled steel sheeting and steel reinforcing

Element	σ_{us}	ε_{ps}	ε_{us}
Steel beam	$1.28\sigma_{ys}$	$10\varepsilon_{ys}$	$30\varepsilon_{ys}$
Steel Reinforcing	$1.28\sigma_{ys}$	$9\varepsilon_{ys}$	$40\varepsilon_{ys}$
Profiled Sheeting	-	$20\varepsilon_{ys}$	-
Shear Connectors	-	$25\varepsilon_{ys}$	-

4.4 Shear Connectors

The most common type of shear connector used in composite construction is the 19 mm diameter headed shear stud. These connectors provide the composite action between the concrete slab and the steel beam, and are not only responsible for transferring shear forces at the slab-steel beam interface, but also prevent vertical separation at the interface. Many researchers have generated various non-linear curves using the approach of Aribert and Labib [23].

$$F_j = F_{\max}(1 - e^{-\beta s})^{\alpha} \tag{7}$$

Aribert and Labib [23] provided a combination of α = 0.8, β = 0.7 mm^{-1},while Johnson and Molenstra [24] presented values of α = 0.558, β = 1.0 mm^{-1}, and also α = 0.989, β = 1.535 mm^{-1}. An improvement was given by Gattesco and Giuriani [25] to simulate the actual behaviour of the connectors from Eq. (8) in order to represent the connector load-slip characteristics, with α = 0.97, β = 1.3 mm^{-1} and γ = 0.0045 mm^{-1}. Moreover, Loh et al. [22] proved that Eqs. (7) and (8) compared well with the experimental data obtained, as shown in Figure 6. From Figure 6, the mechanical properties of shear studs are modelled as a bilinear stress-strain model similar to Figure 5 excluding the strain hardening range.

$$F_j = P_{\max}\left[\alpha(1 - e^{\frac{-\beta s}{\alpha}})^{0.5} + \gamma s\right] \tag{8}$$

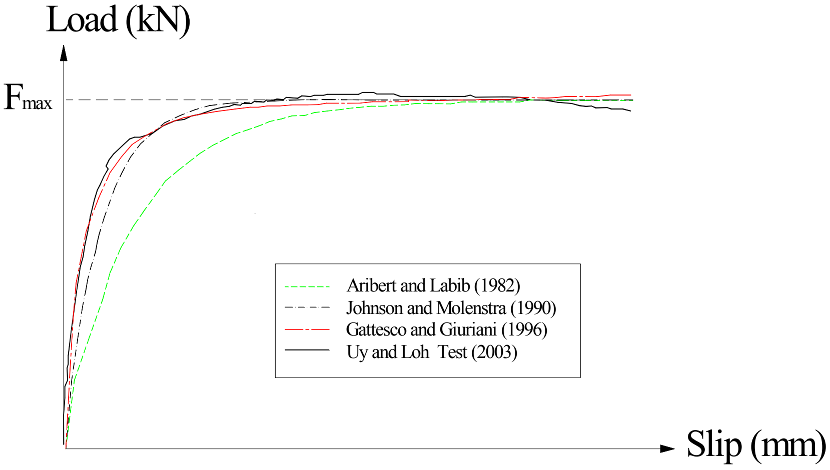

Figure 6. Load-Slip Relationship for Shear Studs Loh et al. [22]

4.5 Finite Element Mesh, Boundary Conditions and Load Application

4.5.1 Finite element mesh

Three dimensional solid elements were used to model the push off test specimens. These included a three dimensional eight node element (C3D8R) for both the concrete slab and the structural steel beam, a three dimensional thirty node quadratic brick element (C3D20R) for the shear connectors, a four node doubly curved thin shell element (S4R) for profiled steel sheeting and a two node linear three dimensional truss element (T3D2) for the steel reinforcing. In this paper, two different analyses were considered. Figures 7 and 8 show the finite element mesh used to represent half a model of the push test to reduce the simulation cost.

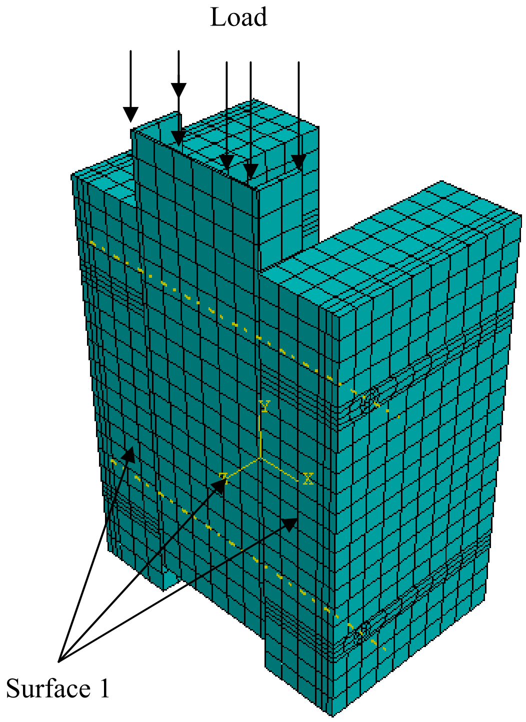

Figure 7. Finite Element Model of Push Test Specimen for Solid Slab

4.5.2 Boundary conditions and loading conditions

Surface 1 consists of the concrete slab nodes, steel reinforcing nodes and profiled steel sheeting nodes. They are restricted from moving in the Z-direction due to symmetry. The reinforcement was embedded into the concrete element using an embedded constraint type. The profiled surface was tied to the concrete surface by using the constraint enforcement method. Since the shear connectors were welded to the steel, the tie constraint method was used between the shear connectors and structural steel beam.

With the load application, a uniformly distributed load is applied to the web using the modified RIKS method. The modified RIKS method is commonly used to predict the unstable and nonlinear collapse of a structure. More importantly, this method can obtain a series of iterations for each increment for the nonlinear behaviour of structures.

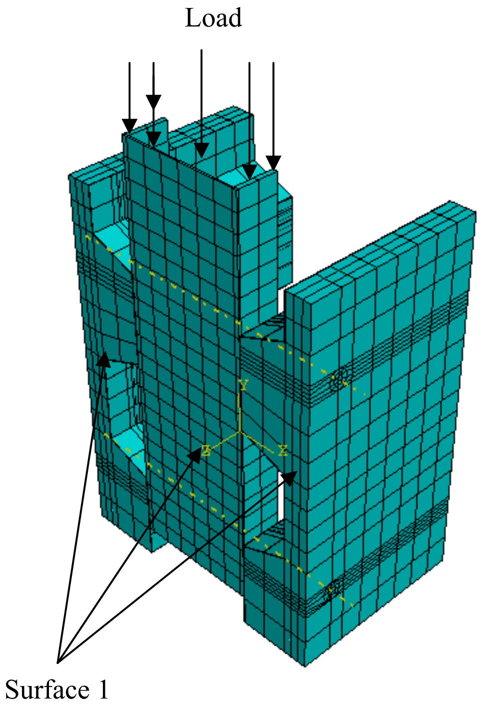

Figure 8. Finite Element Model of Push Test Specimen for Profiled Slab

5. FINITE ELEMENT ANALYSIS AND DISCUSSION

5.1 General

In order to determine the effect of steel fibres on the composite steel-concrete beams, push tests were carried out to verify the load-slip and shear capacity behaviour. Six specimens of different steel fibre quantities and slab profiles were tested to validate the present finite element model shown in Table 1. Table 3 summarised the ultimate load of the six tests compared with the finite element analysis. Table 3 verifies that the optimum dosage of steel fibres is F=0.3 because an increment of F=0.6 showed that no visible advantage is gained in concrete strength or ductility for this range of concrete strength. The ultimate load discrepancy is in good agreement with the experimental results. Generally, it can be observed that the ultimate load for solid slabs is higher than profiled slabs.

Table 3. Comparison of Experimental Results and Finite Element Analysis

Test No	Concrete strength (N/mm^2)	Exp. result (kN)	FEM result (kN)	Result Discrepancy (Exp. /FEM)	Failure Mode (*)
1	31.7	104.8	110.0	0.95	S.F
2	34.9	118.3	125.1	0.95	S.F
3	30.6	106.4	112.8	0.94	S.F and C.F
4	33.9	49.9	52.4	0.95	C.F
5	36.8	51.2	54.6	0.94	S.F
6	33.3	47.5	53.7	0.88	S.F and C.F
Mean value				0.94	

*S.F denotes stud failure and C.F concrete failure

5.2 Solid Slab

The solid push tests showed that no cracks were found on the concrete slab until the ultimate load was reached. Cracks were only observed surrounding the stud after the solid slab failed. All the three tests for the solid slab illustrated that the dominant failure mode was stud fracture where the shear connectors sheared off near the weld collar. The failure mode of the shear connectors is similar to that mentioned by Yam [26] and Lam and El-Lobody [2]. Figures 9, 10 and 11 illustrate that the shear connectors experienced significant deformation around their base. In the experiments, yielding of the stud elements was discerned near the shear connector collar followed by the maximum compressive stress being reached by the concrete elements around the shear connector. It was observed that cracking is lower when the fibre content of F=0.3 was added to the concrete. In the finite element model, the failure mode was determined where the shear connector reached the maximum stress value before the other element reached their maximum stress. The maximum stress value reached when the shear connectors reached the ultimate load and shear off the concrete element. For solid slabs, the failure modes were governed by fractured of shear connectors. The stress contour showed a higher stress value before failure occurred with the increased fibre content which is shown in Figure 12. In Figure 13, additions of steel fibres provided a higher stiffness and ductility. One important observation was that the deformation decreased with the increase in fibre content. There is an optimum value for steel fibre content in concrete. From Table 3, it is illustrated that when the value F=0.6, the concrete strength is lower than F=0.3. The reason for that is due to the fact that when the fibre content is too high in the concrete, the fibres themselves become too congested in the concrete mix. Therefore, in this study, the optimum value for fibre content is assumed to be F=0.3. Furthermore in experimental studies, for fibre content of F=0.6 not only was stud fracture observed but concrete failure crushing also occurred.

5.3 Profiled Slab

The profiled slab exhibited initial cracking in the middle of the slab along the trough of the profiled slab which was initiated by concrete failure shown in Figure 14. When steel fibres were added to the concrete, instead of concrete failure, stud failure was initiated. Therefore, it was shown that steel fibres improve the concrete strength and cracking in the surrounding concrete as shown in Figure 15. Whilst Figures 14 and 15 show that a back break type failure has occurred, this is not the primary cause and it has been exacerbated by concrete tensile and compression failure in the specimen which has then given rise to large deformations and a bending failure of the slab. Figure 16 illustrates that two types of failures occurred, these being stud and concrete failure due to clumping of the steel fibres. In the finite element model, when there is no steel fibre in the concrete, the concrete reached its ultimate stress before the shear connectors reached their maximum stress. Therefore the failure mode was concrete failure as observed in the experimental study. When $F=0.3$ steel fibres were added into the concrete, the shear connector reached the maximum stress value before the concrete reached its cracking stress. For $F=0.6,$ the failure modes were governed by both fractured of shear connectors and concrete failure. In the finite element model, it was observed that the concrete reached the maximum stress before the shear connectors. Figure 17 shows the concrete element in the trough of the profiled slab reaches a maximum stress before the shear connector element attains its maximum value. Profiled slabs indicated that the failure mode was dominated by concrete failure where the concrete cracked before the shear connectors sheared off near the weld collar with the exception of when $F=0.3$ steel fibres was added into the concrete. The failure mode observed is similar to that mentioned by El-Lobody and Young [4]. It was observed that the profiled slab experienced lower deformation and lower stress in the concrete and shear connector because of the contribution of the profiled steel Lysaght W-Dek sheeting. It was observed that cracking through the trough was lower when the fibre content was F=0.3, which proved that the steel fibres increased the stiffness and ductility of the concrete. Figure 18 shows that a higher fibre content produced a higher stiffness and ductility. The optimal amount of fibres was found to be F=0.3.

Figure 9. Concrete Damage at the Base of the Shear Connectors for Concrete with *F=0* fibres

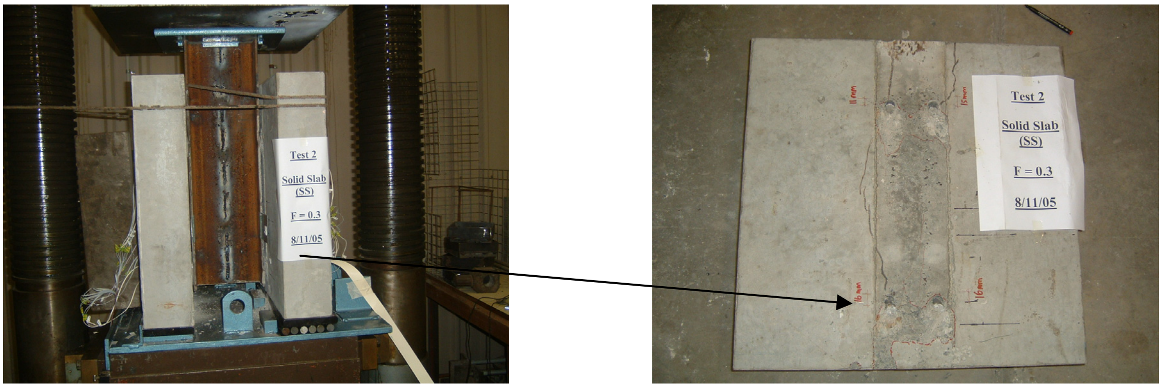

Figure 10. Concrete Damage at the Base of the Shear Connectors for Concrete With *F=0.3* Fibres

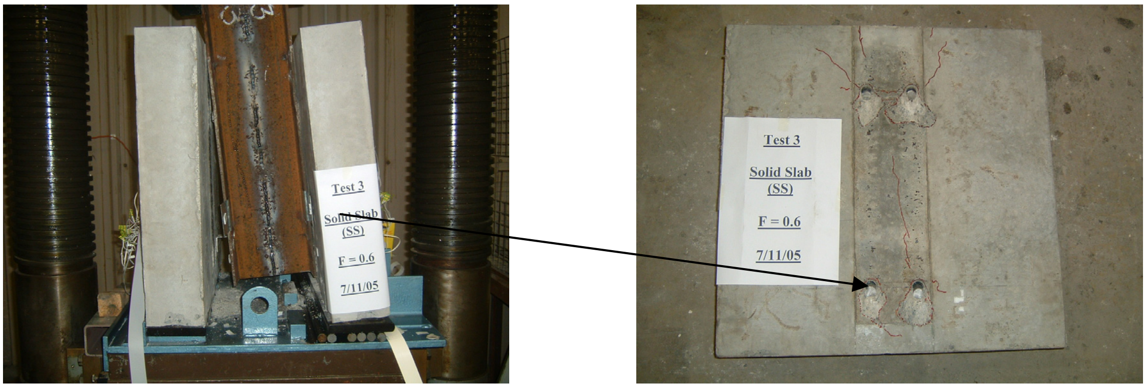

Figure 11. Concrete Damage at the Base of the Shear Connectors for Concrete With *F=0.6* Fibres

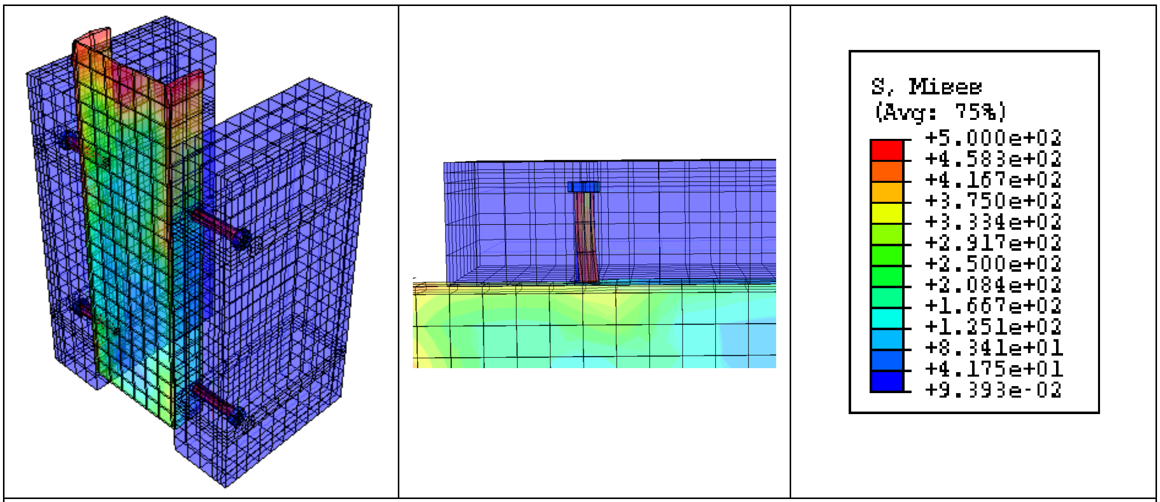

Fibre Content *F = 0*

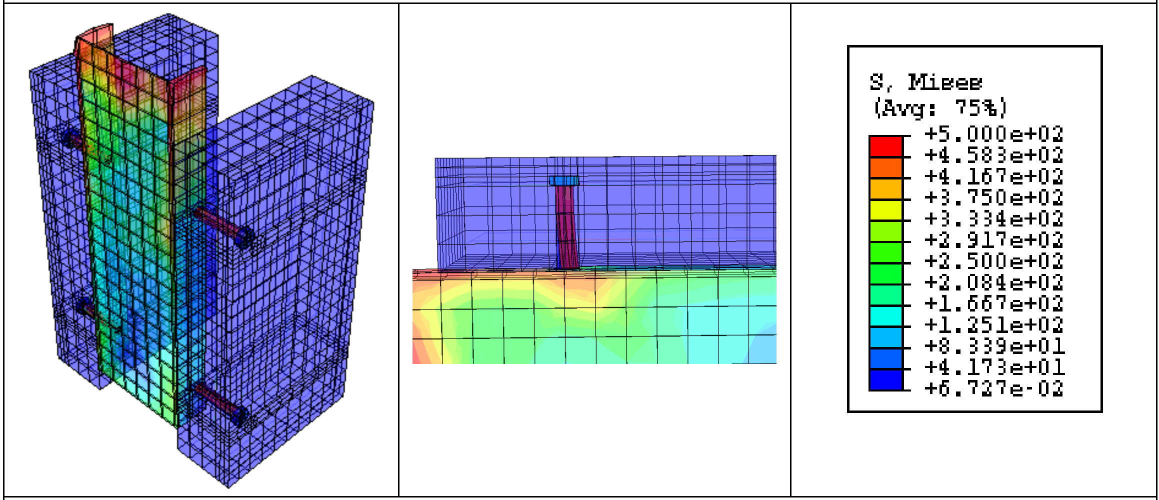

Fibre Content *F = 0.3*

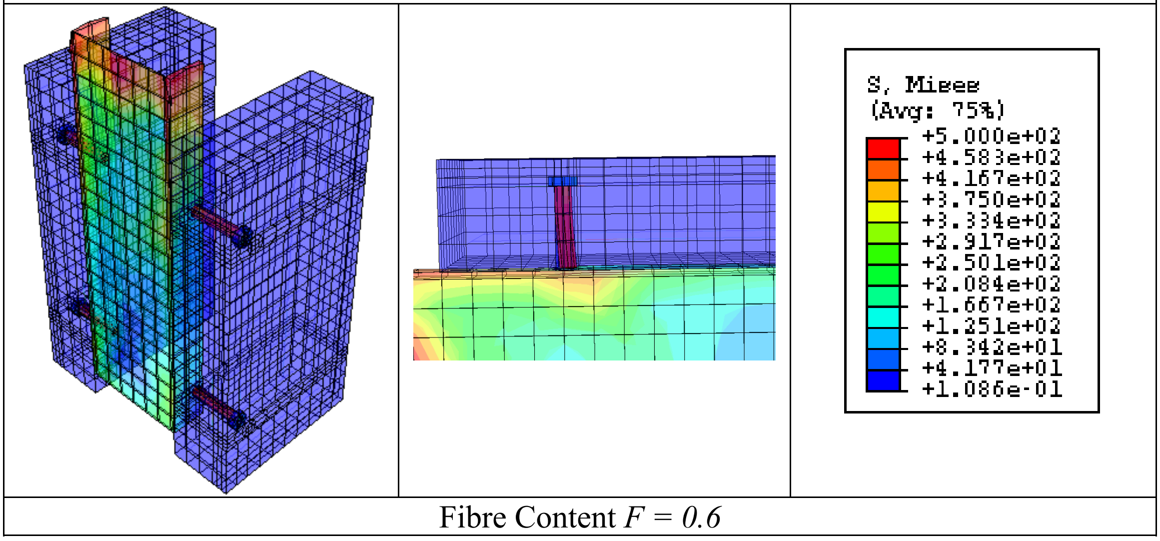

Fibre Content *F = 0.6*

Figure 12. Stress Contours and Deformed Shapes for
One Stud of Push Tests for Different Fibre Contents for Solid Slab

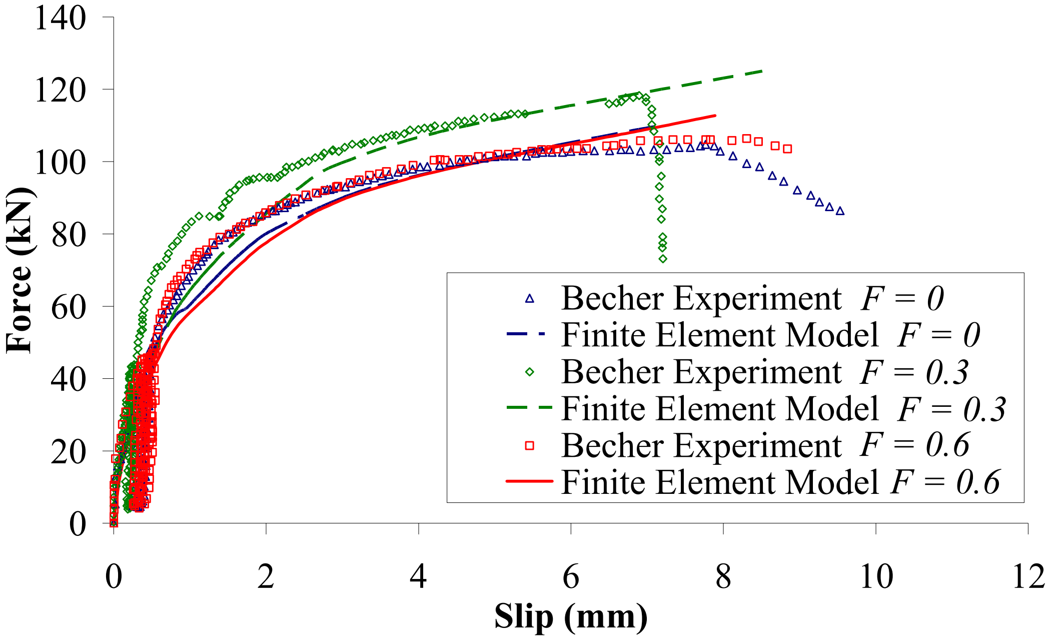

Figure 13. Comparison of Load Versus Slip Relationships with Different Fibre Contents for Solid Slabs

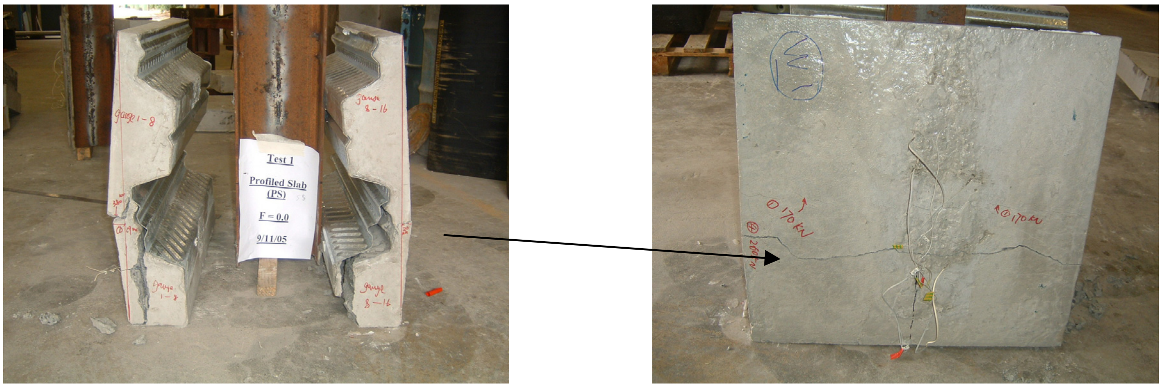

Figure 14. Concrete Damage at the Thin Layer of Concrete with *F=0* Fibres

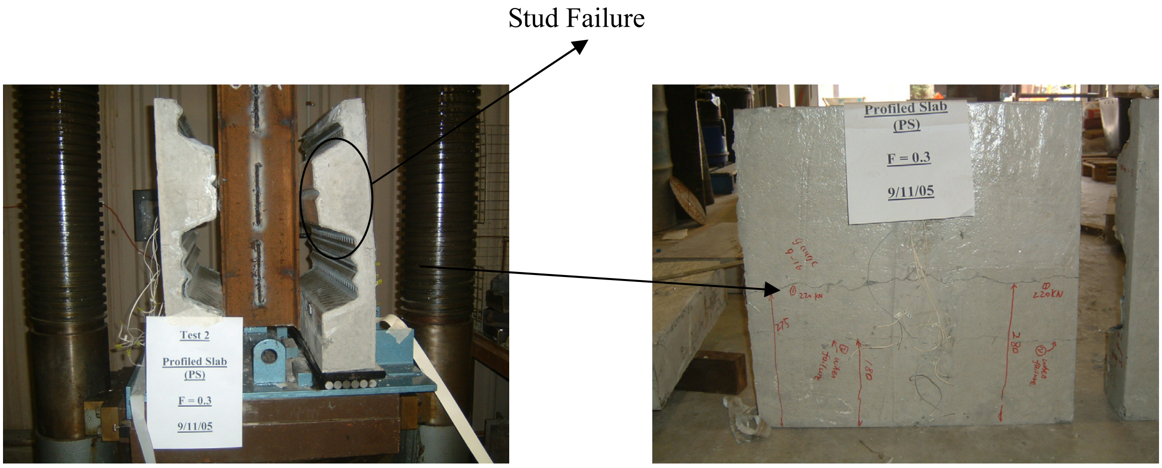

Figure 15. Stud Failure for Concrete with *F=0.3* Fibres

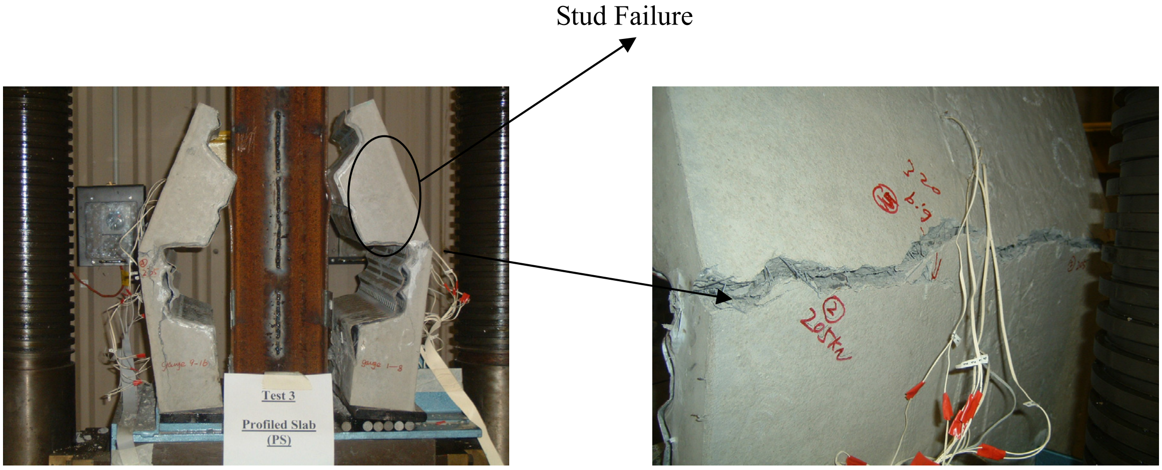

Figure 16. Stud Failure and Concrete Failure for Concrete with *F=0.6* Fibres

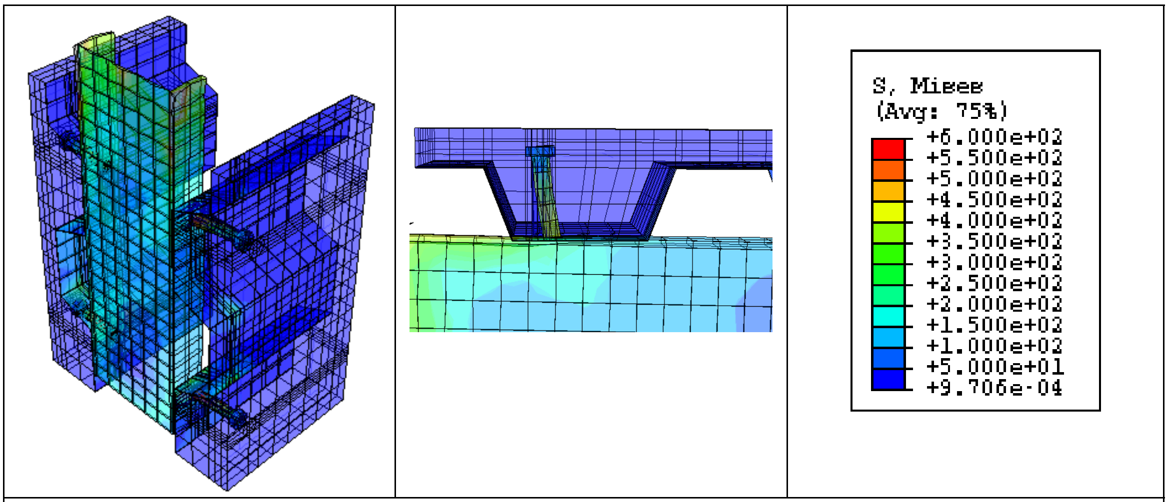

Fibre Content *F = 0*

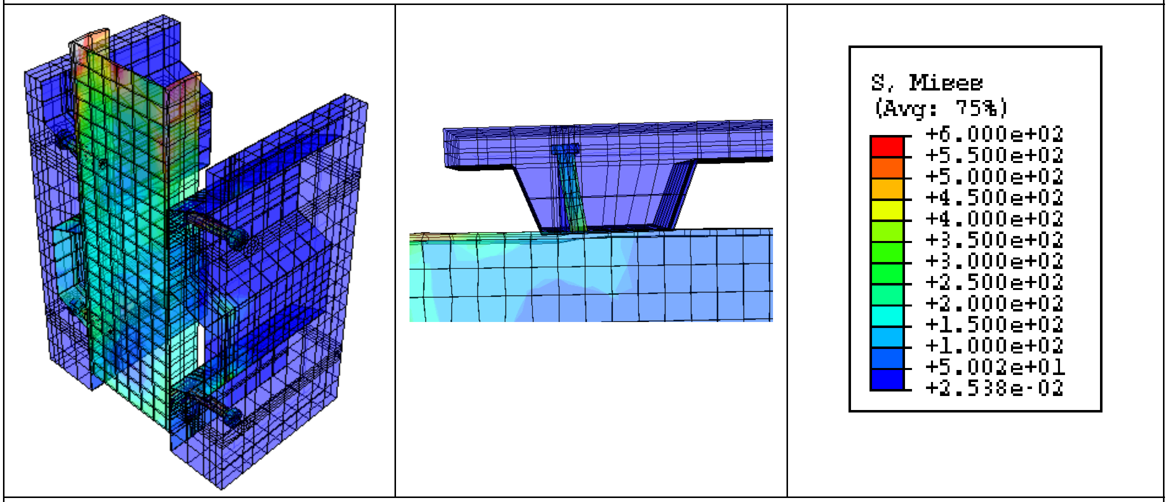

Fibre Content *F = 0.3*

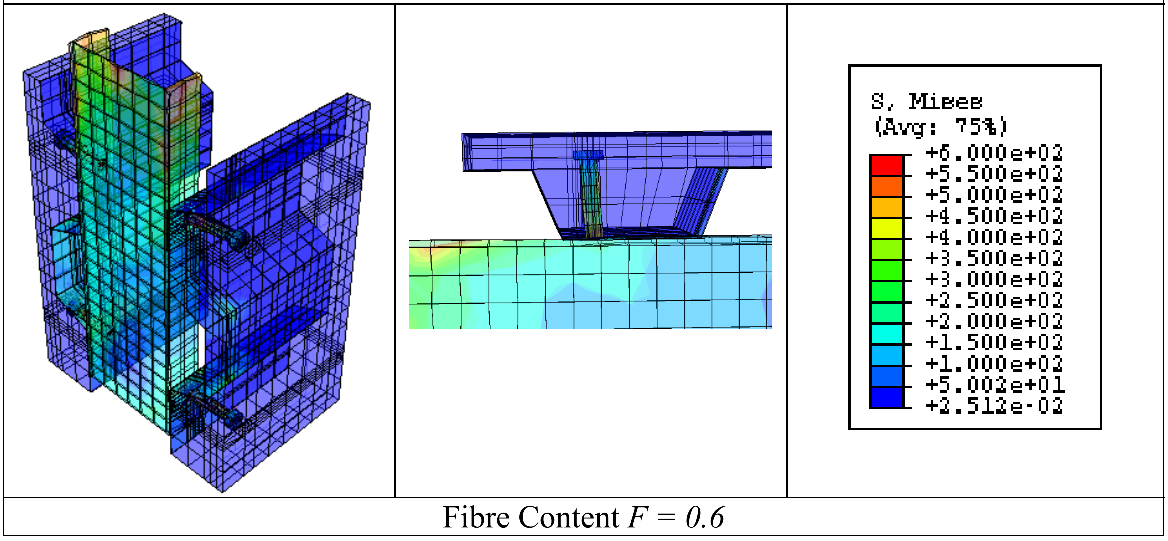

Fibre Content *F = 0.6*

Figure 17. Stress Contours and Deformed Shapes for
One Stud of Push Tests for Different Fibre Contents for Profiled Slab

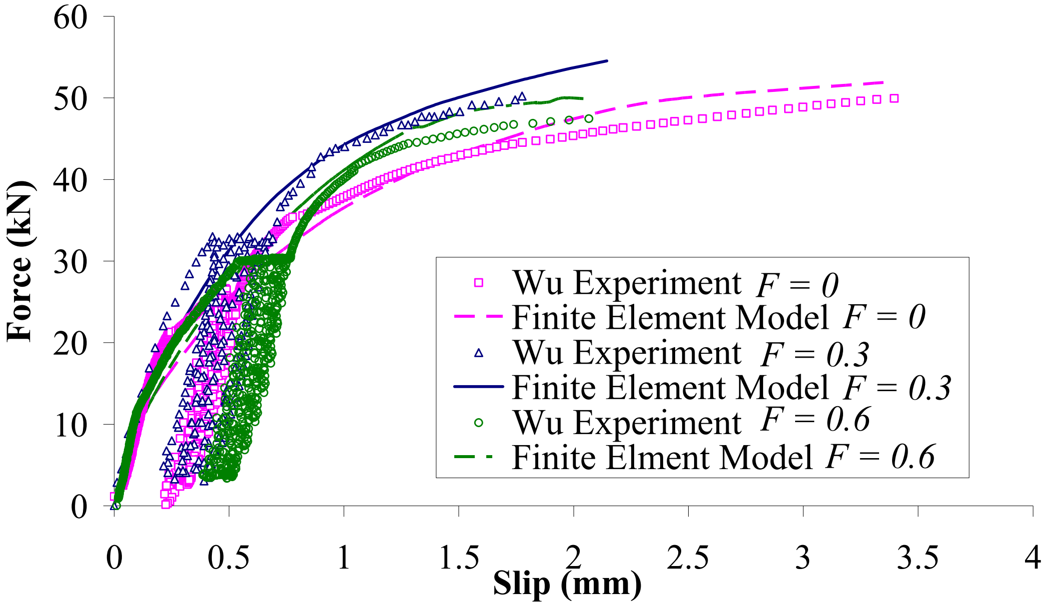

Figure 18. Comparison of Load Versus Slip Relationships with Different Fibre Contents for Profiled Slabs

5.4 Positioning of Shear Connectors in the Profiled Slab

Finite element studies have been undertaken in order to look at the effect of shear connectors placed in different positions in the profiled slab. The different positions of the shear connectors are illustrated in Figure 19.

In the initial finite element analysis, the shear connectors were placed in the perceived strong position. They are similar to the experimental tests undertaken by Wu [10]. When there were no steel fibres added to the concrete, the load-deflection behaviour of the push test shows that the failure load was 52 kN. In the weak position of the finite element models, the failure load decreased to 41 kN, which is equivalent to a reduction of about 22 % in the strength of the shear connectors. The finite element model demonstrates that the concrete element surrounding the shear connectors starts to fail. When load is applied to the middle position of the profiled slab, the specimen also did not reach the strength attained by the shear connectors that were placed in the strong region. The shear connectors' strength reduced to a value of 46 kN, which is a 11 % reduction. The results are shown in Figure 20 and it can also be observed that the shear connectors in the strong position are more ductile than the other two positions. For the strong and middle positions of the shear connectors, their stiffness is similar. Conversely, the stiffness in the weak position is lower than the other two positions.

When steel fibres with a quantity *F*=0.3 were added to the concrete, the shear connectors in the strong position attained an ultimate load of 55 kN. In the weak position of the finite element models, the load applied decreases to 46 kN, which is a reduction of 15 % in strength. The middle position of the shear connectors shows a maximum load 50 kN, which is an 8 % reduction when compared with the strong side. This is illustrated in Figure 21. When compared with concrete without steel fibres, the reduction in strength is lower. This observation suggests that the steel fibres assist to prevent concrete from cracking.

When steel fibres *F*=0.6 were added into the concrete, the strong position had an ultimate load of 50 kN. Both weak and middle positions of the finite element models were analysed, and it was shown in Figure 22 that the load was reduced to 41 kN and 46 kN, respectively. The reductions of 18 % and 8 % in the strengths when compared with the addition of steel fibres *F*=0.3 showed that there is an optimum value at which the increase in strength in relation to the amount of steel fibres in concrete becomes minimum.

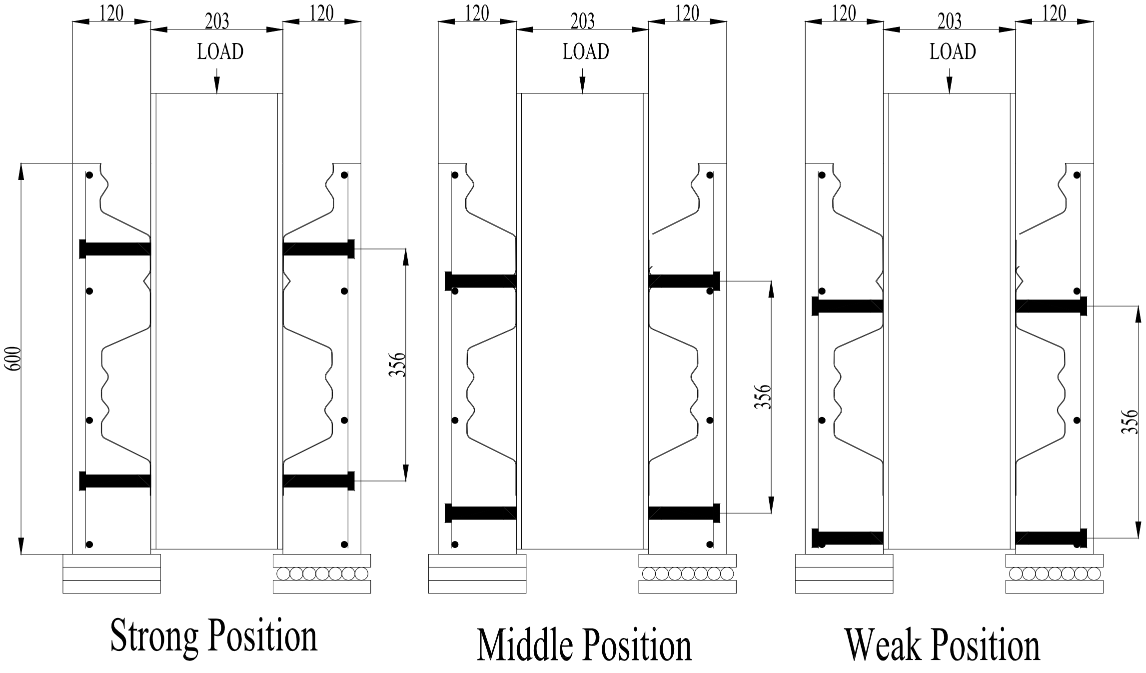

Figure 19. Position of Shear Connectors in Push Test Specimens

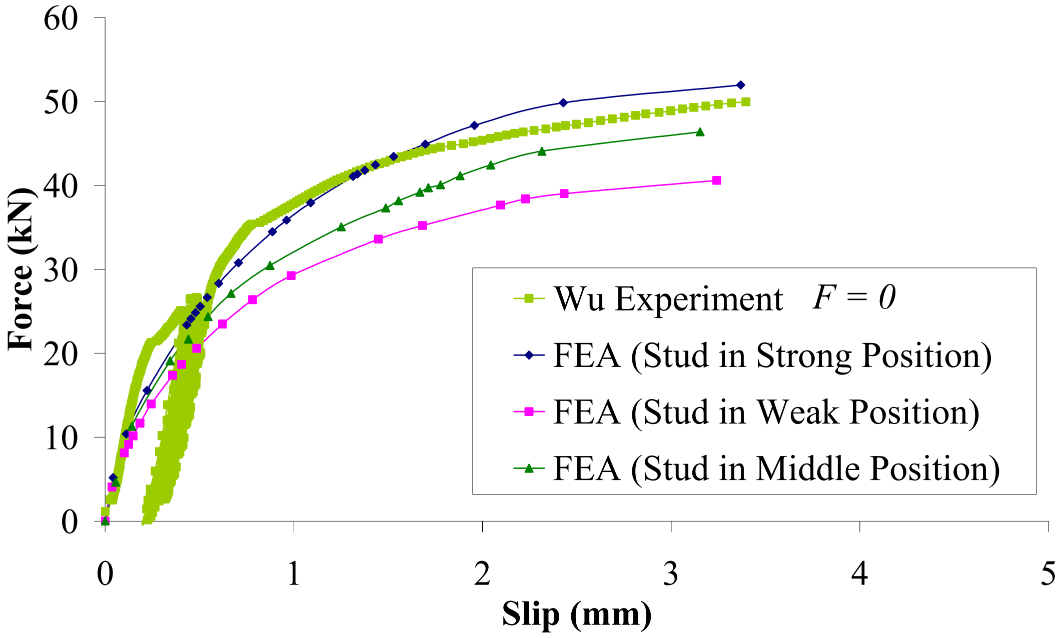

Figure 20. Load Slip Relationship for Different Shear Connectors Position Without Steel Fibres

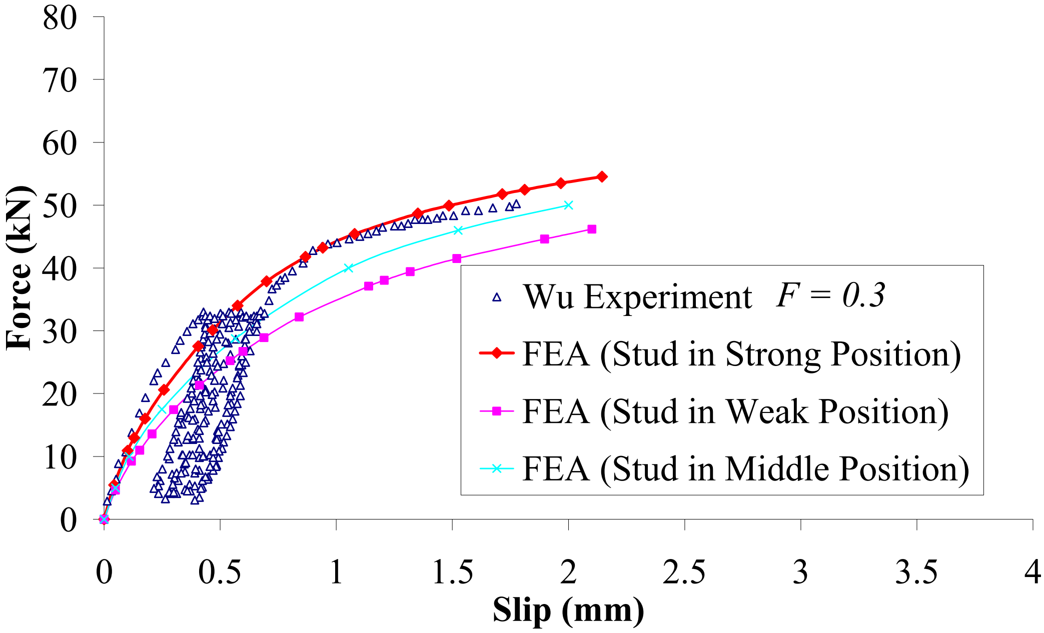

Figure 21. Load Slip Relationship for Different Shear Connectors Position with Steel Fibres *F=0.3*

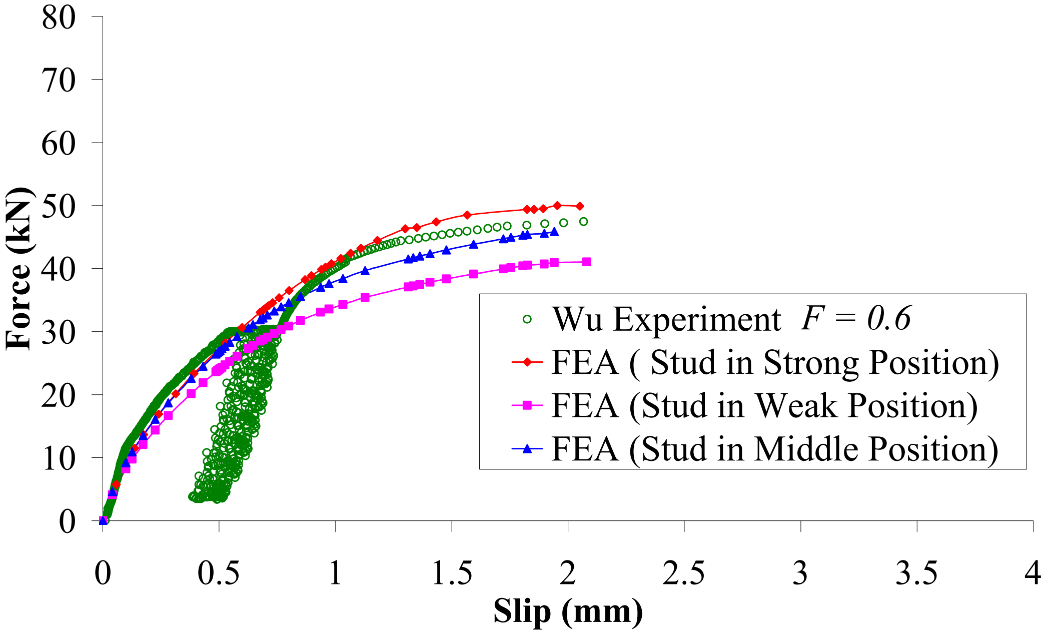

Figure 22. Load Slip Relationship for Different Shear Connectors Position with Steel Fibres *F=0.6*

6. COMPARISON OF EXPERIMENTAL STUDIES AND FINITE ELEMENT SOLUTION WITH AVAILABLE STANDARDS

A comparison was made to evaluate the experimental studies and finite element solutions with three existing international standards. They included the Australian Standard AS 2327 [27], British Standards Institute [28] and American Standard AISC [29].

The strength of the shear connector is dependent on four principal factors; E_c is the mean modulus of elasticity of the concrete, E_{sc} is the modulus of elasticity of the shear connector, f_c is the compressive strength of the concrete and f_{us} is the ultimate strength of the shear connector. The failure of a stud when steel fracture dominates is given by:

$$P_{AS} = 0.63d^2 f_{us} \tag{9a}$$

$$P_{EC} = 0.628d^2 f_{us} \tag{9b}$$

$$P_{AISC} = 0.785d^2 f_{us} \tag{9c}$$

In each equation above, the stud failure will only take place when the concrete strength is relatively high. When the concrete is weak, then Eq. 10a, b and c will tend to govern. The equations below depend greatly on f_{ck} which is the characteristic compressive cylinder strength of the concrete and E_c is defined as the mean modulus of the elasticity of concrete.

$$P_{AS} = 0.31d^2\sqrt{f_{ck}E_c} \tag{10a}$$

$$P_{EC} = 0.29d^2\sqrt{f_{ck}E_c} \tag{10b}$$

$$P_{AISC} = 0.39d^2\sqrt{f_{ck}E_c} \tag{10c}$$

When the steel profiled slab is taken into consideration, Eq. 9 and 10 above are replaced by a reduction factor k. The value of k is defined in the equations below:

$$k_{AS} = 1.148 - (0.18/\sqrt{n}) \tag{11a}$$

$$k_{EC} = \left(\frac{0.7}{\sqrt{n}}\right)\left(\frac{b_o}{h_p}\right)\left(\left(\frac{h}{h_p}\right) - 1\right) \le k_{t,\lim} \tag{11b}$$

$$k_{AISC} = \left(\frac{0.85}{\sqrt{n}}\right)\left(\frac{b_o}{h_p}\right)\left(\left(\frac{h}{h_p}\right) - 1\right) \le 1 \tag{11c}$$

where n is the number of studs, b_o is the width of the steel profiled ribs, h_p is the height of the decking profile, h is the height of the stud. A summary of the ultimate loads for the shear connector, P which is calculated using the Australian Standard, British Standard and American Standard is given in Table 4. Table 4 shows that both the experimental results and finite element solution fall between the theoretical values from the three standards.

For the solid slab, the calculated theoretical values for both the Australian and British Standards corresponded with the experimental observations. On the other hand, the American Standards seem to be less conservative because the theoretical calculations prove that the shear connectors have higher capacities when compared with the experiments. For the profiled slab, current design rules are adjusted purely based on a reduction factor k to the empirical strengths of solid slab beams. Shear connection behaviour in reality is a complex mechanism and the logic of this approach is questionable, as the theoretical calculations contradict the experimental observations shown in Table 3.

Table 4. Comparison of Ultimate Load of Shear Connector for Different Standard

Slab	F	Australian Standard		British Standard		American Standard	
		Stud	Con.	Stud	Con.	Stud	Con.
S.S	0	113.7	75.3	113.4	79.7	141.7	94.7
	0.3	130.8	86.6	130.4	91.7	162.9	108.9
	0.6	142.1	94.1	141.7	99.7	177.1	118.4
P.S	0	56.9	37.6	35.1	24.7	53.8	36.0
	0.3	65.4	43.3	40.4	28.4	61.9	41.4
	0.6	71.1	47.1	43.9	30.9	67.3	45.0

S.S denotes solid slab, P.S denotes profiled slab, Stud denotes stud failure,
Con. denotes concrete failure.

7. CONCLUSIONS

This paper discusses five key issues in the push testing of shear stud connectors. An accurate finite element model has been developed to investigate the behaviour of the shear connection in composite steel-concrete beams for both solid and profiled slabs. Based on the comparisons between the results obtained from finite element models and available experimental results, it was observed that they are in good agreement. All the failure modes were accurately predicted by the finite element model.

One primary issue that has been solved when steel fibres were included in a composite steel-concrete beam was the improved stiffness and ductility for both the solid and profiled slabs. Even though steel fibres did not show any major gain in concrete strength, the effectiveness of steel fibres is only shown when the concrete begins cracking, particularly in profiled slabs. From both the experimental tests and finite element analysis, it is illustrated that the inclusion of steel fibres in concrete improves the cracking load of the concrete. This is a major advantage especially for continuous beams in hogging moment regions. Moreover, the ultimate load of the push tests also increases with the inclusion of steel fibres for both the solid and profiled slabs.

There are three differences between the profiled steel sheeting and solid slab varieties. One of them is the failure mode. For the solid slab, the failure mode is shear connection failure whereas as for the profiled slab, failure is dominated by concrete failure as discussed in section 5. Stresses in the shear connector and concrete are lower compared with those in the solid slab, due to the addition of the steel profile. It also can be observed that the solid slab generally has a higher ultimate load compared with that of the slab with profiled steel sheeting.

The positioning of the shear connectors in composite beams has been discussed in this paper. It was concluded that both the strong and middle positions have similar stiffness, whilst the stiffness for the weak position of shear connectors is roughly 10 % lower. The ultimate loads for the shear connectors reduced by 22 % and 11 % for both the weak and middle positions, respectively. When steel fibres of F=0.3 were added to the specimens, the ultimate load was reduced by 15 % and 8 %. When compared with concrete without steel fibres, the load reduction value is less significant. On the other hand, when steel fibres with a factor of F=0.6 were added to the specimens, the ultimate strength showed reductions of 18 % and 8 % for both the weak and middle positions, respectively. As a conclusion, steel fibres are introduced to provide desirable characteristics such as increased strength and ductility in composite steel and concrete beams, but there is an optimum value for the steel fibre dosage included in the concrete.

Lastly, when the Australian, British and American Standards are compared, both experimental and finite element results seem to be in good agreement with the Australian and British Standards, however the American Standard seems to be less conservative for solid slabs. Consequently for profiled slabs this issue should be considered carefully by the designer.

Composite steel-concrete beams with the inclusion of steel fibres showed an improvement in cracking load. Studies considering continuous beams in hogging moment regions with the inclusion of steel fibres to look at the cracking behaviour and ductility will be subjected to further research in this project. Moreover, the reduction factor for the profiled slab requires augmentation for all the international standards.

LIST OF NOTATION

b_o	width of steel profiled ribs
d	diameter of shear connectors
E	elastic modulus of concrete
E_s	elastic modulus of steel fibres and shear connectors
E_c	mean modulus of elasticity of concrete
f_c	mean compressive strength of concrete
f_{ck}, f'_c	characteristic strength of compressive cylinder strength of concrete
f_t	tensile strength of concrete
f_{tu}	residual strength of concrete
f_{us}	ultimate stress of shear connectors
F	fibre content
h	height of shear connectors
h_p	height of the decking of the profiled slab
k	reduction factor for profiled slab
L/d	fibre aspect ratio
n	number of shear connectors in a shear span
P	shear capacity of shear connectors
s	longitudinal shear slip
V_f	fibre volume fraction
α, β	parameters in load-slip characteristics of shear connectors
ε_c	concrete compressive strain
ε'_c	strain corresponding to f'_c
ε_{co}	strain value at yield stress
ε_{cu}	ultimate compressive strain
ε_{ps}	strain value when strain hardening commences
ε_{us}	ultimate yield strain
ε_{ys}	yield strain
γ	parameter used for stress-strain curve for concrete
η	fibre orientation in three dimensional random distribution
σ_c	concrete compressive stress
τ_d	bond stress

SUBSCRIPTS

AS	Australian Standard
AISC	American Standard
c	concrete slab
EC	British Standard (Eurocode)
s	structural steel beam
sc	shear connection
y	yield
u	ultimate

ACKNOWLEDGEMENTS

The authors would like to thank the Australian Research Council Linkage Grant Scheme and BlueScope Lysaght, Sydney for providing funding for this project and Messrs Becher and Wu from the University of Wollongong for their assistance in the preparation of the experimental work. Furthermore the authors would like to thank the University of Western Sydney for providing a conducive environment for the authors to prepare this paper.

REFERENCES

[1] Martin, D.A., "Steel-fibre-reinforced Concrete Floors on Composite Metal Decking", Concrete (London), 2003; Vol. 37, No. 8, pp. 31-32.

[2] Lam, D. and El-Lobody, E., "Behaviour of Headed Stud Shear Connectors in Composite Beam", Journal of Structural Engineering-ASCE, 2005, Vol. 131, No. 1, pp. 96-107.

[3] Kim, B., Wright, H.D. and Cairns, R., "The Behaviour of Through-deck Welded Shear Connectors: An Experimental and Numerical Study", Journal of Constructional Steel Research, 2001, Vol. 57, No. 12, pp. 1359.

[4] El-Lobody, E. and Young, B., "Performance of Shear Connection in Composite Beams with Profiled Steel Sheeting", Journal of Constructional Steel Research, 2006, Vol. 62, No. 7, pp. 682-694.

[5] Lam, D. and Nip, T.F., "Effects of Steel Fibres Reinforcement on Shear Studs Capacity of Composite Beams", Technical Report, School of Civil Engineering, University of Leed, 2002.

[6] Craig, R.J., Mookerjee, A., Roessler, H., Jr. and Kulik, K., "Steel Reinforced Fiber Concrete Composite", Columbus, OH, USA, 1985, pp. 406-407.

[7] Robery, P., "Construction of Composite Floor Slabs Using Steel Fibre Reinforced Concrete", Structural Engineer, 2002, Vol. 80, No. 3-24, pp. 15-17.

[8] Roberts-Wollmann, C.L., Guirola, M. and Easterling, W.S., "Strength and Performance of Fiber Reinforced Concrete Composite Slabs", Journal of Structural Engineering, ASCE, 2004, Vol. 130, No. 3, pp. 520-528.

[9] Becher, L., "Behaviour and Design of Composite Beams Using Fibre Reinforced Composite Slabs", in Faculty of Engineering, 2005, University of Wollongong, Wollongong, pp. 75.

[10] Wu, J., "Behaviour and Design of Composite Beams Using Fibre Reinfroced Composite Slabs", in Faculty of Engineering, 2006, University of Wollongong, Wollongong, pp. 191.

[11] British Standards Institution, "Design of Composite Steel and Concrete Structures, Part 1.1 General Rules and Rules for Buildings, British Standard Institute, London; ENV 1994-1-1; 2004.

[12] Karlsson and Sonrensen, "Analysis User's Manual Version 6.5, Hibbitt, Pawtucket, R.I., 2006.

[13] Karlsson and Sonrensen, "User's Manual Version 6.5", Hibbitt, Pawtucket, R.I., 2006.

[14] Karlsson and Sonrensen, "Theory manual version 6.5", Hibbitt, Pawtucket, R.I., 2006.

[15] Carreira, D. and Chu, K., "Stress-strain Relationship for Plain Concrete in Compression", Journal of ACI Structural, 1985; Vol. 82, No. 11, pp. 797-804.

[16] Liang, Q., Uy, B., Bradford, M.A. and Ronagh, H.R., "Ultimate Strength of Continuous Composite Beams in Combined Bending and Shear", Journal of Constructional Steel Research, 2004, Vol. 60, pp. 1109-1128.

[17] Lok, T. and Xiao, J., "Flexural Strength Assessment of Steel Fiber Reinforced Concrete", Journal of Materials in Civil Engineering, 1999, Vol. 11, No. 3, pp. 188-196.

[18] Swamy, R.N. and Al-Ta'an, S.a., "Deformation and Ultimate Strength in Flexural of Reinfroced Concrete Beams Made with Steel Fiber Concrete," Journal of ACI Structural, 1981, Vol. 78, No. 36, pp. 395-405.

[19] Hassoun, M.N. and Sahebjam, K., "Plastic Hinge in Two-span Reinforced Concrete Beams Containing Steel Fibers", in Proceeding Canada Society of Civil Engineering, Canada, 1985, pp. 119-139.

[20] Lok, T.S. and Xiao, J.R., "Tensile Behaviour and Moment-curvature Relationship of Steel Fibre Reinforced Concrete", Magazine of Concrete Research, 1998, Vol. 50, No. 4, pp. 359-368.

[21] Hannant, D.J., "Fiber Cement and Fiber Concrete", New York, Wiley, 1978.

[22] Loh, H.Y., Uy, B. and Bradford, M.A., "The Effects of Partial Shear Connection in the Hogging Moment Region of Composite Beams Part II - Analytical Study", Journal of Constructional Steel Research, 2003, Vol. 60, pp. 921-962.

[23] Aribert, J. and Labib, A., "Modèle calcul èlasto-plastique de pustres mixtes a connexion partielle", Journal of Construct Metallique, 1982, Vol. 4, pp. 3-51.

[24] Johnson, R. and Molenstra, N., "Partial Shear Connection in Composite Beams for Building", in Proceeding Institute Civil Engineer, London, 1991, pp. 679-704.

[25] Gattesco, N. and Giuriani, E., "Experimental Study on Stud Shear Connectors Subjected to Cyclic Loading", Journal of Constructional Steel Research, 1996, Vol. 38, No. 1, pp. 1-21.

[26] Yam, L.C.P., "Design of Composite Steel-concrete Structures", London, Surrey University Press, 1981.

[27] AS 2327, A.S. Composite Structures, Part 1: Simply Supported Beams, Standard Australia International, 2003, AS 2327, pp. 1-2003.

[28] British Standards Institute, "Design of Composite Steel and Concrete Structures", Part 1.1 General Rules and Rules for Buildings, British Standard Institute, London; ENV 1994-1-1; 2004.

[29] AISC, Load and Resistance Factor Design Specification (LRFD), American Institute of Steel Construction, 1999.

THE STRUCTURAL BEHAVIOUR OF COMPOSITE CONNECTIONS WITH STEEL BEAMS AND PRECAST HOLLOW CORE SLABS

Feng Fu

Structural Engineer, WSP Group, WSP House , 70 Chancery Lane London WC2A 1AF
E-mail: cenffu@yahoo.co.uk

Received: 19 November 2007; Revised: 5 January 2008; Accepted: 16 January 2008

ABSTRACT: The use of composite precast hollowcore floor system has been rapidly increased in U.K. and the international construction market due to its various advantages. However, this composite system is mainly used as simply supported beam, without considering the moment behaviour of the connections. Therefore, little research on the composite joint behaviour of this connection has been conducted so far. In this paper, using the general purpose finite element software ABAQUS, a three dimensional model of the composite joint was set up to simulate the semi-rigid composite beam-column connections of the composite beams with precast hollowcore slabs. Using the proposed model, the numerical studies using 3-D Finite element modelling techniques were carried out. Against with the full scale test results of the author, the structural behaviour of this type of connections was studied.

Keywords: Connection; semi-rigid;, finite element; connection; modelling

---

1. INTRODUCTION

In the building construction, precast hollowcore slab is a newly developed floor system with limited research. Compared with the traditional composite floor system like the solid slabs or metal profiled decking floor system, it saves construction time; reduce the cost of concrete casting, etc. Therefore, it becomes more and more popular in the construction market. In the construction practice, the composite beams with precast slabs are used as simply supported beam; no moment capacity of the connection has been taken into account in the current design. However research by the author found that even with simple steel beam to column connection, if the longitudinal steel bars are placed around the columns edge, the connection can achieve some moment capacity due to the composite action between the precast slabs and the steel beams. The behaviour of this type of connections more or less can be classified as semi-rigid connections which can be used to enhance the whole stability of the frames. Therefore, the research on the behaviour of this type of connections is quite necessary.

Johnson et al. [1] firstly conducted five tests on composite connections which covered the whole range of the web slenderness available in universal beams and showed that negative moment with semi-rigid joints had greater resistance to bucking and much greater rotation capacity than rigid joints. MacGinley et al. [2] tested a series of bare steel joints and two composite connections. The two composite connections exhibited considerably more capacity than the bare steel joints. Davison et al. [3] tested eleven composite beam-to-columns connections. This was the first study in the U.K. to use relatively flexible joint details to exploit the composite floor action in composite frames. This also was the first attempt to use profiled metal decking rather than a solid slab. The test results suggested that it was unwise to rely solely on mesh to provide tensile reinforcement and that the anchorage of the reinforcement is particularly important. Seven bare steel beam-to-column equivalent joints were tested, the comparison between the two types of connection showed that the composite connection had significant improvement on the stiffness and strength. Anderson et al. [4] carried out research on flush and extended endplate composite connections with metal decking flooring at the University of Warwick. The tests were of a cruciform configuration with the loads being applied at the assumed point of contra-flexure of the beam. Xiao et al. [5] carried out tests on flush and partial depth end plate connections with metal decking slab at the University of Nottingham. Twelve tests were carried out on major axis connections using flush end plates of 10 mm thickness with modest amounts of slab reinforcement. A further twelve tests were carried out on fin-plate, partial depth endplate and cleated connections. The rotation capacity found from the experiment was similar to the tests carried out by Anderson et al. [4]

In addition to full scale test, finite element modelling technique is used to study the behaviour of the composite connections. Krishnamurthy et al. [6] modelled the connections by adopting the eight-node sub-parametric bricks in order to reproduce the behaviour of bolted end plate connections. Ayoub et al. [7] used the inelastic beam element for the analysis of steel–concrete composite girders with partial composite action under monotonic and cyclic loads. Sebastian et al. [8] developed a beam element with layered steel beam and layered concrete slab for the analysis of steel–concrete composite girders. In their study, they also included the modelling of profiled steel sheeting. A stub element with an empirical nonlinear shear force–slip relationship is used at the concrete slab–steel beam interface to permit the modelling of either full or partial shear connector action. Baskar et al. [9] built a 3-D FE model using ABAQUS to analyze the steel-concrete composite plate girders under negative bending and shear loading. In order to overcome the convergence problem of under the negative bending, different material models have been tried. The material model adopted is the CAST IRON MODEL and ELASTIC–PLASTIC MODEL. Ahmed et al. [10] proposed a 2-D model for the analysis of composite connections and composite frames using ABAQUS. In order to overcome the convergence problem in the concrete slab's simulation, they ignored the concrete slab under negative bending and analyzed the steel beam with multipoint constraint to behave like a composite girder.

Recently, the mechanical model using the component method has become more and more popular for researchers to investigate the behaviour of composite connections. The principle of this method is to divide the connection into a set of mechanically connected components, representing the behaviour of elemental parts. The behaviour of each element is then described by general constitutive relations, either in plane stress or plane strain. And the connection behaviour can be combined together from these separate element relationships by considering force equilibrium and deformation compatibility. This technique has been used by Tschemmemegg [11], Madas [12] and Rassati et al. [13] in their research.

Although tremendous research has been conducted toward the semi-rigid composite connections, few of them were focused on the composite connection with precast hollowcore slabs. Therefore, the behaviour of this type of connection is still unclear. In this paper, through the full scale tests and 3-D finite element modelling, the behaviour of this type of connections has been studied extensively.

2 EXPERIMENTAL STUDIES

In order to study the behaviour of the composite connection with precast hollow core slabs, eight full scale flush endplate composite joint tests with precast hollowcore slabs were conducted by Fu et al. [14]. The variables are stud spacing, degree of the shear connections, area of the longitudinal reinforcement and slab thickness. All specimens were of cruciform arrangement as shown in Fig.1 to simulate the internal beam-column joints in a semi-rigid composite frame. The specimens were assembled from two 3300 mm long 457×191×89 kg/m; grade S275 universal beams and one 254×254×167 kg/m grade S275 universal column to form the cruciform arrangement. The beams are connected to the column flanges using 10mm thick flush end plates with two rows of M20 Grade 8.8 bolts. The steel connection is a typical connection currently used in UK practice for simple joints. A single row of 19mm diameter headed shear studs are pre-welded to the top flange of the steel beams. Finally, two 305×102×28 kg/m universal beams were connected to the column web to make up of the full joint arrangement. Heavy columns were used in the tests, and the flange is very thick to ensure no plastic deformation is observed in the column. Full details of the test set up, instrumentation and material are described in the reference Fu et al. [14].

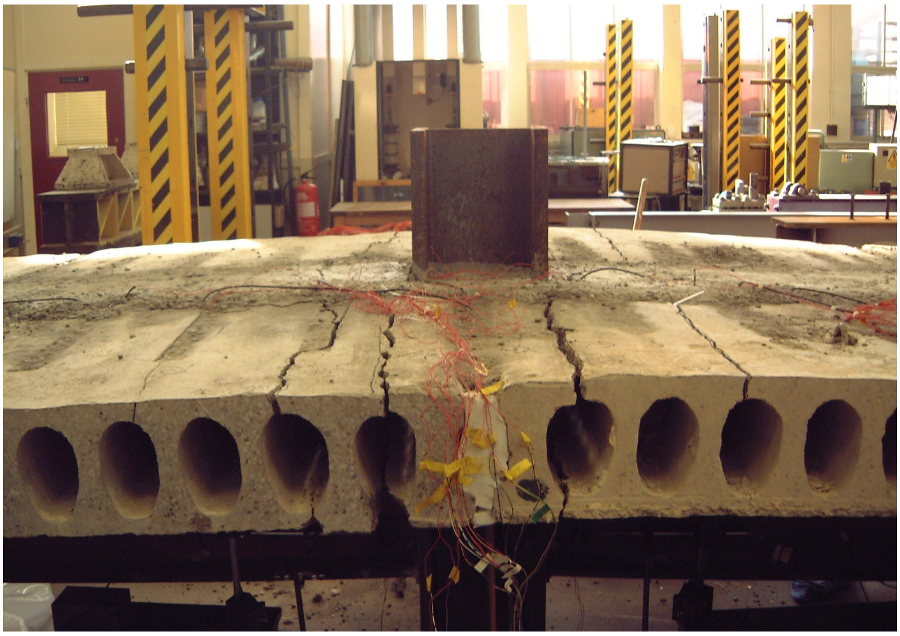

Figure 1. Full Scale Tests

3. THREE-DIMENSIONAL FINITE ELEMENT MODEL

Apart from full scale tests, a three-dimensional finite element model consisting of three-dimensional continuum (solid) elements was created by Fu et al. [15] as shown in Fig.2 to simulate the composite joints with precast hollowcore slabs. The general-purpose finite element package ABAQUS [16] is used for the simulation.

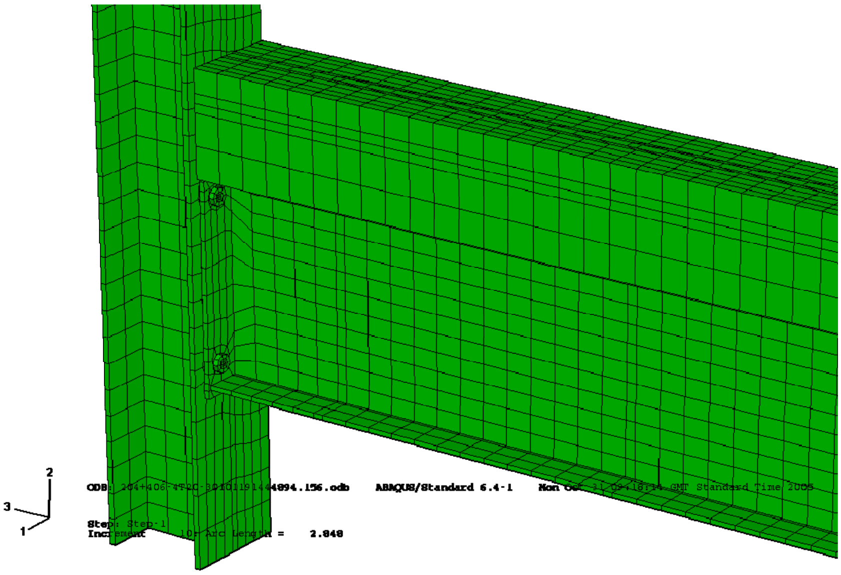

Figure 2. 3-D Finite Element Model

Using 3-D solid elements, the model replicates the composite joints from the experimental program by Fu et al. [14]. In order to reduce the computing time of the computer, only one side of the tests was simulated. The sizes of all the components except the hollowcore slabs were closely modelled as the actual experimental work.

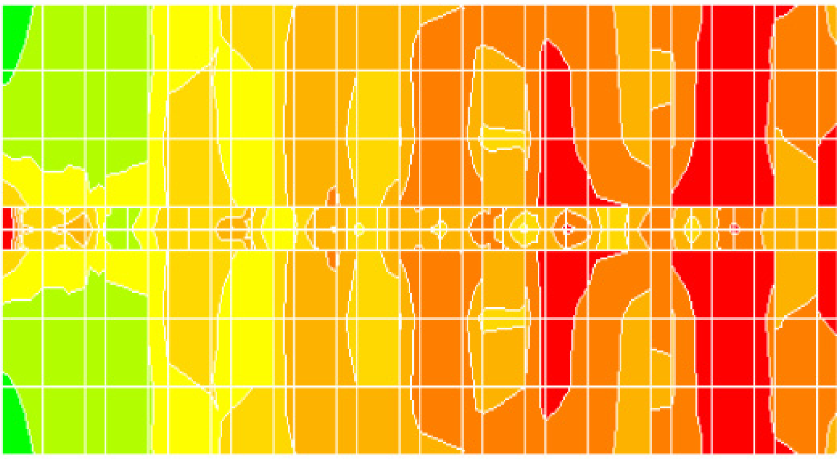

Figure 3. Effective Width of Composite Beam Using Precast Slab

The research conducted by El-Lobody et al. [17] showed that the effective breadth around the joint is confined to the in-situ infill concrete portion of the slabs as it is shown in Fig.3. Therefore, for the slab, only the in-situ infill concrete in the centre is modelled. The boundary conditions and method of loading adopted in the finite element analysis follow closely those used in the tests. Rather than use the smeared reinforcement slab model, the rebar were modelled using 3-d solid element with contact element between the rebar surface and the slab. Material non-linearity was included in the finite element model by specifying a stress-strain curve in terms of the true values of stress and plastic strain. All the structural steel components such as steel beams, steel columns, studs and bolts are modelled as an elastic-plastic material in both tension and compression. The stress-strains relationship in compression and tension are based on the coupon tests result conducted by Fu et al. [14]. A simplified elastic-plastic material model was adopted to simulate the concrete slabs. It is assumed that the concrete behaves as a linear-elastic material up to the yield. The option *PLASTIC is used to specify the plastic part of the material model that use the Von Mises yield surface. For the elastic part of the stress-strain curve, the value of the Young's modulus and the Poisson's ratio of the concrete are determined in accordance to BS8110 [18]. For the plastic part, two different values are adopted in different area of the slab. The main area of the concrete slab as shown is defined with the ultimate tensile stress f_t which is obtained from the concrete indirect tensile test. The area with 4×d length and 1.5 d width and the same height of the stud in the compressive side of the stud is defined with the yield stress 0.8 f_{cu} which is obtained from concrete cube tests. In the hogging moment regions, the concrete slab is mainly under tension. However, for the area around the front of the shear studs, the ultimate compressive strain ε_{cu} is given as 0.002ε. Although the proposed material model for the concrete can not predict the explicitly crack initiation and the evolution, the modelling result shows that it is sufficiently accurate for simulating the behaviour of the composite connection. The model has been validated against the full scale tests of Fu et al. [14], as shown in Fig.4, good agreement has been obtained.

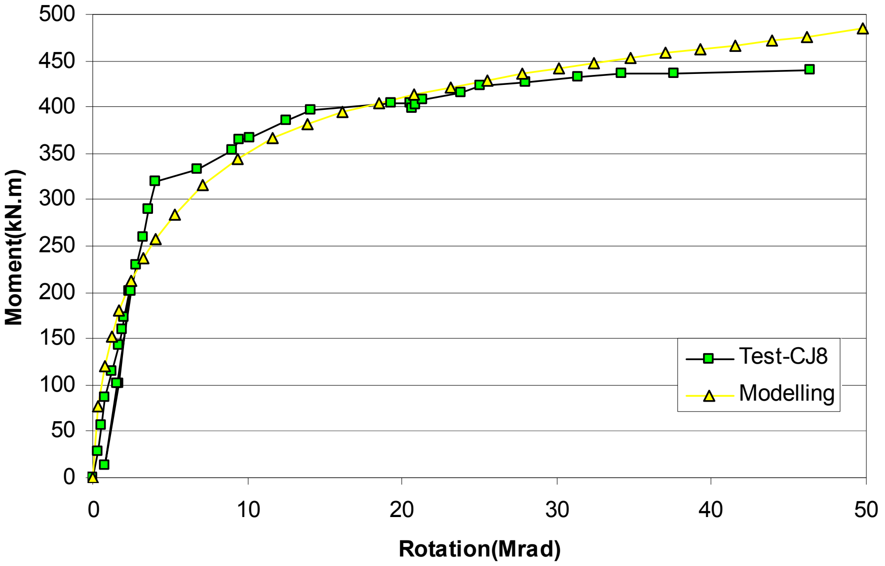

Figure 4. Moment vs. Rotation Curves for Test CJ8 and FE-solution

4. THE STRUCTURAL BEHAVIOUR OF THE CONNECTIONS

Using the results of full scale tests of Fu et al. [14] and the proposed 3-D FE model, the parametric study has been conducted. The main variables are first stud spacing, bottom flange thickness and the column sizes etc. Base on the full scale tests result and parametric study of the proposed 3-D model the structural behaviour of the connection is studied as follows:

4.1 Effect of the Amount of Longitudinal Bars

Fig. 5 compares the moment-rotation curves of tests CJ2, CJ6, and CJ7 of Fu et al. [14]. All three tests have full shear connections with the same slab thickness except the longitudinal bars were 2T20, 4T16 and 2T16 respectively. It can be observed from the curves that the rotation stiffness was enhanced with an increase in longitudinal reinforcement. It showed that increases in the amount of longitudinal reinforcement leads to higher moment and rotation capacity.

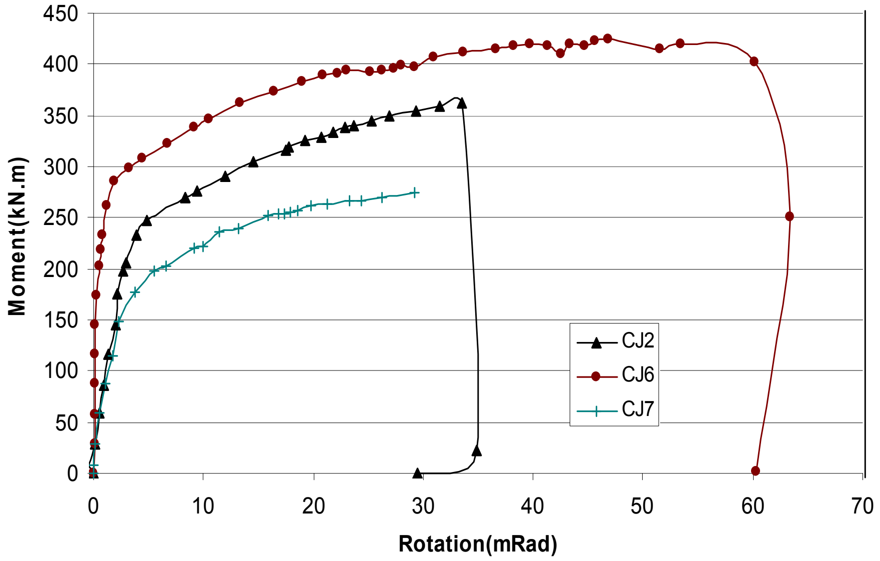

Figure 5. Comparison of Moment-rotation Curves of Tests CJ1, CJ2 and CJ7

4.2 Effect of Precast Slab Thickness

In order to investigate the effective of the slab thickness, two 3-D finite element models CJ8-400 and CJ8-150 were built, these two models are similar to full scale test CJ8 of Fu et al [14], with the slab thickness of 400mm and 150 mm respectively. Fig.6 is the comparison of the moment rotation relationship of these two models with test CJ8 of Fu et al [14]. Results show that by using a deeper slab, moment capacity was increased, but purely due to an increase in the lever arm, this being accompanied a slight reduction in the rotation capacity.

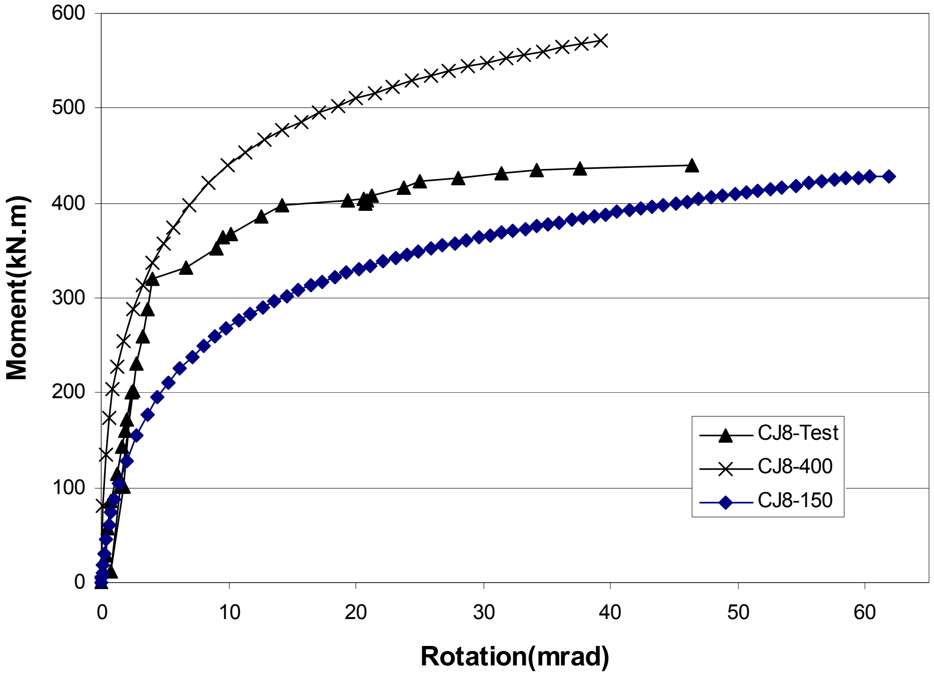

Figure 6. Comparison of Moment Rotation Relationship with Different Slab Thickness

4.3 Effect of Stud Spacing and Stud Number

Fig 7 is the comparison of moment-rotation curves of Tests CJ1 and CJ2 of Fu et al. [14].Test CJ1 and CJ2 are identical except that number of the studs is 7 and 4 respectively and with different stud spacing. They are both full shear connection tests. From the comparison of the moment-rotation curves of tests CJ1 and CJ2 (as shown in Fig.7), it can be seen that, although different stud spacing and numbers of stud were used, as both tests were full shear connection, no distinct difference of moment and rotation capacity was found from the test results. The only difference was the rotation stiffness of the composite connection. Test CJ1 has larger rotation stiffness than CJ2, as more shear studs were used. Therefore, it can be concluded that for full shear connection, the studs number and spacing does not has much influence on the moment capacity and rotation capacity of the connection. It can be also concluded that under the same conditions, the more studs, the larger the rotation stiffness of the connection.

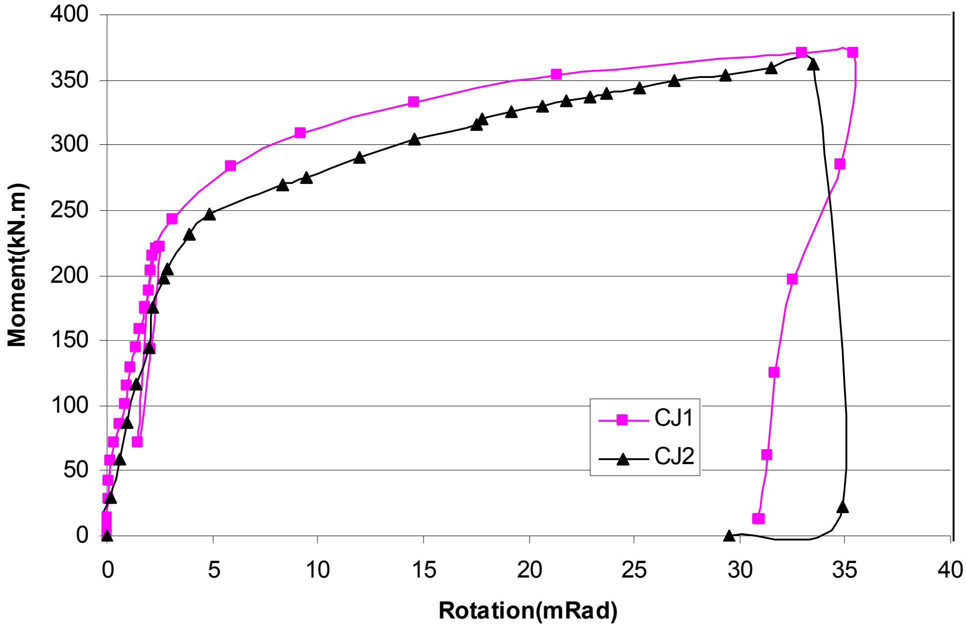

Fig 7 Comparison of moment-rotation curves of Tests CJ1 and CJ2

4.4 Effect of Column Sizes

In the actual design practice, yielding of the column flange and buckling of the column web could occur if smaller column sizes were used. In order to further study the behaviour of composite joints, different sizes of column were chosen in the finite element models for the parametric studies. Three 3-D finite element models with the column sizes of 254 ×254×167 UC, 203 ×203×86 UC and 203 ×203×46 UC were chosen for the parametric study, where model 254 ×254×167 UC replicated the test CJ2 of the full-scale test of Fu et al. [14]. The three models have column web thicknesses of 19.2mm, 12.7mm and 7.2mm with the flange thickness of 31.7 mm, 20.5 mm 11 mm, respectively, 457 ×191×89 UB beams were used throughout. All other conditions were kept the same as the full scale tests of Fu et al. [14]. The modelling results are shown in Fig.10 and Table 1. It can be seen that the moment-rotation curves for model 254 ×254×167 UC and model 203 ×203×46 UC are similar, with slightly higher rotation capacity for model 254 ×254×167 UC. With the column sizes decreases to 203 ×203×46 UC, it can be seen that the rotation stiffness decreases with an increases in rotation capacity. The failure modes of all three models are the longitudinal bar failure. As shown in Table 1, for model 254 ×254×167 UC, due to the heavy column used, the maximum stresses for the column web and flange are only 88N/mm^2 and 101.6N/mm^2 respectively. For the other two models, it can be seen that the columns are about to yield. Figure 8 and 9 show the models of UC203×203×86 and UC203×203×46 at their failure state respectively. It can be seen that the deformation of the column in UC203×203×46 is obviously larger than UC203×203×86 due to the smaller column size. The maximum stress in the web occurred at the position near the bottom flange of the beam, the assumed centre of the rotation. Also, the rotation of the UC203×203×46 is much greater due to the deformation of the column. For UC 254×254×167, as heavy column is used, the stress of the column is very small and remains elastic, as was observed in the tests.

It can be concluded that as long as heavy columns are used, the connection can achieve a certain amount of moment capacity and rotation capacity without much difference. Smaller column size will cause higher rotation capacity and lower rotation stiffness.

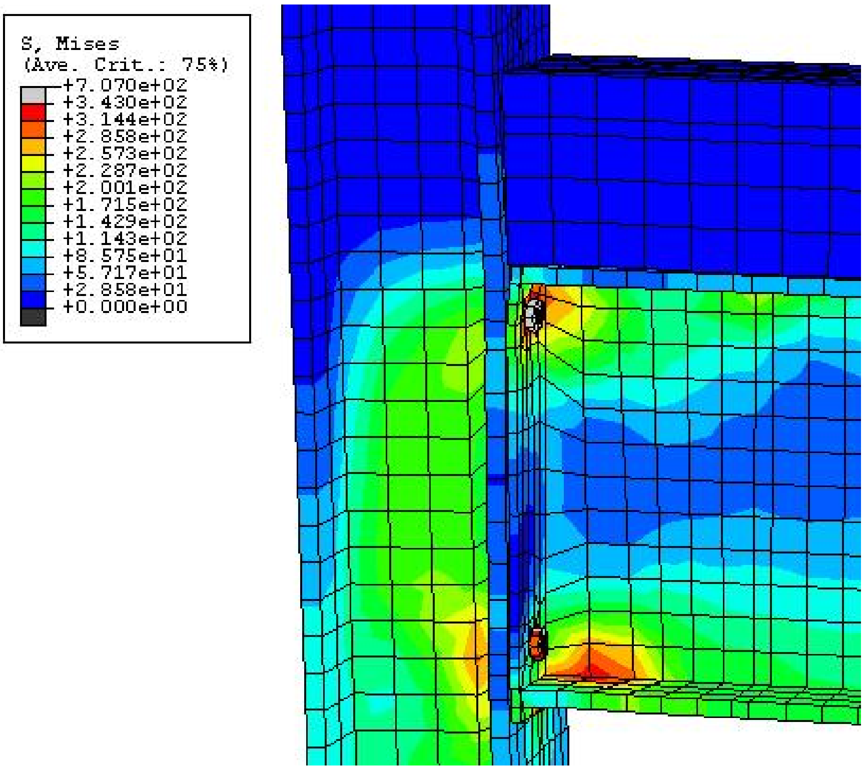

Figure 8. UC203×203×86 at Failure (Longitudinal Bar Failure)

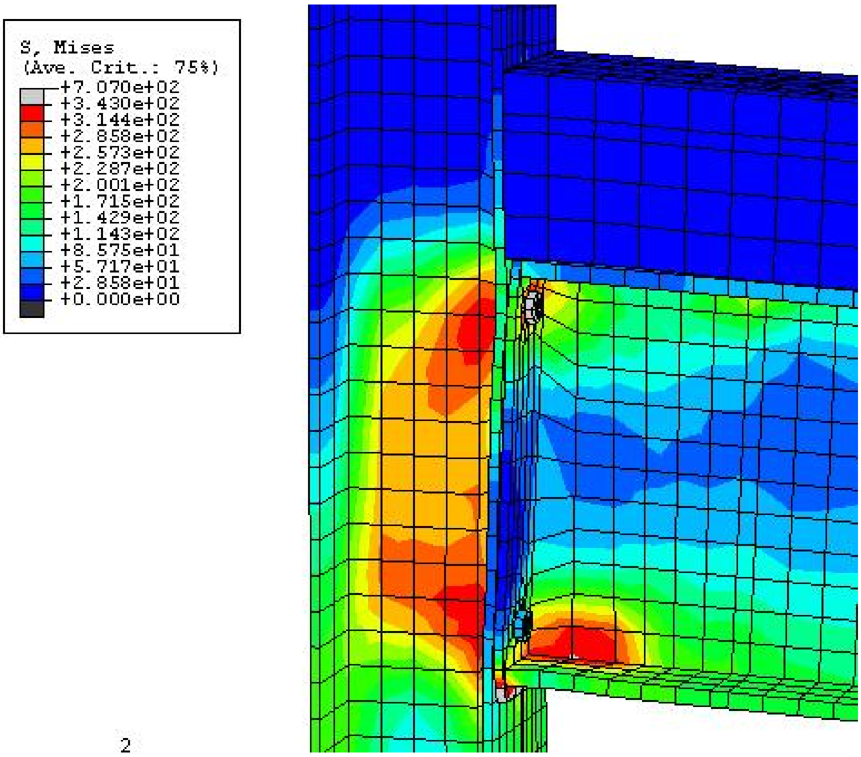

Figure 9. UC203×203×46 at Failure (Longitudinal Bar Failure)

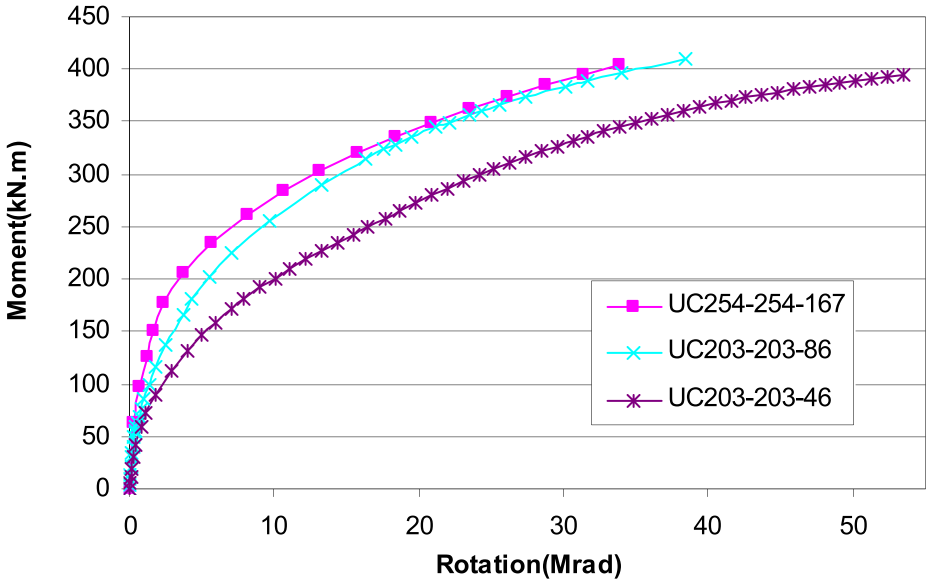

Figure 10. Variation of Moment-rotation Curves with Different Size of the Column

Table 1. Modelling Result

	Moment (kN.m)	Rotation (Mrad)	Maximum column web stress (N/mm2)	Maximum column Flange stress (N/mm2)	**Mode of failure**
254 ×254×167 UC	404	34.6	88	101.6	rebar
254 ×254×167 UC	409	38.4	303.4	248	rebar
203 ×203×46 UC	395	53.4	343.27	304.3	rebar

5. CONCLUSION

The behaviour of semi-rigid composite connections with precast hollowcore slabs was examined using full scale tests and 3-D finite element modelling technique, different stud spacing and position, amount of longitudinal bars, column size and precast slab thickness have been examined, following conclusions can be drawn:

1. With full shear connection, increases in the amount of longitudinal reinforcement leads to higher moment and rotation capacity.
2. Using a deeper slab, moment capacity was increased, but purely due to an increase in the lever arm, this being accompanied a slight reduction in the rotation capacity.
3. The stud spacing does not have much influence on the moment capacity and rotation capacity of the connection.
4. Smaller column size will cause higher rotation capacity. However, column flange yielding or web buckling could lead to lower rotation stiffness.

REFERENCE

[1] Johnson, R.P. and Hope-Gill, M.C., "Semi-rigid Joints in Composite Frames", International Association for Bridge and Structural Engineering, Ninth Congress, Prelim. Report, Amsterdam, May 1972, pp. 133-44.

[2] MacMackin, P.J. and Cheung, P.A.T., "Flexible Steel and Composite Joint Design", Pacific Structural Steel Conference, Queensland, Australia, 1989, pp. 479-496.

[3] Davison, J.B., Lam, D. and Nethercot, D.A., "Semi-rigid Action of Composite Joints", The Structural Engineer, 1990, Vol. 68, No. 24.

[4] Anderson, D. and Najafi, A.A, "Performance of Composite Connections: Major Axis End Plate Joints", Journal of Constructional Steel Research, 1994, Vol. 31, No. 1, pp. 31-57.

[5] Xiao, Y., Choo, B.S. and Nethercot, D.A., "Composite Connections in Steel and Concrete, I. Experimental Behavior of Composite Beam–Column Connections", Journal of Constructional Steel Research, 1994, Vol. 31, pp. 3–30.

[6] Krisbnamurthy, N. and Graddy, D., "Correlation between 2- and 3-dimensional Finite Element Analysis of Steel Bolted End-plate Connections", Computers and Structures, 1996, Vol. 6, pp. 381-389.

[7] Ayoub, A., and Filippou, F., "Mixed Formulation of Nonlinear Steel—Concrete Composite Beam Element", Journal of Structural Engineering, 2000, Vol. 126, No. 3, pp. 371-381.

[8] Sebastian, W.M. and McConnel, R.E., "Nonlinear FE Analysis of Steel-concrete Composite Structures", Journal of Structural Engineering, 2000, Vol. 126, No. 6, pp. 62-674.

[9] Baskar, K., Shanmugam, N.E. and Thevendran, V. "Finite-element Analysis of Steel-concrete Composite Plate Girder", Journal of Structural Engineering, 1996, Vol. 128, No. 9, pp. 1158-1168.

[10] Ahmed, B. and Nethercot, D.A., "Prediction of Initial Stiffness and Available Rotation Capacity of Major-axis Flush End-plate Connections", Journal of Constructional Steel Research, 1997, Vol. 41, No. 1, pp. 31–60.

[11] Tschemmernegg, F., "On the Nonlinear Behaviour of Joints in Steel Frames, Connections in Steel Structures: Behaviour, Strength and Design", Elsevier Applied Science Publishers, 1998, London, pp. 158-165.

[12] Madas, P.J., "Advanced Modelling of Composite Frames Subject to Earthquake Loading", Ph.D. Thesis, University of London, 1998.

[13] Rassati, G.A., Leon, R.T. and Noe, S., "Component Modelling of Partially Restrained Composite Joints under Cyclic and Dynamic Loading", Journal of Structural Engineering, 2004, Vol. 130, No. 2.

[14] Fu, F. and Lam, D., "Experimental Study on Semi-Rigid Composite Joints with Steel Beams and Precast Hollowcore Slabs", Journal of Constructional Steel Research, August 2006, Vol. 62, No. 8, pp. 771-782.

[15] Fu, F., Lam, D. and Ye, J.Q., "Parametric Study of Semi-rigid Composite Connections with 3-D Finite Element Approach", Engineering Structures, 2007, Vol. 29, Issue 6, pp. 888-898.

[16] ABAQUS Theory Manual, Version 6.4. Hibbitt, K-arlsson and Sorensen, Inc. Pawtucket, R.I., 2003.

[17] El-Lobody, E. and Lam, D., "Finite Element Analysis of Steel– Concrete Composite Girders", Advances in Structural Engineering, 2003, Vol. 6, No. 4, pp. 267 – 281.

[18] BS 8110, Part 1, "Structural Use of Concrete — Part 1: Code of Practice for Design and Construction, British Standards Institution, London, 1997.